

# **Plasma Processing of Carbon Nanostructures and Their Characterization**

*By*  
**Rajib Kar**

**PHYS 01201104016**

**Bhabha Atomic Research Centre, Mumbai**

*A thesis submitted to the  
Board of Studies in Physical Sciences*

*In partial fulfillment of requirements  
for the Degree of*

**DOCTOR OF PHILOSOPHY**

*of*

**HOMI BHABHA NATIONAL INSTITUTE**



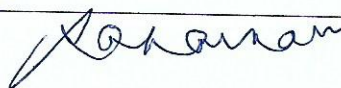
**6<sup>th</sup> October, 2017**

# Homi Bhabha National Institute<sup>1</sup>

## Recommendations of the Viva Voce Committee

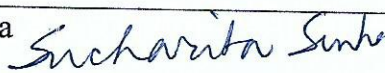
As members of the Viva Voce Committee, we certify that we have read the dissertation prepared by Rajib Kar entitled "Plasma Processing of Carbon Nanostructures and Their Characterization" and recommend that it may be accepted as fulfilling the thesis requirement for the award of Degree of Doctor of Philosophy.

Chairman - Dr. Saibal Basu



Date: 6/10/17

Guide / Convener – Dr. Sucharita Sinha



Date: 6/10/2017

Examiner - Prof. Vikas L. Mathe



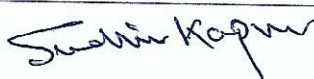
Date: 6/10/2017

Member 1- Prof. D.S. Patil



Date: 06.10.2017

Member 2- Dr. Sudhir Kapoor




Date: 6/10/17.

Final approval and acceptance of this thesis is contingent upon the candidate's submission of the final copies of the thesis to HBNI.

I/We hereby certify that I/we have read this thesis prepared under my/our direction and recommend that it may be accepted as fulfilling the thesis requirement.

Date: 6/10/17

Place: Mumbai



Guide: Dr. Sucharita Sinha

डॉ. सुचरिता सिन्हा, उत्कृष्ट वैज्ञानिक  
Dr. Sucharita Sinha, OS

अध्यक्ष, लेसर एवं प्लाज्मा सतह प्रक्रम अनुभाग  
Head Laser & Plasma Surface Processing Section

भारत सरकार/Government of India

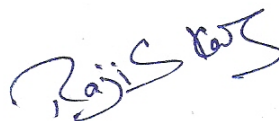
भाभा परमाणु अनुसंधान केंद्र/Bhabha Atomic Research Centre  
ट्रॉम्बे, मुंबई-400085./Trombay, Mumbai-400085.

<sup>1</sup> This page is to be included only for final submission after successful completion of viva voce.

## STATEMENT BY AUTHOR

This dissertation has been submitted in partial fulfillment of requirements for an advanced degree at Homi Bhabha National Institute (HBNI) and is deposited in the Library to be made available to borrowers under rules of the HBNI.

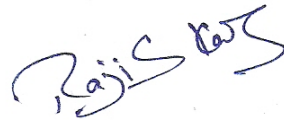
Brief quotations from this dissertation are allowable without special permission, provided that accurate acknowledgement of source is made. Requests for permission for extended quotation from or reproduction of this manuscript in whole or in part may be granted by the Competent Authority of HBNI when in his or her judgment the proposed use of the material is in the interests of scholarship. In all other instances, however, permission must be obtained from the author.



Rajib Kar

## DECLARATION

I, hereby declare that the investigation presented in the thesis has been carried out by me. The work is original and has not been submitted earlier as a whole or in part for a degree / diploma at this or any other Institution / University.



Rajib Kar



## List of Publications arising from the thesis

### Journal

1. “Bias independent growth of carbon nanowalls by microwave electron-cyclotron resonance plasma CVD”, **R.Kar**, N.N. Patel, S.S. Chopade, S.Mukherjee, A.K. Das and D.S. Patil, *Journal of Experimental Nanoscience*, **2014**, Vol.9, 575-581.
2. “Effect of substrate heating and microwave attenuation on the catalyst free growth and field emission of carbon nanotubes”, **R.Kar**, S.G. Sarkar, C.B. Basak, Avinash Patsha, Sandip Dhara, Chanchal Ghosh, Divakar Ramachandran, N. Chand, S.S. Chopade, D.S. Patil, *Carbon*, **2015**, Vol. 94, 256-565.
3. “Detailed investigations on the mechanism of co-deposition of different carbon nanostructures by microwave plasma CVD”, **R.Kar**, N.N. Patel, N. Chand, R.K. Shilpa, R.O. Dusane, D.S. Patil, S. Sinha, *Carbon*, **2016**, Vol.106, 233-242.

### Chapters in books and lectures notes

1. Materials under Extreme Conditions; Editors: A.K. Tyagi, S. Banerjee; Publishers: Elsevier. Chapter 12 “Cold plasma processing of materials for extreme conditions”, D. S. Patil, **R. Kar** and S. S. Chopade; To be published in February 2017

### Conferences

1. Bias Independent growth of Carbon nanowalls; **R. Kar**, N.N. Patel, S.S. Chopade, S. Mukherjee, A.K. Das and D.S. Patil, Presented as poster in 2<sup>nd</sup> International Conference on Advanced Nanomaterials and Nanotechnology (ICANN-2011) at IIT-G.
2. Raman Spectroscopic Investigations on Carbon Nanowalls Grown in N<sub>2</sub> - CH<sub>4</sub> Plasma without application of substrate bias; **R. Kar**, N.N. Patel, S.S. Chopade, S. Mukherjee, Naresh Chand, A.K. Das and D.S. Patil, presented as oral in International Conference and

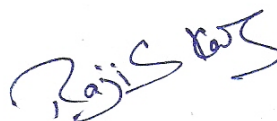
Workshop of Nanostructured Ceramics and Other Nanomaterials (ICWNCN-2012) at Delhi University.

3. Microwave Plasma Enhanced Chemical Vapor Deposition of Carbon Nanotubes on Metallic Substrates; **Rajib Kar**, MN Deo, Naresh Chand, AK Das, DS Patil' Presented as poster in 27<sup>th</sup> National plasma symposium-2012 (Plasma-2012) at IASST-Pondicherry University.
4. Effect of Localized Surface Resonance on the Growth of Carbon Nanowalls: Inference from Langmuir Probe Diagnostics, **R. Kar**, N.N. Patel, S. Mukherjee, A.K. Das and D.S. Patil , Presented as oral in 28<sup>th</sup> National plasma symposium-2013 (Plasma-2013) at KIIT, Bhubaneshwar.
5. Deposition of Multi-walled Carbon Nanotubes by Microwave Plasma Enhanced Chemical Vapor Deposition without Addition of Any External Catalyst, **Rajib Kar**, S.G. Sarkar, M.N. Deo, R. Tewari, K.C. Mittal, N. Chand, A.K. Das and D.S. Patil, Presented as poster in Nanoscale Excitations in Emerging Materials (NEEM-2013) at IPR, Gandhinagar.
6. Field Emission Behavior of Carbon Nanotubes Grown on Inconel 600 by Microwave Plasma CVD: effect of Substrate Pretreatment and Microwave Field Attenuation, **R. Kar**, S. G. Sarkar, M.N. Deo, N. Chand, K.C. Mittal, A.K. Das, and D.S. Patil, Presented as oral in N-SEPMI 2014 at University of Pune.
7. Growth of Carbon Nanotubes by PECVD: Information Obtained through OES, **Rajib Kar**, Naresh Chand, Arundhati Bute, A.K. Das and D.S. Patil, Presented as oral in N-SEPMI 2014 at University of Pune.
8. Co-deposition of Different Carbon Based Nanostructures and Diamond via Low Pressure Microwave Plasma CVD, **Rajib Kar**, Nishant N. Patel, Naresh Chand, Arundhati Bute, D.S. Patil, Sucharita Sinha' Presented as oral in IVSNS 2015 at TIFR.

## Others

1. “Microwave ECR plasma assisted MOCVD of  $Y_2O_3$  thin films using  $Y(tod)_3$  precursor and their characterization”, S. Barve, M. Deo, **R. Kar**, N. Sreenivasan, R. Kishore, A. Biswas, B. Bhange, M. Rao, L.M. Gantayet, D. S.Patil; *Plasma process and polymers*, **2011**, Vol. 8, 740-749.
2. “A possible explanation of the anomalous emissive probe behavior in a reactive RF plasma”, **R. Kar**, S.A. Barve, S.S. Chopade, A.K. Das, D.S. Patil, *Plasma Sources Science and Technology*, **2012**, Vol. 21, 055009 (7pp).
3. “Comparative study of nanocomposites prepared by pulsed and dc sputtering combined with plasma polymerization suitable for photovoltaic device applications”, A.A. Hussain, A.R. Pal, **R. Kar**, H. Bailung, J. Chutia, D.S. Patil, *Materials Chemistry and Physics*, **2014**, Vol. 148, 540-547.
4. “Scratch resistance and tribological properties of SiOx incorporated diamond-like carbon films deposited by r.f. plasma assisted chemical vapor deposition”, N. Kumar, S.A. Barve, S.S. Chopade, **R. Kar**, N. Chand, S. Dash, A. K. Tyagi, *Tribology International*, **2015**, Vol. 84, 124-131.
5. “Pulsed laser-assisted removal of powder coating from galvanized steel surface: a characterization study”, A. Kumar, M. Prasad, S. Shail, R.B. Bhatt, P.G. Behere, Md. Afzal, A. Kumar, **R. Kar**, J.P. Nilaya, D.J. Biswas, *Applied Physics: A*, **2015**, Vol. 119, 853-858.
6. “Unique erosion features of hafnium cathode in atmospheric pressure arcs of air, nitrogen and oxygen”, S. Ghorui, K.C. Meher, **R. Kar**, N. Tiwari, S. N. Sahasrabuddhe; *Journal of Physics D: Applied Physics*, **2016**, Vol.49, 295201 (13 pp).
7. “Synthesis of uranium-di-oxide nanoparticles by pulsed laser ablation in ethanol and their characterization”, A. Kumar, M. Prasad, S. Shail, C. Baghra, B.N. Mohanty, R.B. Bhatt, P.G. Behere, Mohd. Afzal, A. Kumar, S. Neogy, **R. Kar**, D.J. Biswas, *Nano-structures & Nano-objects*, **2016**, Vol. 7, 75-80.
8. “Effect of self-bias on the elemental composition and neutron absorption of boron carbide films deposited by RF plasma

- enhanced CVD”, A. Bute, Jagannath, **R. Kar**, S.S. Chopade, S.S. Desai, M.N. Deo, Pritty Rao, N. Chand, S. Kumar, K.Singh, D.S. Patil, S. Sinha, *Materials Chemistry and Physics*, **2016**, Vol.182, 62-71.
9. “SiO<sub>x</sub> containing Diamond like Carbon coatings: Effect of substrate bias during deposition”, S.A. Barve, S.S. Chopade, **R. Kar**, N. Chand, M.N. Deo, A. Biswas, N.N. Patel, G.M. Rao, D.S. Patil, S.Sinha, *Diamond and Related Materials*, **2017**, Vol. 71, 63-72.
  10. “Role of hydrogen diffusion in temperature-induced transformation of carbon nanostructures deposited on metallic substrates by using a specially designed fused hollow cathode cold atmospheric pressure plasma source”, Bikash Sharma, **R Kar**, Arup R Pal, R K Shilpa, R O Dusane, D S Patil, S R Suryawanshi, M A More, S Sinha, *Journal of Physics D: Applied Physics*, **2017**, Vol. 50, 155207 (11 pp).



Rajib Kar

**Dedicated to my mother Mrs. Uma Kar  
& my wife Sucharita**

## ACKNOWLEDGEMENT

It is impossible to mention the names of each and every individual who has helped me during the course of my thesis. There lies an obvious risk of failing to mention contributions of some. I apologize sincerely in advance for such mistakes while writing this acknowledgement.

I start writing this section by offering my deep and sincere gratitude to my guide, Dr. Sucharita Sinha for her invaluable guidance and constant encouragement. My deepest gratitude also lies towards Dr. D.S. Patil, my very first mentor during beginning of my research career. His keen interest and constant inputs in my research was invaluable to my scientific progress. Dr. Sinha and Dr. Patil helped to keep my morale high during difficult times.

I would like to express my sincere thanks to Dr. A.K. Das, former head, Laser and Plasma Technology Division (L&PTD) and Dr. L.M. Gantayet, former director, Beam Technology and Development Group (BTDG) who gave me the opportunity to start my doctoral research work. Both of them, especially Dr. Das had always taken keen interest in my work and I would always remember his advice to keep my “scientific spirit” alive. Thanks are also due to Dr. K. Dasgupta, former associate director, BTDG, Dr. P.V. Anathapadmanabhan, former head, TPPS and Dr. A.V. Bapat, former head, PBEDS for their constant encouragement. I am grateful to my doctoral committee members, Dr. Saibal Basu, head, Solid State Physics Division, Dr. Sudhir Kapoor, Radio-photochemistry division, Dr. S.K. Gupta, former head, TPD for spending their precious time for periodic assessment of the work and offering valuable suggestions to enhance its quality.

During this journey, I have been fortunate enough to get associated with many

respectable senior members of BARC and young scientists of DAE whose generous help culminated into this thesis. Also, most of them have actively collaborated with me in my research. Among them, I remember Dr. C.B. Basak, Dr. Raghvendra Tewari, Dr. H. Sodaye for their help and support in electron microscopy and Dr. M.B. Kakade, Dr. S. Ramanathan, Dr. A. Nagaraj, Dr. M.N. Deo, Mr. S. Mukherjee for providing their characterization facilities. I fondly recall my associations with Mr. Nishant Patel, Dr. Avinash Patsha, Mr. Chanchal Ghosh, Mr. Rohan Phatak, Mrs. Shreya G Sarkar, Mrs. Arundhati Bute, Mrs. Vandana C. Mishra, Dr. Supriya Chopade, Dr. Shruti A. Barve, Mr. Thangam, Mr. Kannan, Dr. A. Pragatheeswaran, Mr. Y. Chakravarthy. All of them had gone extra miles to give crucial supports to my work, especially Nishant, Avinash, Shreya and Chanchal. I sincerely hope to continue these associations after completing my thesis.

During the thesis, I have been greatly benefitted from the associations of different researchers of Indira Gandhi Centre for Atomic Research (IGCAR) and IIT-Bombay. Dr. A.K. Tyagi, Dr. E. Mohandas, Dr. Divakar Ramachandran, Dr. Sandip Dhara are among the senior colleagues of IGCAR without whose generous help this thesis would have been incomplete. Same is true for Ms. Shilpa R.K. and Dr. R.O. Dusane of IIT-Bombay.

It is also a great pleasure of mine to record my thanks to Mr. Naresh Chand and Mr. Sankalp Thakur. They have tirelessly helped me in organizing different experiments and also helped in solving many technical problems. Without their help it would have been impossible to run a single experiment. Mr. D.P. Chopade, Mr. Tushar Hire and Ms. Vanita Shekar are other persons whose solid support forms the backbone of my research.

It gives me immense pleasure to express my deep gratitude to my mother and my wife for their constant support, well wishes and encouragement. These two ladies have always been pillars of strength for me and without their support this work could have never been completed.





# Homi Bhabha National Institute

## SYNOPSIS OF Ph. D. THESIS

- 1. Name of the Student: Rajib Kar**
- 2. Name of the Constituent Institution: Bhabha Atomic Research Centre**
- 3. Enrolment No. : PHYS 01201104016**
- 4. Title of the Thesis: Plasma Processing of Carbon nanostructures and their characterization**
- 5. Board of Studies: Physical Sciences**

### SYNOPSIS

Carbon is one of the most researched elements in nature. Since ages, people have been using different forms and allotropes of carbon for different purposes. While diamond is most popular for its gem value, graphite is mostly used as pencil-tip, dry lubricant for machinery and as a conducting material. Laboratory grown synthetic diamond has many desirable properties such as high mechanical hardness, thermal conductivity, electrical resistivity, chemical inertness and broad optical transparency. Several investigations have been reported on the potential and actual applications of poly, nano and single crystal diamond films [1]. Apart from diamond, recent interest in nanotechnology has also lead to the discovery of a variety of graphitic carbon nanostructures and their exciting applications. Carbon nanotube (CNT) and graphene nanowall (GNW) are two such nanostructures. Since the discovery of CNTs in 1991 it has been given the status of another allotrope of carbon. CNTs are being projected for a wide range of applications in diverse fields ranging from electronics to medicine [2, 3].

Due to their excellent electron emission properties CNTs have a strong potential application as a cold cathode [4]. GNW, sometimes also called carbon nanowall (CNW) is a two-dimensional nanostructure of graphene sheets which stand on the substrate like a wall. GNW is a relatively newer nanostructure and it is also relatively less explored. Presently, a good amount of research on this material has shown that GNWs can serve as a good catalyst support structure for fuel cell [5] and as the negative electrode for lithium ion battery [6]. Moreover, because of its high surface area and high aspect ratio, its field-emission capabilities are also comparable to that of CNT [7]. In addition to CNT and GNW nano-crystalline diamond (NCD) is another type of carbon nanomaterials which have high hardness, excellent chemical inertness and good biocompatibility among other properties.

In the work being reported here, all these carbon nanostructures have been deposited via low pressure plasma enhanced chemical vapour deposition (PECVD) process. Plasma has long been one of the preferred medium for deposition of carbon nanostructures. Plasma consists of energetic electrons and ions which actively take part or aid in the deposition process. The main advantage of using plasma is the low deposition temperature and high deposition rate. Using plasma as a medium of deposition is thus advantageous compared to conventional chemical vapour deposition (CVD) technique. Nowadays, deposition of carbon nanostructures are mostly carried out using non-thermal plasmas under vacuum as they provide reasonable control over deposition while maintaining a comfortably high deposition rate. There are different types of non-thermal plasmas and each having their own merits and demerits. We have used two different types of non-thermal plasmas, namely microwave electron cyclotron resonance (ECR) plasma and low pressure microwave plasma for the deposition of

different nanostructures such as CNTs, CNWs and NCDs.

Microwave electron cyclotron resonance (ECR) plasma is a type of non-thermal plasma which operates at the low pressure regime of  $\sim 10^{-4}$  Torr. ECR plasma is an efficient process for generation of large area uniform plasma at the substrate location [8]. Since this process works at low operating pressure, low temperature regime hence atom-by-atom deposition is possible in this case. It leads to a precision in the deposition which is very important for growth of nanomaterials via self-assembly. Since, plasma generation mechanism in this case is electrode-less in nature, so ECR plasma deposition results in very low contamination when compared to other plasma processes. In spite of having these advantages there are very few reports available on the successful deposition of Carbon nanowall by ECR plasma CVD [9]. During our study, contrary to the conventional ECR plasma synthesis route of CNWs no external substrate bias has been applied. Our experiments lead to the deposition of dense CNWs on Si substrates using Ni as catalyst with different process gas compositions.

Microwave plasma enhanced chemical vapour deposition (MPECVD) is another PECVD process which is convenient for depositing carbon based structures. Operation of microwave plasma in comparatively high operating pressure regime (up to even 100 Torr) allows deposition of crystalline diamond. In fact, microwave plasma CVD favours for diamond deposition as it offers a high operating pressure and temperature regime with good plasma density compared to other plasma CVD methods [11]. Apart from growing diamond, microwave plasma has also been routinely used to deposit CNT and GNW. We have used MPECVD to grow CNTs directly on metallic Inconel 600 substrates. Inconel was chosen as the substrate to grow CNTs directly on the metal surface to ensure intimate contact with the conducting base of substrates. It

also results in good mechanical integrity and low contact resistance between the grown CNTs and the substrate [12]. But, direct growth of CNTs on metal surfaces normally requires in-situ formation of catalyst nanoparticles on the metallic substrates [14]. We have been successfully grown multi-walled CNTs (MWCNTs) on Inconel, characterized them and studied their field emission properties. The novel concept in the deposition was to combine heat-treatment of the substrate with the attenuation of the microwave on the substrate. This combination resulted in enhancement of field emission current density.

Co-deposition of different carbon nanostructures was another area of investigation. Co-deposition of carbon nanotubes (CNTs) along with nano-crystalline diamond and graphene nanowalls (GNWs) was made possible by MPECVD process. It is known that CNT and nanocrystalline diamond (NCD) based composite materials can have superior physical properties than either of them but controlled deposition of two different nanostructures on different substrates in a single experiment [14] has been difficult to achieve. However, in our case, CNTs have been grown directly on Inconel and other nanostructures could be grown on the Si microwave attenuator placed above Inconel during the same experiment. This thesis gives a detailed analysis of all these experiments along with our results and findings.

The thesis is organized as follows: Chapter 1 gives an introduction on plasma, PECVD, nanotechnology and carbon based nanostructures. It also discusses the importance of PECVD technique for the deposition of nanostructures and compares this with other available deposition techniques. The introduction section also discusses about the different characterization techniques used in the thesis. An exhaustive literature survey is also included in this section.

Chapter 2 gives details on the two different experimental set-ups namely ECR-CVD and MPECVD used during the course of the research. All the necessary hardware of these set-ups and their utilities are also discussed in this section. Various substrate preparation methods used for Inconel and Si prior to the deposition of nanostructures have also been discussed.

Chapter 3 deals with the deposition and characterization of carbon nanowalls (CNWs) by ECR-CVD method without application of any external bias. As stated previously, an electrical substrate bias (-50 to -200 V) is generally used during the growth of Carbon nanostructures in ECR plasma for enhancement of ion bombardment energy so as to attract more positive species without causing sputtering effect [15]. However, our investigations established that synthesis of Carbon nanowalls (CNW) by ECR plasma assisted CVD process is possible without an application of any external bias. CNWs were grown on Si substrates using  $H_2 / CH_4$  and  $N_2/CH_4$  plasma at  $650^0\text{C}$  substrate temperature. Ni was used as catalyst for this synthesis. Our investigations indicate that the problem of silicide formation does not occur whether the substrate had a diffusion resistant barrier or not. Formation of CNWs was confirmed by scanning electron microscopy (SEM), high-resolution transmission electron microscopy (HRTEM) and Raman Spectroscopy. Special thrust is given on analyzing the results of Raman spectroscopy and possible growth mechanism for CNWs in this particular scenario is also discussed. Since the observed plasma potential is low and no electrical bias is applied to the substrates therefore it is possible that a strong lateral electric field generated in Ni nanoparticles gives rise to the growth of CNWs on the substrates [16].

Chapter 4 provides detail on deposition and characterization of multi-walled carbon nanotubes (MWCNTs) by MPECVD on Inconel 600 without use of any external

catalyst. Grown CNTs were characterized by field emission scanning electron microscopy (FESEM), HRTEM, X-ray diffraction (XRD) and Raman spectroscopy. Since CNTs are known to have excellent field emission properties, field emission studies were also conducted on the deposited samples. It showed that field emission current density increased from  $200 \mu\text{A} / \text{cm}^2$  at  $\sim 5.5 \text{ V}/\mu\text{m}$  to  $14.5 \text{ mA}/\text{cm}^2$  at  $\sim 1.6 \text{ V}/\mu\text{A}$  when deposition was done with a heat-treated substrate and incident microwave was attenuated before reaching it. It is seen that heat-treatment resulted in migration of Cr and Fe oxides towards the top surface which completely changes substrate morphology. It is also seen that the presence of clearer grain boundaries that are created during heat-treatment helps in formation of transition metal nanoparticles more efficiently. Microwave attenuation reduces reflection of microwaves from the substrate and increases residence time of the precursor over the substrate promoting high density growth of CNTs. A schematic model is proposed suggesting that when the decomposed species reach the substrate their residence time increases due to the presence of the attenuator over it. Also, sputtered out decomposed precursor is reflected back to the substrate surface by the attenuator. This increases the chance of carbon radicals to get dissolved in the freshly produced transition metal nano structures causing increase in nucleation density for formation of CNTs on the substrate. Also carbon radicals have more time to form crystalline structure and formation of amorphous soot becomes almost non-existent. The combination of heat-treated substrate and microwave attenuator parameters resulted in growth of long, dense CNTs with bamboo-like defects that contributes to enhanced current density in our field emission studies. It also makes it possible to achieve high field enhancement factor (FEF) ( $\sim 6740$ ) at a low turn on electric field of ( $\sim 0.65 \text{ V}$ ) [4].

Chapter 5 deals with the novel concept of co-deposition of different carbon nanostructures in a single experiment. Co-deposition of CNTs along with nanocrystalline diamond and graphene nanowalls (GNWs) were made possible by MPECVD technique. CNTs have been grown directly on Inconel while other nanostructures could be grown on the Si microwave attenuator placed above Inconel. The detailed mechanism involving co-deposition of  $sp^3$  and different  $sp^2$  hybridized nanostructures has been investigated through a series of experiments and windows for co-deposition have been determined. Deposited samples were characterized by SEM, TEM, Raman spectroscopy and Raman imaging. Characterization results revealed that substrate surface preparation, carbon precursor feeding rate and deposition time are the deciding factors for growth of a particular type of nanostructure. When an unscratched Si surface is used as attenuator with comparative high flow rate of precursor gas (20 SCCM in this case), it is seen that GNWs can be grown on the attenuator along with CNTs. But if a scratched Si surface is used with relatively lower precursor flow rate (5 SCCM in this case), NCD can be obtained along with CNTs. Raman spectroscopic results showed that GNWs behave like nano form of turbostratic graphite and it was seen that they could be deposited even when plasma is highly perturbed. Optical emission spectroscopy results indicated that an increase in the intensity of C2 swan band leads to the increase in the deposition rate of graphitic nanostructures but this fast deposition rate also leads to deposition of unwanted graphitic structures like amorphous carbon soot. The role of plasma sheath in co-deposition has been explained qualitatively with the help of a schematic model. It shows that, one needs to make sure that all the different substrates must be placed inside plasma sheath for co-deposition and feeding rate of

carbon containing precursor should be low to avoid formation of unwanted carbon based structures [17].

Chapter 6 is the final chapter of the thesis which summarizes all the work carried out and also proposes investigations to be taken up in future. In future this work can be progressed both in experimental and simulation domains. Effect of microwave attenuation on CNTs and other nanostructures can be explored by replacing Si with other possible attenuators such as  $\text{Al}_2\text{O}_3$ . Also, the deposited CNTs and CNWs can be tried for fabrication of supercapacitor. In the realm of simulation it will be interesting to take up co-deposition mechanism and try to see how it actually happens and what microscopic parameters effect its growth.

## References

- [1] J.E. Butler, Y.A. Mankelevich, A. Cheesman, J. Ma, M.N.R. Ashfold, J.Phys: Condens. Matter 21 (2009) 364201 (20 pp).
- [2] S. Iijima, Nature 354 (1991) 56–58.
- [3] P. Jarillo-Herrero, J.A. Van Dam, L.P. Kouwenhoven, Nature 439 (2006) 953–956.
- [4] R.Kar, S.G. Sarkar, C.B. Basak, A. Patsha, S. Dhara, C. Ghosh et al. Carbon 94 (2015) 256-265.
- [5] T. Machino, W. Takeuchi, H. Kano, M. Hiramatsu, M. Hori, Appl. Phys. Express 2 (2009) 025001.
- [6] O. Tanaike, N. Kitada, H. Yoshimura, H. Hatori, K. Kojima, M. Tachibana, Solid State Ionics 180 (2009) 381-385.
- [7] Y. Wu, B. Yang, B. Zong, H. Sun. Z. Shen, Y. Feng, J. Mater. Chem. 14 (2004), 469-477.



- [8] S. A. Barve, N. S. Nandurkar, N. Chand, S. B. Singh, N. Mithal, Jagannath, B. M. Bhanage, D. S. Patil, L. M. Gantayet, J. Phys.: Conf. Ser. 114 (2008) 012045.
- [9] E. Luais, M. Boujtita, A. Gohier, A. Tailleur, S. Casimirius, M. A. Djouadi, A. Granier, P. Y. Tessier; App. Phys. Lett, 95 (2009) 014104 (3 pp).
- [11] W. Chen, X. Lu, Q. Yang, C. Xiao, R. Sammynaiken, J. Maley et al. Thin Solid Films 515 (2006) 1970–1975.
- [12] S. Talapatra, S. Kar, S.K. Pal, R. Vajtai, L. Ci, P. Victor et al. Direct growth of aligned carbon nanotubes on bulk metals, Nature Nanotech. 1 (2006) 112-116.
- [13] W.Yi, Q. Yang, CVD growth and field electron emission from of aligned carbon nanotubes on oxidized Inconel plates without addition of catalyst, Diam. Rel. Mat. 19 (2010) 870-874.
- [14] M. Ali, M. Ürgen, Solid State Sciences 14 (2012) 150-154.
- [15] C.H. Lin, S.H. Lee, C.M. Hsu, C.T. Kuo, Diamond & Related Materials 13 (2004) 2147–2151.
- [16] R. Kar, N.N. Patel, S.S. Chopade, S. Mukherjee, A.K. Das, D.S. Patil, J. Exp. Nanosci. 9 (2014) 575-581.
- [17] R.Kar, N.N. Patel, N.Chand, Shilpa R. K., R. O. Dusane, D.S. Patil, S.Sinha, Carbon, 106 (2016) 233-242.

**Publications in Refereed Journal:**

- a. Published: 03
- b. Accepted: X
- c. Communicated: X
- d. Other Publications: 09

Signature of Student:

Date:

*Rajis Das*  
*11/01/2017*

**Doctoral Committee:**

S. No.	Name	Designation	Signature	Date
1.	Prof. Saibal Basu	Chairman	<i>Saibal Basu</i>	11/1/17
2.	Prof. Sucharita Sinha	Guide/ Convener	<i>Sucharita Sinha</i>	11/1/2017
3.	-----	Co-guide (if any)		
4.	Prof. D.S. Patil	Member	<i>D.S. Patil</i>	
5.	Prof. Sudhir Kapoor	Member	<i>Sudhir Kapoor</i>	11/1/17
6.	-----	Member		

Enclosure: Annexure-I (list of publications)

# CONTENTS

	<b>Page No.</b>
<b>SYNOPSIS</b>	<b>i-xi</b>
<b>LIST OF FIGURES:</b>	
<b>Figure 1.1:</b> Dimensions of different objects in nanometers.	<b>4</b>
<b>Figure 1.2:</b> Schematic showing how graphene sheet/ sheets get converted into SWCNT (above) and MWCNT (below).	<b>6</b>
<b>Figure 1.3:</b> Schematic showing emergence of three different types of SWCNT from rolling of grapheme sheet. Rolling the sheet along blue axis results in formation of zigzag CNTs and rolling along the red line results in armchair type. Rolling the tube along any other direction (like the black line) results in the formation of chiral CNTs.	<b>7</b>
<b>Figure 1.4:</b> Schematic showing the structure of CNWs on a substrate.	<b>10</b>
<b>Figure 1.5:</b> SEM image showing a sample having presence of both diamond and NCD.	<b>10</b>
<b>Figure 1.6:</b> Schematic of DC plasma discharge system.	<b>15</b>
<b>Figure 1.7:</b> Schematic of (a) inductively coupled RF discharge plasma system, (b) capacitively coupled RF discharge plasma system.	<b>17</b>
<b>Figure 1.8:</b> Schematic of a low pressure microwave discharge plasma system.	<b>19</b>
<b>Figure 1.9:</b> Schematic of a low pressure microwave ECR discharge plasma system.	<b>20</b>
<b>Figure 1.10:</b> Schematic of a scanning electron microscope [30].	<b>26</b>
<b>Figure 1.11:</b> Schematic of a (a) transmission electron microscope, (b) principle of imaging and diffraction pattern. [30]	<b>28</b>
<b>Figure 1.12:</b> Schematic of a typical Raman spectroscopy system.	<b>30</b>
<b>Figure 1.13:</b> Schematic of a typical OES set-up.	<b>32</b>
<b>Figure 1.14:</b> Schematic of a typical XRD set-up.	<b>33</b>

<b>Figure 2.1:</b> Schematic of the ECR-PECVD facility [1].	<b>43</b>
<b>Figure 2.2:</b> Variation of magnetic field profile with axial distance. [2].	<b>43</b>
<b>Figure 2.3:</b> Schematic diagram of the MPECVD set up used for the deposition of CNTs [5].	<b>45</b>
<b>Figure 3.1:</b> Schematic of the ECR-PECVD facility used for deposition of CNWs.	<b>51</b>
<b>Figure 3.2:</b> SEM image of the deposited four samples of CNWs.	<b>53</b>
<b>Figure 3.3:</b> A typical EDS spectrum of the deposited CNWs.	<b>53</b>
<b>Figure 3.4:</b> (a) Typical HRTEM image of deposited CNWs, (b) measurement of inter-layer spacing between two graphene sheets.	<b>54</b>
<b>Figure 3.5:</b> Raman spectrum of the deposited four samples of CNWs.	<b>56</b>
<b>Figure 3.6:</b> (a) Typical SEM image showing formation of Ni nano-islands after plasma pre-treatment of Ni thin film, (b) histogram plot of dimensions of Ni nano-islands, (c) Sporadic presence of nano-islands marked by yellow circles in SEM image of CNWs.	<b>57</b>
<b>Figure 3.7.</b> SEM images of two typical flower-like patterns obtained during deposition of CNWs.	<b>59</b>
<b>Figure 3.8.</b> Electronic polarizability vs. wavelength plot for Ni.	<b>60</b>
<b>Figure 3.9:</b> Schematic representation of different stages during growth of CNWs by ECR-CVD.	<b>62</b>
<b>Figure 4.1:</b> Actual photograph of MPECVD system used during the experiments.	<b>68</b>
<b>Figure 4.2:</b> (a) SEM image of the as-received Inconel substrate, (b) As-received Inconel substrate after H <sub>2</sub> plasma pre-treatment, (c) SEM image of CNTs grown in sample A, (d) SEM image Inconel substrate heat-treated at 1100°C, (e) SEM image of heat-treated Inconel substrate after H <sub>2</sub> plasma pre-treatment, (f) FESEM image of CNTs grown in sample B, (g) FESEM image of CNTs grown in sample C; inset image showing low resolution SEM image for this sample, (h) Histogram plot of diameter distribution of CNTs grown for all three samples.	<b>72</b>

<b>Figure 4.3:</b> (a) TEM image of sample A showing large metal particles along with CNTs, (b) HRTEM image of sample A showing hollow core and defects marked by arrows, (c) HRTEM image of sample B showing clusters of CNTs with varied diameter distribution, (d) HRTEM image of a CNT in sample B showing defect on the wall of the tube (marked by arrow) and presence of trapped metal nanoparticle inside the core, (e) HRTEM image of CNTs in sample C showing large number of CNTs, bamboo like defect shown by arrows, (f) bamboo-like defect shown in a CNT marked by arrows in sample C, (g) STEM-XEDS analysis of a typical metal nanoparticle showing presence of Ni & Fe in nanoparticles.	<b>74</b>
<b>Figure 4.4:</b> Comparison of XRD spectrum of as-received and heat-treated Inconel substrate.	<b>76</b>
<b>Figure 4.5:</b> Deconvoluted micro-Raman image of samples A, B & C showing presence of D, G and D' peaks.	<b>77</b>
<b>Figure 4.6:</b> Schematic diagram of field-emission set-up used in the experiment.	<b>80</b>
<b>Figure 4.7:</b> (a) J vs. E plot for sample A, B & C. Inset image showing $\ln J$ vs. $1/E$ plot for three samples, (b) Variation of Turn-on voltage vs. Field enhancement factor for samples A, B and C.	<b>82</b>
<b>Figure 4.8:</b> EDS spectrum of the heat-treated Inconel substrate with elemental composition of different elements present.	<b>85</b>
<b>Figure 4.9:</b> (a) Photograph of Inconel substrate with Si wafer on top, (b) Schematic diagram showing how reflector helps in increased deposition rate of CNTs.	<b>89</b>
<b>Figure 5.1:</b> Actual photograph of experimental condition for CNT deposition inside MPECVD reactor.	<b>100</b>
<b>Figure 5.2:</b> (a) FESEM image of CNTs deposited in experiment 1, (b) SEM image of the Si attenuator used in the experiment 1, (c) SEM image of the NCD and MCD deposited in the experiment 2, (d) SEM image of octahedral diamond crystals deposited in experiment 3, (e)	<b>106</b>

SEM image of the defective MCD crystals deposited in the experiment 3, (f) SEM image of the CNTs deposited in the experiment 4, (g) SEM image of the CNTs deposited in the ball shape in experiment 4, (h) SEM image of the GNWs deposited on the Si attenuator in the experiment 4, (i) SEM image of the CNTs deposited in the experiment 5 along with micron sized larger diameter tubes and thicker bunches, (j) magnified SEM image of the CNTs deposited in the experiment 5, (k) SEM image of GNWs deposited in ball shape on the Si attenuator in the experiment 5, (l) SEM image of the CNTs deposited in the experiment 6, (m) FESEM image of the CNTs deposited in the experiment 6 showing formation of defect free CNTs, (n) SEM images of the NCDs deposited on the Si attenuator in the experiment 6, (o) SEM image of the Si attenuator showing the diamond formation along the scratch marked tracks, (p) SEM image of the reused Si attenuator previously used in the experiment 5. It shows removal of ball shaped GNWs and presence of diamond particles on it.

**Figure 5.3:** Actual photograph of the plasma condition inside the reactor in experiment 4. **107**

**Figure 5.4:** (a) HRTEM image of the CNTs deposited in experiment 5, (b) HRTEM image of CNTs deposited in experiment 6, (c) HRTEM image of typical bamboo-like defects seen inside the tubes in experiment 5 and 6, (d) Typical TEM image of GNWs deposited in experiment 4 and 5, (e) HRTEM image of GNWs deposited in experiment 4, (f) HRTEM image of GNWs deposited in experiment 5. **109**

**Figure 5.5:** (a) Typical Raman spectrum of deposited MCD films in experiment 2 and 3, (b) Raman spectrum of GNWs deposited on Si attenuator in experiment 4 between  $1100-1800\text{ cm}^{-1}$ , (c) Raman spectrum of GNWs deposited on Si attenuator in experiment 4 between  $2500-2800\text{ cm}^{-1}$ , (d) Raman spectrum of GNWs deposited in **112**

ball shape on Si attenuator in experiment 5 between 1200-1850  $\text{cm}^{-1}$ , (e) Raman spectrum of GNWs deposited in ball shape on Si attenuator in experiment 5 between 2500-2900  $\text{cm}^{-1}$ , (f) Raman spectrum of NCD films deposited on Si attenuator in experiment 6.

**Figure 5.6:** (a) Optical microscopic image of the particle taken for Raman imaging, (b) Raman imaging of the particle for 1333  $\text{cm}^{-1}$ , (c) Raman imaging of the particle with 1547  $\text{cm}^{-1}$ . **113**

**Figure 5.7:** (a) OES spectrum of the plasma taken during experiment 5, (b) OES spectrum of the plasma taken during experiment 6. **114**

**Figure 5.8:** (a) Schematic representation of the condition of the plasma over the Si attenuator in experiment 4, (b) schematic representation of scratched Si attenuator used in experiments 5 and 6, (c) Schematic of deposition condition inside MPECVD chamber with presence of Si attenuator inside plasma sheath. **119**

**Figure 5.9:** Actual photograph of the deposition (a) after 30 minutes, (b) after 40 minutes, (c) after 55 minutes; (d) actual photograph of the Si attenuator after it was taken out of the chamber, (e) SEM image of the deposited black mass on the Si attenuator showing presence of the GNWs. **121**

#### **LIST OF TABLES:**

**Table 1.1:** Different types of characterization techniques and their usefulness. **22**

**Table 4.1:** Raman spectroscopic measurement data for three samples. **79**

**Table 5.1:** Details of experiments conducted for the co-deposition of different carbon structures. **101**

**Table 5.2:** Raman spectroscopic measurement of data of GNW samples. **113**

<b>CHAPTER 1</b>	<b>Introduction</b>	<b>1-40</b>
	<b>1.1 Nanotechnology</b>	<b>2</b>
	<b>1.2 Carbon nanostructures</b>	<b>4</b>
	1.2.1 Carbon nanotubes (CNTs)	5
	1.2.2 Carbon nanowalls (CNWs)	9
	1.2.3 Nanocrystalline diamond (NCD)	10
	<b>1.3 Plasma</b>	<b>11</b>
	<b>1.4 Non-thermal plasma sources</b>	<b>14</b>
	1.4.1 Direct current (DC) discharge plasma	14
	1.4.2 Radio frequency (RF) discharge plasma	15
	1.4.3 Low pressure microwave plasma	18
	1.4.4 Microwave Electron-cyclotron resonance (ECR) plasma	19
	<b>1.5 Characterization technique</b>	<b>22</b>
	1.5.1 scanning electron microscopy (SEM)	24
	1.5.2 Transmission electron microscopy (TEM)	26
	1.5.3 Raman spectroscopy	28
	1.5.4 Energy dispersive X-ray spectroscopy (EDS)	30
	1.5.5 Optical emission spectroscopy (OES)	31
	1.5.6 X-ray diffraction (XRD)	32
	<b>1.6 Scope of the thesis &amp; associated     literature survey</b>	<b>33</b>
	<b>References</b>	<b>36</b>
<b>CHAPTER 2</b>	<b>Experimental Details</b>	<b>41-48</b>
	<b>2.1 ECR-PECVD system</b>	<b>41</b>



	<b>2.2 MPECVD system</b>	<b>44</b>
	<b>2.3 Choice of substrates and substrate preparation methods</b>	<b>45</b>
	2.3.1 Preparation of Si substrate for CNW/GNW deposition by ECR-CVD	<b>46</b>
	2.3.2 Preparation of Si substrate for CNW/GNW & NCD deposition by MPECVD	<b>46</b>
	2.3.3 Preparation of Inconel 600 substrate for CNT deposition by MPECVD	<b>47</b>
	References	<b>48</b>
<b>CHAPTER 3</b>	<b>Deposition and Characterization of Carbon Nanowalls synthesized by ECR-CVD Method</b>	<b>49-64</b>
	<b>3.1 Introduction</b>	<b>49</b>
	<b>3.2 Experimental details</b>	<b>50</b>
	<b>3.3 Results</b>	<b>52</b>
	<b>3.4 Discussion</b>	<b>56</b>
	<b>3.5 Conclusion</b>	<b>62</b>
	References	<b>62</b>
<b>CHAPTER 4</b>	<b>Deposition, Characterization and Field Emission Studies on Multi-walled Carbon Nanotubes by MPECVD Method</b>	<b>65-93</b>
	<b>4.1 Introduction</b>	<b>65</b>
	<b>4.2 Experimental</b>	<b>67</b>
	<b>4.3 Characterization results</b>	<b>70</b>
	4.3.1 Electron microscopy	<b>70</b>
	4.3.2 X-ray diffraction (XRD)	<b>75</b>
	4.3.3 Raman spectroscopy	<b>76</b>
	4.3.4 Field emission measurement	<b>80</b>
	<b>4.4 Discussion</b>	<b>82</b>
	<b>4.5 Conclusion</b>	<b>90</b>

	References	90
<b>CHAPTER 5</b>	<b>An Investigation on the Co-deposition Mechanism of Different Carbon Nanostructures by MPECVD Method</b>	<b>94-125</b>
	5.1 Introduction	94
	5.2 Experimental	98
	5.3 Characterization results	103
	5.4 Discussion	114
	5.5 Conclusion	122
	References	122
<b>CHAPTER 6</b>	<b>Conclusion and Future Scope</b>	<b>126-128</b>
	6.1 Conclusion	126
	6.2 Future Scope	128

# **Chapter 1**

## **Introduction**

Nanotechnology is undoubtedly one of the most researched fields of science in present times. Its numerous promising applications have led researchers all around the world to work on different nanomaterials. Among the vast realm of nanomaterials carbon nanostructures have gained considerable attention due to their enviable range of potential applications from mechanics to medicine. Different routes are being explored to synthesize carbon nanostructures each having its own advantages and drawbacks. Plasma enhanced chemical vapour deposition (PECVD) or simply plasma processing is one of the popular tools of today for synthesis of different carbon nanostructures. This thesis reports about the investigations and obtained results from plasma processing of different carbon nanostructures and their physical properties. Three different types of carbon nanostructures have been discussed in this thesis; they are carbon nanotubes (CNTs), carbon nanowalls (CNWs) and nano-crystalline diamonds (NCDs). Their synthesis has been done using microwave electron-cyclotron resonance (ECR) plasma chemical vapor deposition (CVD) and microwave plasma enhanced (MPE) CVD techniques. While ECR-CVD was employed for deposition of CNWs alone, MPECVD has been used to deposit all three types on nanostructures depending on prevailing experimental conditions. Any synthesized nanostructures must undergo characterization to ensure that the deposited structure qualifies as ‘nano’ and that properties of the deposited structure hold promise for potential applications. Here, deposited structures have been characterized by different characterization techniques to study their morphology, chemical bonding and other physical properties like field emission behavior. In addition to characterization of the deposited films,

plasma has also been characterized by optical emission spectroscopy (OES) and plasma properties have been correlated with the properties of deposited nanostructures.

This chapter gives a brief introduction and an overview of the topics covered in this thesis. A brief introduction to nanotechnology is given at the first followed by short discussion on different carbon nanostructures and their applications. One section is dedicated next to discuss plasma and different PECVD techniques which can be used for plasma processing. Working principles, instrumentations and usefulness of different characterization techniques used in this thesis are included in a separate section. Finally, motivation for this present work, its scope and thesis organization is discussed for completeness.

## **1.1 Nanotechnology**

As stated earlier, nanotechnology is one of the most researched and widely explored field of science. The amazing power of nanotechnology is being widely exploited to make life simpler and safer. The word ‘nano’ originates from the Greek word nanos meaning dwarf. Nano refers to a scale of  $10^{-9}$  m and typically any object with a dimension less than 100 nm is qualified as “nano material” following the definition used by the National Nanotechnology Initiative in the US. Research in Nanotechnology essentially began with the famous lecture of Prof. Richard Feynman in 1959 titled “There’s plenty of room at the bottom” at Caltech in December 1959. Feynman had described a process by which the ability to manipulate individual atoms and molecules might be developed. In the course of this, he noted, scaling issues would arise from the changing magnitude of various physical phenomena: gravity would become less important, surface tension and Van der Waals interaction would become more important [1]. Experiments in nanotechnology got a major boost in the

80's through the invention of scanning tunneling microscope (STM). The surge came immediately after the discovery of fullerenes in 1985 by Harry Kroto, Richard Smalley, and Robert Curl, who together won the 1996 Nobel Prize in Chemistry. Fullerene was later attributed the title of third allotrope of carbon after diamond and graphite.

Many exciting changes in the materials have been observed when their dimension diminishes to nanoscale. These include statistical mechanical as well as quantum mechanical effects. Quantum effects can become significant when the nanometer size range is reached. Band structure of solid then changes into simpler atomic model with continuous electronic bands becoming discrete. This leads to interesting changes in the electrical properties of the material. Additionally, a number of physical (mechanical, optical, etc.) properties change when compared to macroscopic systems. One example is the increase in surface area to volume ratio altering mechanical, thermal and catalytic properties of materials. Diffusion and surface reactions at nanoscale, nanostructured materials and nanodevices become faster with fast ion transport. Materials reduced to the nanoscale show different properties compared to what they exhibit on a macroscale, enabling unique applications. For instance, opaque copper becomes transparent in nanoscale, Aluminium becomes combustible, gold becomes soluble and also turns into an active chemical catalyst in nanoscale. Much of the fascination with nanotechnology stems from these quantum and surface phenomena that matter exhibits at the nanoscale. Figure 1.1 shows comparative dimensions of different objects on a nanometer scale.

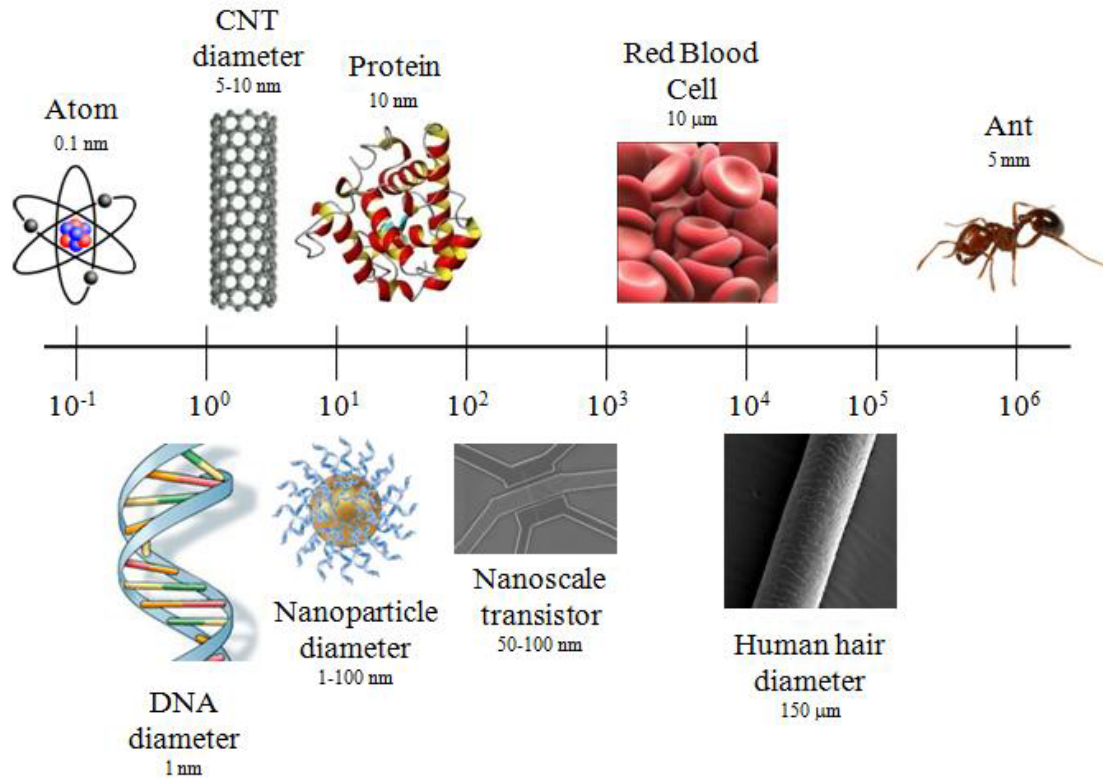


**Figure 1.1:** Dimensions of different objects in nanometre [2].

## 1.2 Carbon nanostructures

Carbon has six electrons that occupy the  $1s^2$ ,  $2s^2$  and  $2p^2$  orbitals. The core  $1s^2$  electrons are strongly bound whilst the remaining weakly bound four valence electrons undergo quantum mechanical orbital hybridization to form  $sp^1$ ,  $sp^2$  and  $sp^3$  bonds. Under ambient conditions graphite and diamond are the well known thermodynamically stable forms of carbon allotropes having  $sp^2$  and  $sp^3$  hybridization respectively. Carbon has become one of the most researched elements in recent times since the advent of nanotechnology. The worldwide interest in carbon nanostructures is primarily due to two reasons. First is the exciting range of potential applications that these materials offer and second is the easy availability of carbon making it a cheaper source material to start with. Since the discovery of buckyballs or fullerene in 1985 research in carbon nanostructures has leapfrogged to a new level altogether. The

tremendous improvement of electron microscopy has made it possible to observe novel carbon nanostructures, such as fullerenes, nano crystalline diamond (NCD), carbon nanowalls (CNWs), nanowires and carbon nanotubes (CNTs). Following subsections discuss the three carbon nanostructures that have been deposited in the course of this work.

### ***1.2.1 Carbon nanotubes (CNTs)***

A CNT is basically a sheet of graphene rolled into a seamless cylinder. It may be capped with half of a buckyball at both ends but it may also be capped with metal nanoparticles or remain uncapped. CNTs are majorly divided into two categories depending on the number of cylinders around the central axis of the tube. When a single sheet of graphene is rolled into a cylinder then single-walled CNT (SWCNT) is formed and when multiple graphene sheets are rolled together then multi-walled CNT (MWCNT) is formed. CNTs are graphitic in nature and they are  $sp^2$  hybridized nanostructures. Since their discovery in 1991 by S. Ijima [3] CNTs have offered a lot of promising applications in diverse fields ranging from electronics to medicine [4]. They boast a diverse set of exotic and valuable properties. CNTs are stronger than steel and harder than diamond but can be as flexible as cotton; they are light-weight, transparent and hold unparalleled capacity for conducting electrical or thermal energy. Due to their excellent electron emission properties CNTs have a strong potential application as a cold cathode [5, 6]. Figure 1.2 shows schematics of SWCNT and MWCNT together. The schematic shows how a single graphene cylinder when rolled gets converted into a SWCNT and when multiple graphene cylinders are rolled together they transform into a MWCNT.

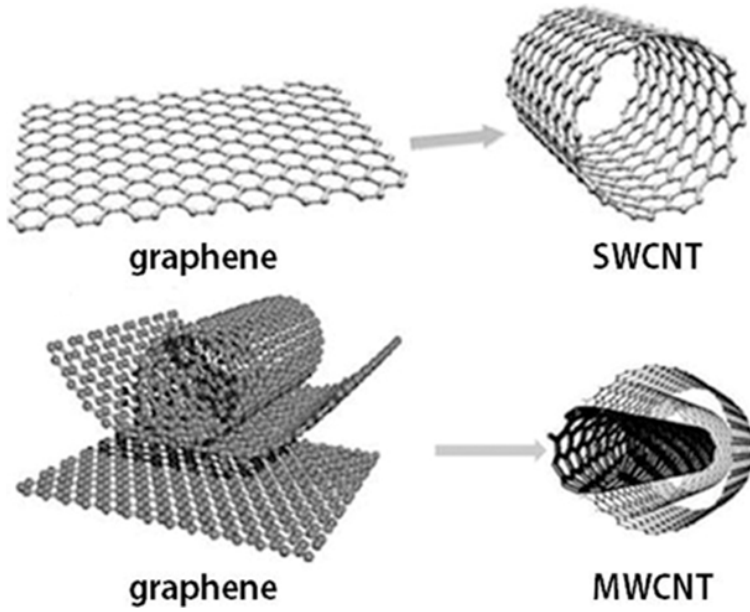


**Figure 1.2:** Schematic showing how graphene sheet/ sheets get converted into SWCNT (above) and MWCNT (below) [7].

SWCNTs have again been divided into three distinct classes depending on how the graphene cylinder is rolled. A chiral vector  $\mathbf{c}$  has been defined on the basis of two unit vectors  $\mathbf{a}$  and  $\mathbf{b}$  of hexagonal lattice as  $\mathbf{c} = m\mathbf{a} + n\mathbf{b}$ , where  $m, n$  are integers. Based on the value of  $m$  and  $n$ , a rolled cylinder of SWCNT can be called as armchair ( $m=n$ ), zigzag ( $m=0$ ) or chiral ( $m \neq n$ ). Figure 1.3 shows a detailed schematic representing these three types of SWCNTs. Chirality controls the electronic properties of SWCNTs, it is found that armchair nanotubes are always metallic while other two can either be metallic or semiconducting depending on the values of  $m$  and  $n$ . If  $n - m$  is a multiple of 3, then the nanotube is semiconducting with a very small band gap, otherwise the nanotube is a moderate semiconductor with a band gap of  $\sim 2$  eV [6]. For practical purposes, most SWCNTs are found to be chiral after deposition. Also, it has to be understood that deposition of SWCNTs is more difficult than deposition of



MWCNTs. Deposition of the latter is easier to control though both single and multi-walled CNTs are commercially available.

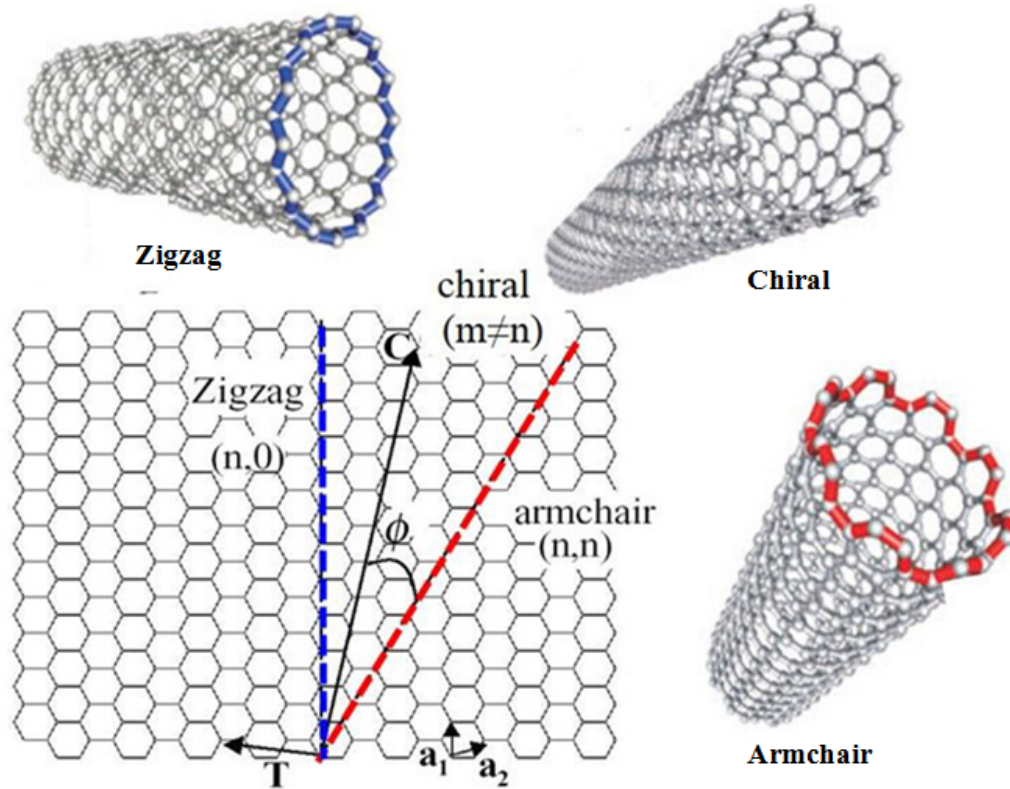


**Figure 1.3:** Schematic showing emergence of three different types of SWCNT from rolling of graphene sheet. Rolling the sheet along blue axis results in formation of zigzag CNTs and rolling along the red line results in armchair type. Rolling the tube along any other direction (like the black line) results in the formation of chiral CNTs [8].

Till now, researchers have employed several techniques to produce CNTs among which arc discharge, chemical vapor deposition (CVD), plasma enhanced chemical vapour deposition (PECVD) and laser ablation are prominently employed methods. There are reports of using arch discharge to produce high quality SWCNTs

with impressively narrow distribution in diameter averaging about 1.4 nm [9]. However, arc discharge or laser ablation mostly produce randomly mixed and tangled nanotubes with byproducts, such as fullerenes, graphitic polyhedra with enclosed catalytic metal particles and amorphous carbon in the form of particles. These preparation methods provide only very limited control over dimensions (length and diameter) of the CNTs. Most importantly, the production cost of CNTs are high and the experimental setup cannot easily be scaled up for plant scale production of CNTs. To overcome these difficulties alternative possibilities have been explored and CVD has been found to be a promising technique to circumvent the problems.

The CVD method has long been used since the 1970s to produce carbon fibers [10] and the method has been successfully modified to meet the requirements for synthesis of CNTs. Compared with arc discharge and laser ablation methods, the CVD method can produce CNTs in bulk quantity both in powder form and on flat surfaces. Controlling the deposition parameters is also easier in CVD by tuning a variety of parameters such as temperature, carbon feed and catalyst. CVD by far is one of the routinely used methods nowadays for the production of CNTs as it is efficient and economical for large scale production of CNTs. Though CVD seems to be a good solution for bulk production of CNTs, the method uses temperature in the range of 800-1000°C. This turns out to be a major hindrance in cases where CNTs are required to be directly synthesized on plastic substrates for applications like nano-electronics where the processing temperature has to be kept below 500°C [11]. Temperature limitation of CVD can be done away by using PECVD technique. This technique uses plasma as the medium for CVD and since plasma has abundant source of energetic ions and electrons, it lowers the requirement of high process temperature. Hence,

PECVD and particularly low-pressure PECVD technique has emerged as the chosen tool for deposition of CNTs in recent years. It can also be safely said that, advantages of PECVD particularly its requirement of low process temperature and availability of large number of tunable parameters has made this technique the most popular technique for the deposition of any type of carbon nanostructures.

### ***1.2.2 Carbon nanowalls (CNWs)***

Carbon nanowalls (CNWs) are another type of graphitic nanostructures that stand on the substrates surface like a wall. Figure 1.4 shows a schematic of CNW which gives a basic idea about its structure. In most of the cases, CNWs basically consist of a number of graphene sheets which is also the reason for calling CNWs as graphene nanowalls (GNWs) sometimes. CNWs were first discovered by Wu et al in 2002 during the growth experiment of CNTs by MPECVD technique [12]. Since then, CNWs/ GNWs have been prepared by various methods including radio-frequency PECVD (rf-PECVD) [13], dc-PECVD [14] and electron-cyclotron resonance PECVD (ECR-PECVD) [15, 16].

It is a relatively newer nanostructure of Carbon compared to more famous CNT and it is therefore also relatively less explored. Till now, researchers around the world have found several potential applications of this nanostructure like a catalyst support structure for fuel cell [17], an electrode for lithium ion battery [18] and as a field emission device [19].

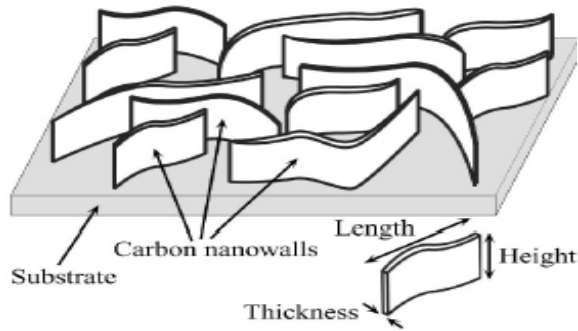


**Figure 1.4:** Schematic showing the structure of CNWs on a substrate [20].

### 1.2.3 Nanocrystalline diamond (NCD)

As the name suggests nanocrystalline diamonds (NCDs) are actually diamond crystals having dimension not more than 100 nm. Unlike the graphitic nanostructures like CNTs or CNWs, NCDs are  $sp^3$  hybridized in nature. Figure 1.5 shows a scanning electron microscopic image of a diamond surface showing presence of both diamond and NCD. Clear 110 planes of diamonds are seen in the image and two of such planes are pointed by an arrow. One region with NCDs is also marked by a circle in the figure.

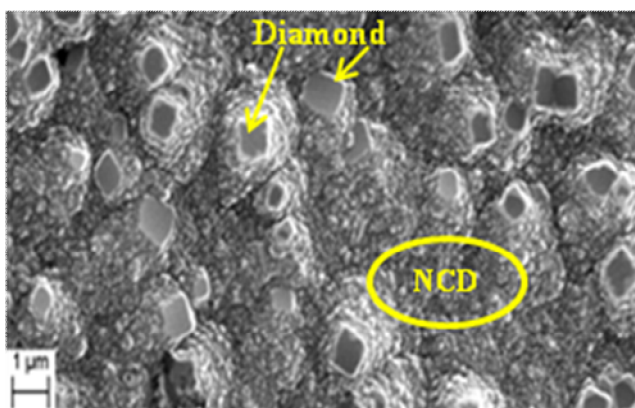


**Figure 1.5:** SEM image showing a sample having presence of both diamond and NCD.

NCD films are easier to synthesize compared to polycrystalline or single crystal diamond films but it does possess most of the important properties of a single crystal diamond film. NCD films possess a lower friction characteristic and higher transparency [21] in addition to the inherent properties of diamond films, such as high hardness, negative electron affinity, high thermal conductivity and high chemical resistance [22, 23]. These inherent properties of these films make them great potential materials for applications in the fields of protective coating, field emission devices and cutting tools [24, 25]. Studies have also been conducted on their non-cytotoxicity which makes them a good choice for biomedical applications, such as artificial heart valves, cardiovascular surgery, catheter ablation, and bioMEMS. NCD films are usually synthesized using a CVD/ PECVD technique via decomposition of a carbon containing gas. The gas decomposition can be activated by a hot metal filament, combustion flame or plasma discharge [26]. Microwave plasma enhanced CVD (MPECVD) has been widely employed for synthesis of NCD films as its operational regime is ideal for diamond / NCD deposition.

### **1.3 Plasma**

Nearly 99.99% of the universe consists of plasma and we live in the other 0.01% of the universe. Plasma is classified as the fourth state of matter consisting of ions, electrons and neutrals. The word 'plasma' is derived from the Greek word *plásma* meaning something that can be molded or fabricated. Presence of plasma in everyday life can be felt through the flash of lightning bolt, in the soft glow of fluorescent lamps, and bright neon signs seen at night. Plasma is present in the stellar interiors, atmosphere, and gaseous nebulae.

Plasma is generally defined as an assembly of electrons, ions and neutrals having quasi-neutrality and collective behavior [27]. Quasi-neutrality means that plasma can possess local microscopic electric field but overall charge neutrality always prevails. Collective behavior arises from the long distance Coulomb force where one part of plasma is closely affected by the changes in another part of the system with overall quasi-neutrality being readily attained. For plasma based processing in laboratory two plasma parameters are very noteworthy, namely, plasma potential and number density of plasma.

Since plasma is quasi-neutral, it has equal number of electrons and ions. But electrons being more mobile will always escape to the wall and to maintain the quasi-neutrality, ions in the plasma also get attracted to the walls and centre of the plasma thus acquires an overall positive potential which is ideally constant throughout the plasma. This potential developed inside plasma due to escape of electrons to the walls is called plasma potential. Also, in a region near the wall quasi-neutrality is disrupted due to the escape of electrons to walls. This region is called plasma sheath. Here ions get accelerated and take part in the deposition. Number density is simply the number of electrons/ions per unit volume of plasma. High number density suggests high degree of ionization inside plasma.

Plasmas are broadly classified into two different types. One is called hot or thermal plasma and the other type is called cold or non-thermal plasma. In thermal plasma ion and electron temperature should ideally be equal and due to high ion temperatures ( $\sim 1$  eV) these plasmas are called hot. Here both ions and electrons follow Maxwell distributions. In non-thermal plasmas ions and electrons have different temperatures. Normally electrons have a very high temperature which may

go as high as 10 eV while ions remain just above the room temperature. Here, both ions and electrons may or may not follow Maxwellian distribution. It is seen that while Maxwell distribution is followed by ions in non-thermal plasmas, electrons follow Druvesteyn distribution [28].

Thermal plasmas are collision dominated in nature with high number density and their steady state population densities can be maintained as per Boltzman relation and distribution of ionization stages are given by Saha equation. This condition is called local thermodynamic equilibrium (LTE) condition. In lower pressures, electron collisions and electron induced dissociations are much more important and ions do not get chance to thermalize through collisions. Due to this reason, electrons and ions in these plasmas attain equilibrium with separate temperatures. These types of non-thermal plasmas never attain LTE condition.

Saha ionization equation (1.1) gives the amount of ionization occurring in a gas at thermal equilibrium.

$$\frac{n_i}{n_n} \approx 2.4 \times 10^{21} \frac{T^{3/2}}{n_i} e^{-U_i/KT} \quad (1.1)$$

Here ( $n_i$ ) and ( $n_n$ ) are the densities (number per  $m^3$ ) of ionized atoms and of neutral atoms,  $T$  is the gas temperature in  $^{\circ}K$ , ( $U_i$ ) is the ionization energy of the gas and  $K$  is the Boltzmann's constant.

From the above equation, it can be seen that at room temperature, the fractional ionization produced is of order of  $n_i/n_n \approx 10^{-122}$  which is extremely low. This fraction becomes considerable only when  $U_i$  becomes few times  $KT$  and the gas reaches plasma state [27].

As high gas temperature is generally associated with LTE systems, these systems are used for applications such as cutting, welding, spraying, etc. In such

systems the plasma power density is in the range of  $100 \text{ W/cm}^3$  -  $10 \text{ KW/cm}^3$  and above whereas non LTE systems are used for various processes such as thin film deposition, surface modification, etching and generally have power density in the range of  $10^{-4}$  to a few tens of watt per  $\text{cm}^3$  [29].

Both of these types of plasmas have been used for material processing. For this work, non-thermal plasmas have been used to deposit carbon nanostructures. There are different types of non-thermal plasma each having their own advantages and disadvantages in terms of material processing. Normally, a particular plasma is chosen for a particular type of material processing depending on its advantages, set-up cost, maintenance cost and ease of handling. Following are some of the commonly used non-thermal plasmas.

#### **1.4 Non-thermal Plasma Sources:**

##### ***1.4.1 Direct Current (DC) discharge plasma***

The configuration of these types of plasma is simple and shown in Figure 1.6. A DC electric field is applied between two electrodes leading to the acceleration of stray electrons. The accelerated electrons then get excited and ionize the atoms through inelastic collisions. The ions bombard the cathode, causing emission of secondary electrons. These electrons are responsible for sustaining the discharge. De-excitation of the charged particles within the visible region causes the discharge to glow. The DC discharge is characterized by different regions as shown in Figure 1.6 and the electric field strength varies from cathode to anode. The region adjacent to cathode is characterized by a strong electric field and it is called cathode dark space. Next is the negative glow region, it is the brightest region of the entire discharge as it has high density of both electrons and ions. When the distance between anode and



cathode is relatively longer, there are two more regions known as the Faraday dark space and the positive column. In Faraday dark space, the electron energy and axial electric field is small. The positive column has low net charge density but sufficient electric field to maintain ionization. The DC discharge can operate over a wide range of pressures from 1 Pa to atmospheric pressure. The voltage used is in the range 300 to 1500 V or more depending on the electrode configuration and the current is in the range of milli ampere.

From material processing point of view, DC plasma is rarely used nowadays as it is quite inefficient, since the lost electrons have to be constantly replenished by the release of secondary electrons into the system. So, plasma densities obtained in the dc discharge are always modest [30].

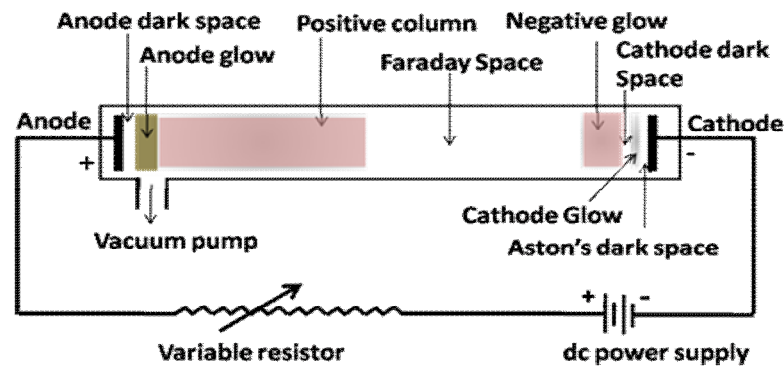


**Figure 1.6:** Schematic of DC plasma discharge system.

#### ***1.4.2 Radio Frequency (RF) discharge plasma***

The limitation of DC discharge arises from the fact that both of the electrodes have to be electrically conducting and it limits deposition of dielectric materials. For such films, deposition will stop due to space charge effect which is called “cathode poisoning”. For plasma processing and deposition of all kinds of films including dielectrics RF plasma provides an effective alternative approach. Here, a varying electric field, typically 13.56 MHz or its integral multiple is applied to the electrodes.

The electrodes alternately change polarity and the accumulated charge can be fully or partially neutralized. There are two different types of configuration for coupling RF power to plasma, one is called inductively coupled plasma (ICP) and the other is capacitively coupled plasma (CCP). Schematic of both the systems are shown in Figure 1.7(a) & (b) respectively. In ICP the RF is fed to helical coils wound axially around a cylindrical, dielectric plasma vessel (usually of quartz). The power is coupled into the discharge via transformer principle and in the MHz frequency range transformer coupling is also efficient. High electron density of  $10^{18} \text{ m}^{-3}$  is one of the hallmarks of ICP but its plasma potential is low. ICPs have been used for different applications such as thin-film deposition, plasma etching and as ion sources for mass spectroscopic analysis [30]. In CCPs power is fed to one of the electrodes through a capacitor while the other electrode is grounded. These devices work in the pressure range of 1 to 10 Pa and typical electron densities obtained in this case is in the range  $10^{15}$ – $10^{16} \text{ m}^{-3}$ . The most important feature of CCP is the development of a large, negative bias on the substrate called self-bias. CCP has lower plasma density in comparison to ICP but compensates it with a high value of plasma potential which may go upto 100 Volts. When this is added to the self bias, it generates a high value of potential and helps to draw ions efficiently towards the substrate for deposition (also causing sputtering if energy is too high). This has a very large number of applications in plasma based material processing. The generation of self-bias voltage on the substrates can be attributed to different response times of electrons and the ions to the applied RF field.

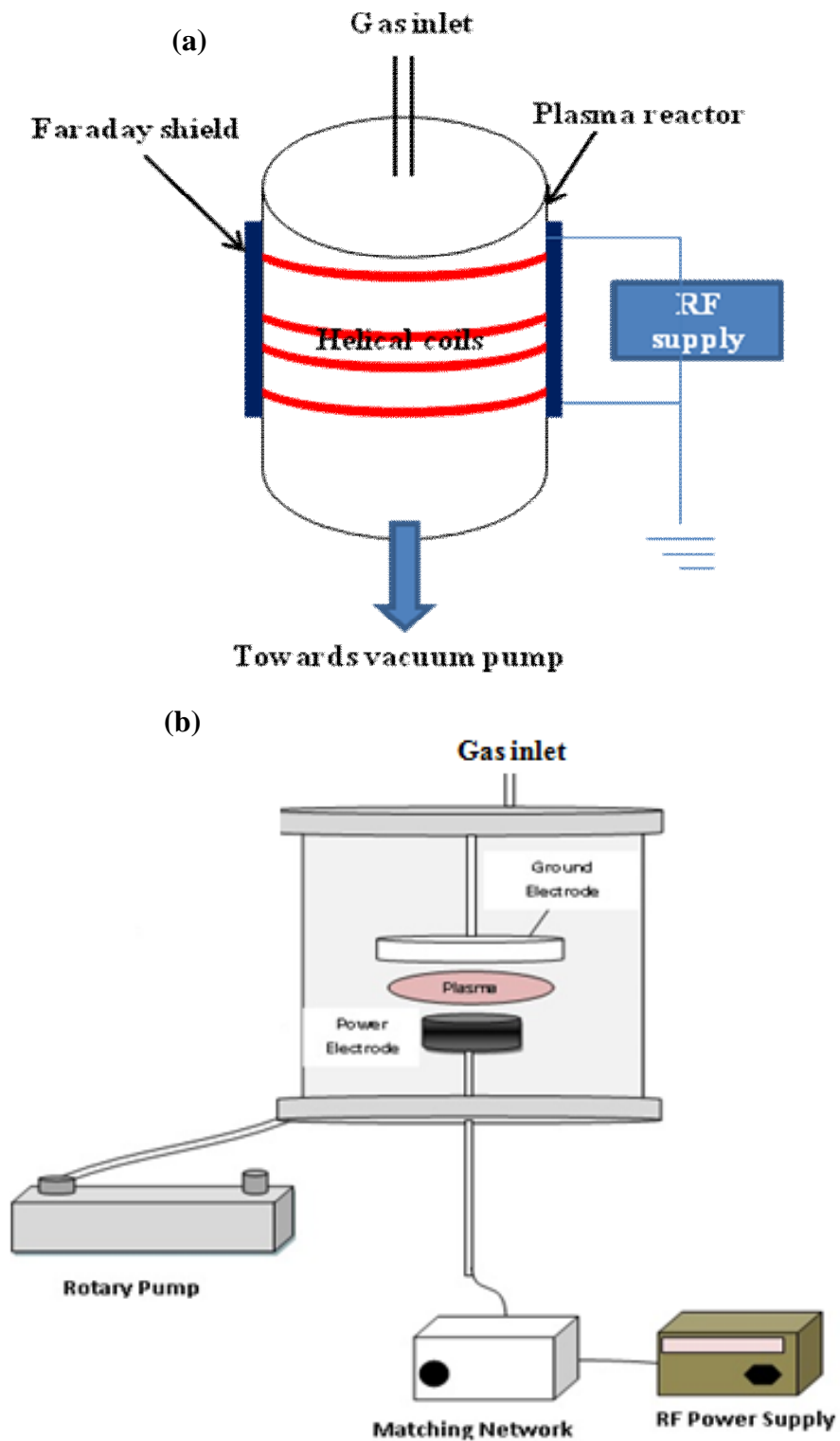


**Figure 1.7:** Schematic of (a) inductively coupled RF discharge plasma system, (b) capacitively coupled RF discharge plasma system.

### ***1.4.3 Low pressure Microwave plasma***

Low pressure microwave plasma is another type of plasma medium often used for deposition of diamond films and different carbon nanostructures [31]. Normally, such devices use frequencies between a few GHz and several GHz with 2.45 GHz being the most common. Figure 1.8 shows the schematic of one such device. At these high frequencies power is transferred to the deposition chamber with the help of a waveguide and antenna. Similar to the case with any ac discharge, stray electrons in the device first get excited and help in creating the discharge. On penetration into the plasma, the microwave couples to a mode of the plasma and it is the absorption of this mode by the plasma particles that helps maintain the plasma. The power absorption depends on the pressure and normally at moderate pressures absorption occurs through electron–neutral collisions. It is well known that no wave can propagate through plasma unless its frequency is greater than the plasma frequency of that medium. The associated number density with the plasma frequency is called critical density and number density of the plasma cannot grow beyond this value. For microwave plasma at 2.45 GHz this critical density is  $\sim 7.3 \times 10^{16} \text{ m}^{-3}$ . Microwave discharges always have a lower plasma potential than the CCP discharges but their deposition rate is normally higher because of relatively higher operating pressure ( $\sim 15 \times 10^3 \text{ Pa}$  in some cases). This is a type of low pressure plasma where ion temperature can go as high as  $\sim 1200^\circ\text{C}$  because of high collision rate between electrons and gas atoms/molecules.

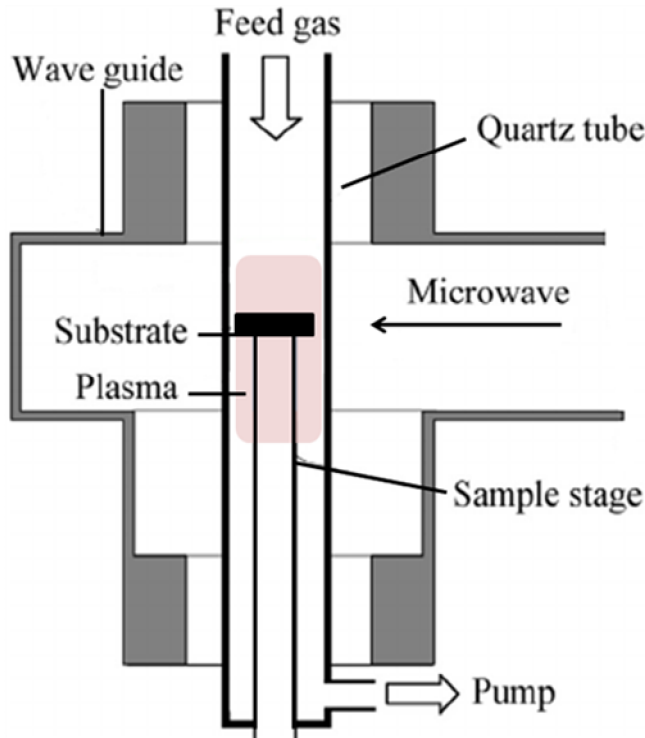


**Figure 1.8:** Schematic of a low pressure microwave discharge plasma system.

#### ***1.4.4 Microwave Electron-cyclotron resonance (ECR) plasma***

This discharge is initiated with the help of microwave radiation coupled with a pair of electromagnets. These discharges are created by setting electrons in resonance with the applied microwave field. The frequency of gyration of charged particles around the magnetic field is independent of velocity of particles. Magnetic field is normally produced by a pair of electromagnetic coils and the field varies in the axial direction. A linearly polarized microwave radiation is applied axially through a dielectric wall to the plasma. This field can be decomposed into two circularly polarized waves rotating in opposite directions, namely, left handed circularly polarized (LHP) and right handed circularly polarized (RHP).

The electric field of RHP wave rotates in the right handed direction around the magnetic field with a frequency  $\omega$  while the electrons also gyrate in same manner with a frequency  $\omega_c$ . When the magnetic field is such that  $\omega = \omega_c$ , the electrons continuously

gain energy along a circular path. In this condition of resonance maximum power is coupled to plasma. The LHP field on the other hand produces oscillating force whose time averaged value is zero and does not lead to any energy gain. However, the energy gained by electrons from the RHP wave is sufficient for the electrons to cause ionizing collisions. The ECR reactor essentially consists of two regions, the resonance region and the process region. The plasma flows along magnetic field lines from resonance region to the process region [29].

ECR plasma is another type of low pressure plasma discharge where operating pressure remains  $\sim 0.01$  Pa. At this low pressure the deposition rate is very slow but deposition is always very uniform and ‘atom by atom’ deposition is possible at this pressure. Figure 1.9 shows the schematic of one ECR plasma device with all the required accessories.

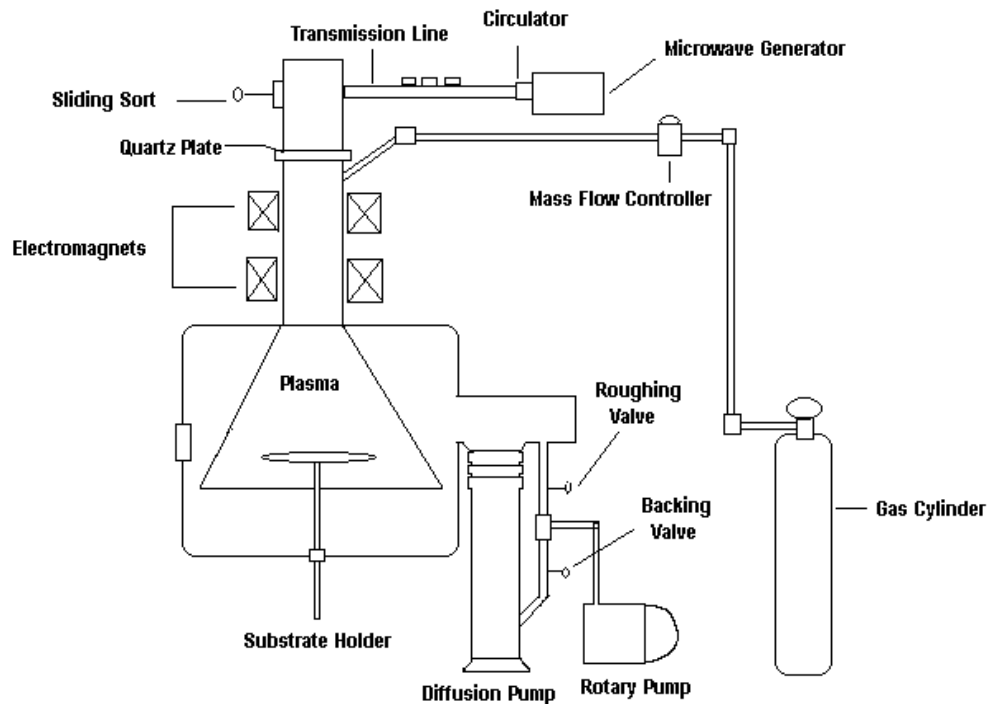


**Figure 1.9:** Schematic of a low pressure microwave ECR discharge plasma system.

Apart from the types of plasma discussed in the above subsections there are many other types of plasma discharges which have not been discussed. A major type of plasma is thermal plasma. Since thermal plasma has not been used during the course of the experiments described in this thesis, detailed description of thermal plasma has not included here. However, thermal plasmas like DC arc-discharge plasma, RF discharge plasma are also used in material processing like diamond deposition, deposition of carbon nanostructures and thick oxide coating depositions among other applications. All these depositions are being carried out at atmospheric pressure and deposition rate is two to three orders of magnitude higher compared to low pressure non-thermal plasmas. But, this high deposition rate comes with a lesser control over the deposition process. So, the deposited products often have high rate of porosity and contain a relatively higher degree of impurity as compared to their low pressure counterparts. Nevertheless, thermal plasma material processing is a very popular tool for depositing thick coatings particularly when porosities are not a major concern for the intended application.

There are also other types of non-thermal plasma devices which work at atmospheric pressure. These types of devices are relatively new and recently a lot of investigations are going on to study their usefulness in material processing. Dielectric barrier discharge (DBD) is the most popular among these types of devices. DBD is atmospheric pressure glow discharge which is being used for water purification and to generate hydrophobicity on fabric surfaces. There are also other 13.56 MHz (RF based) and 2.45 GHz (microwave based) devices which are being used for material processing. Their advantages lie in their high deposition rate and low deposition temperature.

## 1.5 Characterization techniques

Characterization is an integral task associated with any material processing activity. Without the help of characterization a researcher can never be sure about the usefulness and characteristics of synthesized material. There are different types of characterization techniques available. Some of them are complimentary to each other while some other may give rise to mutually exclusive information about the synthesized material. Table 1.1 represents different characterization techniques with their usefulness. From the table it is seen that there are three basic types of characterization techniques namely microscopy, spectroscopy and diffraction. Each of these provides unique information about the material under investigations. Their usefulness is noted in the table along with some examples for each of them.

**Table 1.1:** Different types of characterization techniques and their usefulness.

Type	Usefulness	Examples
Microscopy	Provides visual information where one can see the material directly or indirectly. It provides information on its structure, morphology, uniformity and dimension. Ultimate scale of the information depends on the resolution of the microscopic technique being used.	Optical microscopy.
		Scanning electron microscopy.
		Transmission electron microscopy.
		Atomic force microscopy.
		Scanning tunnelling microscopy.
Spectroscopy	Spectroscopy provides rich information about different chemical bonds, their	Raman spectroscopy.
		Infra-red spectroscopy.



	energies and elemental composition of the material which in turn helps to determine different characteristics of the material.	X-ray photoelectron spectroscopy.
		Electron energy loss spectroscopy.
		Energy dispersive X-ray spectroscopy.
		Optical emission spectroscopy.
Diffraction	This technique provides information about atomic or molecular structure of the system. It provides detailed information on different planes and other characteristics of lattice dynamics.	X-ray diffraction.
		Electron diffraction.

During the course of this thesis, we have used all three types of techniques mentioned above. Since nanostructures are all about visualizing the dimensions of the material synthesized, we have extensively used microscopy techniques. Both scanning electron microscopy (SEM) and transmission electron microscopy (TEM) were used to study the morphology and structures of the synthesized materials. These two techniques were primary techniques which helped us to identify and distinguish between different carbon nanostructures. Spectroscopic types of characterizations were also used quite extensively during this work. Raman spectroscopy has been the backbone in the research of carbon nanostructures. This technique gives elaborate information on the bonding, defect and purity of the deposited carbon nanostructures.

With careful analysis, one can also understand the structural difference of the synthesized nanostructures solely on the basis of Raman spectrum of the material. Apart from this, energy dispersive X-ray spectroscopy (EDX) has also been used to determine the elemental composition and their percentage in a particular nanostructure. Help was also taken from the in-situ EDX associated with a TEM for obtaining highly localized elemental information in some cases. Optical emission spectroscopy (OES) has been used during the deposition experiment to study the excited species of plasma and their effect on the deposition of a particular type of nanostructure. All these types of spectroscopic techniques have often been complimented with SEM/TEM studies to gather sounder knowledge about the synthesized nanostructures. Among the diffraction types of study X-ray diffraction (XRD) has been used during these studies and it has also been complimented with other studies before making a conclusive inference. The following subsections describe the principles, operational details and usefulness of all these characterization techniques used during the work described in this thesis.

#### ***1.5.1 Scanning electron microscopy (SEM)***

A scanning electron microscope (SEM) is an electron microscope that produces images of a sample by scanning it with a focused beam of electrons. SEM is a very important tool in nanotechnology. Normally as received solid samples can be taken for observation and it gives the information about the morphology and surface topography of the sample. Due to the very narrow electron beam, SEM micrographs have a large depth of field which results in a characteristic three-dimensional appearance of the sample under investigation which is very helpful for understanding the surface structure of a sample. A wide range of magnifications is possible with

SEM, from about 10 times (about equivalent to that of a powerful hand-lens) to more than 500,000 times, about 250 times the magnification limit of the best optical microscopes.

Figure 1.10 shows a schematic of the instrument useful in understanding its working principle [32]. Here electrons are generated by heating a thoriated tungsten filament,  $\text{LaB}_6$  or a field emission based source which acts as the cathode emitting electrons with energy  $\sim 20\text{-}40$  keV depending on the supplied current. The emitted electrons are then attracted towards the positively biased hollow anode through which the accelerated electron beam passes and reaches to the condenser lens system. Condenser lenses are electromagnetic lenses which focus the beam and then it reaches in the vicinity of the objective lens system. A pair of deflection or scanning coils is placed in between the objective lens which helps to scan the beam in X-Y direction. This coils helps in scanning the electron beam on the sample placed in the microscope. The electrons then interact with the sample, producing various signals that contain information about the sample's surface topography and composition. Interaction with the material leads to elastic and inelastic scattering of the electrons. Inelastic scattering leads to the emission of secondary electrons with energy  $\sim 50$  eV. This type of electrons are primarily detected for production of an image in the SEM. Elastic scattering leads to the emission of backscattered electrons which are also used for imaging if samples have elements with high atomic number difference. The interaction of electrons with the sample also leads to production of characteristic X-rays which are analyzed to obtain the elemental composition of the sample. SEM is a non destructive technique and it can achieve resolution better than 1 nanometer. Normally, SEM requires samples to be conducting in nature as electron scanning

otherwise becomes difficult and electron accumulation on the surface of the sample leads to ‘charging effect’. For this reason, normally insulating samples are coated with a very thin layer ( $\sim 5\text{nm}$ ) of conducting material like Au so that electrons can conduct through the top surface but can also penetrate the thin layer to give information about the specimen.

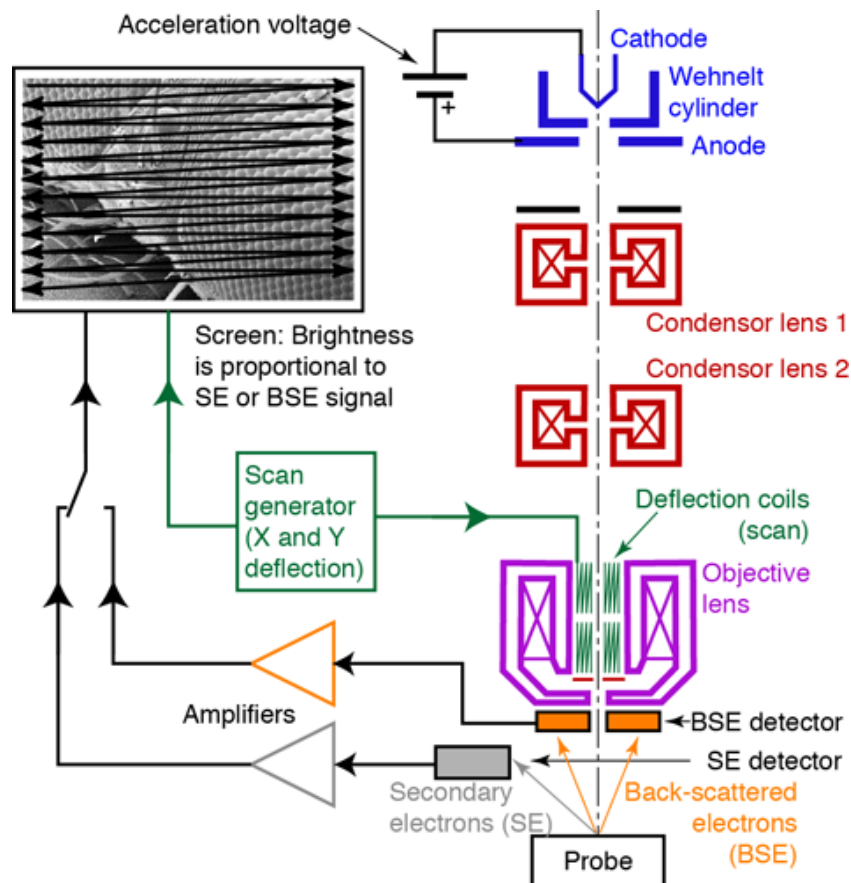


**Figure 1.10:** Schematic of a scanning electron microscope [32]

### 1.5.2 Transmission electron microscope (TEM)

Transmission electron microscope (TEM) is another type of electron microscope whose resolution is better than the SEM described above. As the name suggests, in TEM electrons must transmit through the sample to produce an image. For this very particular reason, the specimen to be observed under TEM must be prepared in a manner so that thickness of the sample remains in the order of few

microns only. In this instrument cathode produces electrons with energy 200-300 keV which is an order of magnitude higher than that of SEM. Since high energy is associated with further lowering the de-Broglie wavelength of electron it improves the resolution further compared to a SEM. Apart from doing microscopy, one can simply adjust current in the electromagnetic lenses to observe either a high-resolution microscopic image or a diffraction pattern. Diffraction created by electrons help to detect localized structure, grain boundaries and defects in them. Chemical analysis can also be done as characteristic X-rays get emitted from the sample. Figure 1.11 shows the schematic of a basic TEM device [33]. This device can be used for both imaging and diffraction. For imaging, emitted electrons from the electron gun are focused into a small, thin, coherent beam using the condenser lens. The beam then strikes the sample and part of it is transmitted depending upon sample thickness and electron transparency. This transmitted beam is focused by the objective lens forming an image on phosphor screen. This image is then passed down the column through the intermediate and a projector lens for magnification. The darker areas of the image represent areas of the sample from which fewer electrons could be transmitted compared to the lighter areas. The right hand side image of the Figure 1.11(b) depicts the principle of observing the diffraction pattern from the TEM sample. From the figure it is seen that, as the electrons pass through the sample, they are scattered by the electrostatic potential set up by the constituent elements in the specimen. After passing through the specimen they pass through the electromagnetic objective lens which focuses all the electrons scattered from one point of the specimen into one point in the image plane. Also, shown in the figure is a dotted line where the electrons scattered in the same direction by the sample are collected into a single point. This is

the back focal plane of the objective lens and is where the diffraction pattern is formed.

As stated above, sample preparation is an important aspect of the TEM analysis. For most electronic materials, a common sequence of preparation techniques is ultrasonic disk cutting, dimpling, and ion-milling. For samples like carbon nanostructures, they are first dispersed ultrasonically in acetone or alcohol and later one drop from that solution is taken on a carbon coated copper grid for viewing under microscope.

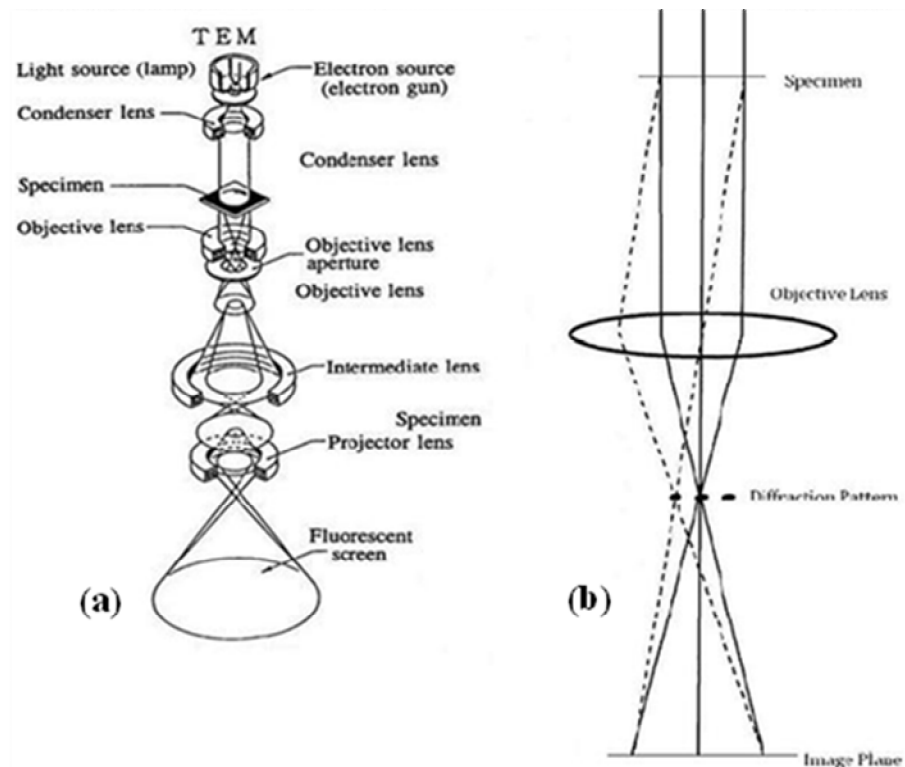


**Figure 1.11:** Schematic of a (a) transmission electron microscope, (b) principle of imaging and diffraction pattern. [33]

### 1.5.3 Raman spectroscopy

Raman spectroscopy is a spectroscopic technique used to observe vibrational, rotational, and other low-frequency modes in a system [34]. It depends on the inelastic

scattering of photon. This technique is commonly used in physics and chemistry to provide information on vibration bonds which act as fingerprint by which molecules can be identified.

In this technique, the sample which may be a gas, liquid or solid is irradiated with an intense beam of monochromatic radiation (usually from a laser) of wave number ( $\nu_0$ ) in the ultra violet, visible or infra-red regions of the electromagnetic spectrum. Most of the radiation is scattered without a change in wave number. This is the usual Rayleigh scattering. However, a small part of the scattered radiation ( $\sim 10^{-5}$  of the incident intensity) is scattered with the wave number  $\nu_0 \pm \nu_m$  where,  $\nu_m$  is characteristic wave number of molecular vibration that undergo excitation. The  $\nu_0 - \nu_m$  and  $\nu_0 + \nu_m$  scattered radiation components are known as Stokes and anti-Stokes lines, respectively. These phenomena occur as photons emitted by monochromatic laser interact with quanta of molecular vibrations (phonons) or excitons of the system being probed resulting in the energy of the laser photons being shifted up or down. The shift in energy gives information about the vibrational modes in the system. The selection rule for Raman scattering is based on molecular polarizabilities and induced dipoles which operate in infrared absorption bands and depends on dipole moment changes. The position and width of the Raman bands of materials are related to their vibration and structural properties.

The basic instrumentation of a conventional Raman spectrometer is shown in Figure 1.12. Monochromatic light from laser is incident on the sample and then gets reflected towards the detector. A notch filter placed in the path of reflected light cuts the Rayleigh component and the inelastic part is allowed to travel to a dispersive

element like grating. The dispersed light is then amplified and fed to a data acquisition system for processing.

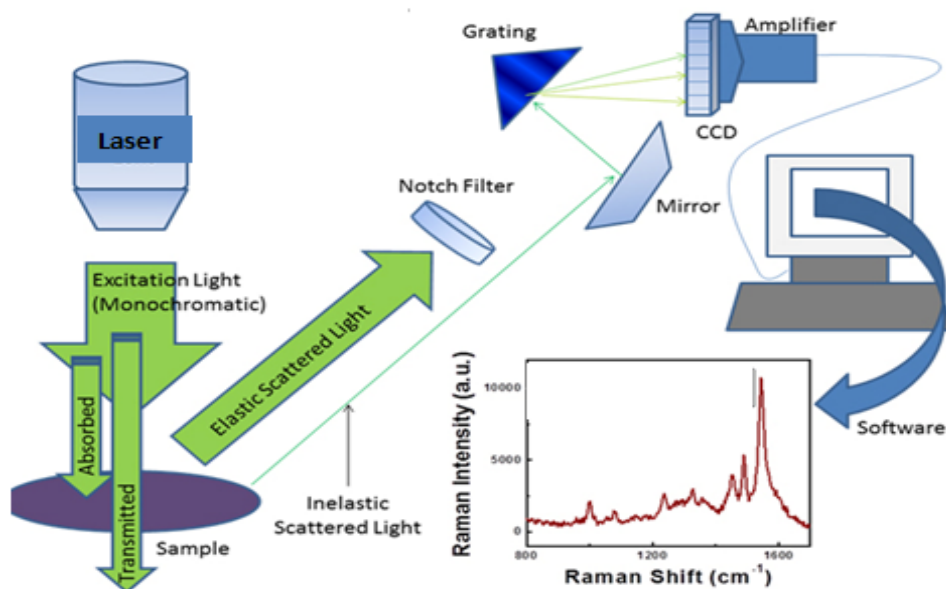


**Figure 1.12:** Schematic of a typical Raman spectroscopy system [35].

#### 1.5.4 Energy dispersive X-ray spectroscopy (EDS)

EDS is a spectroscopic technique which helps to identify the elemental composition of a material. This technique basically requires the identification of characteristic X-rays emitted by elements when they are subjected to an incident electron beam. EDS is normally an add-on associated with electron microscopy technique like SEM or TEM as both these techniques use high energetic electrons for image formation. The technique offers both qualitative & quantitative measurement of elemental composition present in the sample. Also, both local and global information from a sample can be obtained using this technique. The basic components of EDS are X-ray detector, pulse processor (to measure voltage corresponding to X-ray energies) and a computer. The size of voltage pulse is proportional to energy of X-rays. Elemental distribution maps or elemental line profiles can be obtained by EDS.



### 1.5.5 Optical emission spectroscopy (OES)

OES is a very popular spectroscopic tool in the realm of plasma diagnostics. This technique is a non-intrusive one as it does not affect plasma by any means. The technique involves collecting the visible portion of light from plasma by means of an optical fiber and its subsequent analysis. Normally, intensity vs. wavelength spectrum is recorded from which the identification of excited species is done [36]. Depending on the different conditions of the experiment, one can identify species which are helpful /detrimental to the process. Also, depending on the nature of the plasma, the recorded spectrum can also be used to calculate temperature and number density of the plasma. However, this process involves approximations and it normally provides rough estimates unless the plasma maintains LTE condition.

Figure 1.13 shows a schematic of the basic instrumentation required for this technique. The set-up shows that light collected from plasma by optical fiber passes through a lens system and then it is incident on a dispersive element like grating which disperses the visible spectrum into different wavelengths. This system with combination of mirror and grating forms the spectrometer which has a charge coupled device (CCD) placed at the opposite end. CCD converts light into electronic signal and then data passes to a PC where spectrum is recorded.

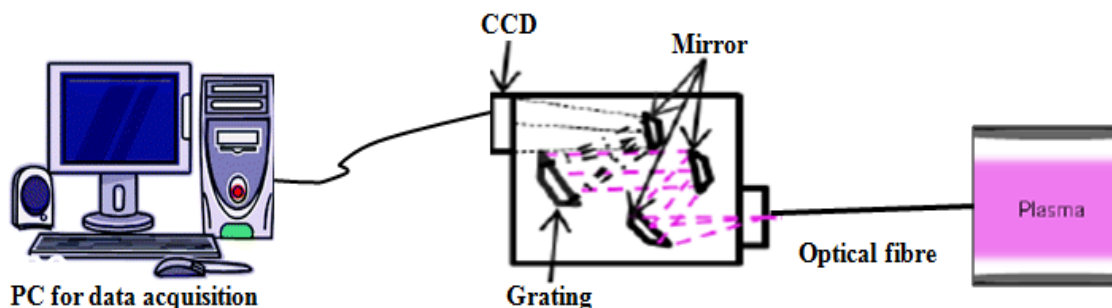


**Figure 1.13:** Schematic of a typical OES set-up.

### ***1.5.6 X-ray diffraction (XRD)***

XRD is the only diffraction based study which has been used in our work. This technique is fundamental in understanding the structure of a material under study. XRD principle is governed by Bragg's law which states that when X-rays of wavelength ( $\lambda$ ) is incident on the surface with the interplanar spacing ( $d$ ) of order of 1-100 Å , constructive interference of the diffracted rays gives rise to maximum intensity at certain angle ( $\theta$ ) which is called the Bragg's angle.

$$2d\sin\theta = n\lambda, \text{ Where, } n \text{ is integral multiple of } \lambda$$

Generally for study of bulk material,  $\theta$ - $2\theta$  (Bragg-Brentano) reflection geometry is used. Here the incidence angle is equal to the diffracted beam angle with respect to the sample surface. The device configuration enables high intensity diffracted beam from any particular set of crystalline planes to be focused on a slit in front of rotating detector. However, for greater angle of incidence, the X-rays can penetrate depths of few to several hundred micrometers inside the material. In case of thin film analysis, the beam penetration depth can be greater than the thickness of the film resulting in diffraction pattern dominated by the substrate peaks. By using grazing incidence configuration, the XRD measurements become more sensitive to the surface region of the film and the substrate contribution is minimized. In case of grazing angle X ray diffraction (GIXRD), a parallel monochromatic X-ray beam is incident on the sample at a fixed angle less than 2-3 degree and diffraction profile is recorded by detector scan only. By using this technique information regarding thickness, phase, changes in composition with depth can be obtained.

Figure 1.14 shows schematic of a basic experimental set-up for XRD. It shows that incident X-ray generated from a source hits the sample and then diffracted light is collected by the detector. The set-up showed here follows  $\theta$ - $2\theta$  geometry.

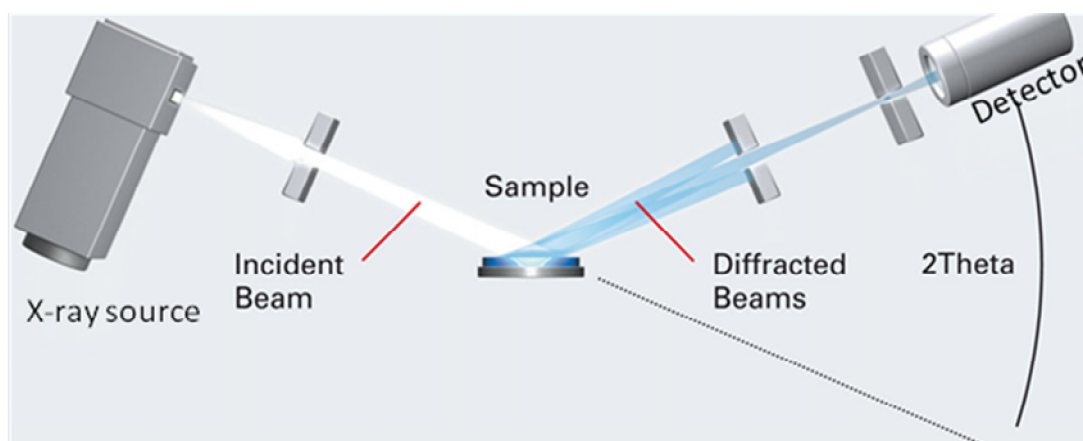


**Figure 1.14:** Schematic of a typical XRD set-up [37].

## 1.6 Scope of the thesis

Studies on synthesis, characterization and application of carbon nanostructures have been extensively reported in the literature for the past two decades. Before initiating this work we have studied many references on synthesis, characterization and applications of carbon nanostructures including some exhaustive reviews [9, 16, 38-45]. It is also seen that CNTs are nowadays commercially available for laboratory based research [46, 47]. But, in spite of all the progress achieved in the synthesis of carbon nanostructures, a gap remains to realise the full potential of carbon nanostructures for making practical devices. Taking the material from lab to commercially viable industrial scale remains a great challenge even to this day. The present scenario demands that efforts be made towards better understanding of the synthesis procedure of carbon nanostructures and finding newer, easier ways to make the potential applications commercially viable. Our literature survey also showed that CNT is the most researched nanomaterial in the family of carbon nanostructures. But,

many applications such as high field emission current density can also be obtained from other carbon nanostructures which at times are easier to synthesize. So, the need remains to look for other potential alternatives of CNTs from the same family for specific applications. It is also known that most of the carbon nanostructures have similar chemical bonding yet there are very few reports on the controlled co-deposition of two different nanostructures without mixing them up. These issues provided the motivation for the work done in this thesis.

Investigations of various process parameters of PECVD such as choice of substrates, the nature of precursors, operating pressure, substrate temperature etc. which affect the properties of the deposited films provided a major scope for this work. Effect of these parameters on the properties of deposited films enables selection of optimum experimental conditions under which film with desired properties can be obtained. Correlation between some of these deposition parameters with the properties of the deposited nanostructures is always important as they determine the physical and chemical properties of the deposited material. In the course of this thesis we have successfully identified some of these determining parameters.

In search of an alternative carbon nanostructure, we have synthesized CNWs by PECVD techniques and tried to understand their growth mechanism during the course of this work. We initially started our work with an ECR-CVD system for this work and later used MPECVD for the deposition of same nanostructure. It is known that ECR-CVD is a technique which works at low operating pressures, low temperature regime [48] and hence atom-by-atom deposition is possible in this case. This gives a precision in the deposition which is very important for nanomaterial growth via self-assembly. It is also noted that, microwave ECR plasma generation

process is an efficient process for large area uniform plasma generation [49]. Since, plasma generation mechanism is electrode-less in nature, so ECR plasma deposition results in very low contamination compared to other plasma processes. After analyzing the experimental results we have understood that CNW/GNW is a nanostructure which can be deposited by easier means compared CNTs and can also be used for many applications like field emission application and as supercapacitor.

Subsequently considering the various technological applications of CNTs, we have synthesized them by MPECVD technique and studied their field emission behavior. This technique produces CNTs in considerably less time compared to other PECVD techniques. We have found that field emission is one important property of CNTs which has been studied at length in the literature [9, 45, 50-52]. Researchers around the world have prepared different types of samples for improvement in this behavior so that a practical field emission device like cold cathode can be made. But, during our study we found that there is lot of room for improvement upon the knowledge on how the substrate preparation and attenuation of the incoming microwave beam may affect the field emission behavior of CNTs. We worked on these particular aspects and consciously chose Inconel as the substrate for this work. All syntheses were done without using any additional catalyst layer. Our choice of substrate is important for the development of a practical rugged cathode where intimate contact between the substrate and CNTs are important [45]. Our experiments resulted in newer findings about the effect of substrate pre-treatment and microwave attenuation on the field emission behavior of the deposited CNTs.

After working on two different types of carbon nanostructures we wanted to study the possibility of their co-deposition in a single experiment. This is an idea

which if implemented will save both process time and energy consumption. But, for implementing this idea one needs to have understanding of the controlling factors and key deposition parameters during the experiments. During literature survey we found that there are some reports which discuss about the co-deposition of two different kinds of carbon nanostructures on the same substrate [53-58] but we focused our interest in the domain of co-deposition of two different types of nanostructures in a single experiment where mixing of different nanostructures does not occur. We wanted to explore the possibility and understand the growth mechanism for this kind of co-deposition in PECVD experiments. We found only one available work by Yang et al. [59] which shows that co-deposition of sp<sup>3</sup> hybridized diamond and sp<sup>2</sup> hybridized CNT is possible in a single experiment. Our systematic experimental efforts resulted in important findings confirming that co-deposition is possible for both different (sp<sup>2</sup> and sp<sup>3</sup>) and similar (both sp<sup>2</sup>) type of carbon nanostructures. Our research showed that choice of substrate and its location are the most important parameters which controlled co-deposition experiments. In the thesis we have also discussed the role of plasma and found a correlation of the experimental results with a plasma parameter which can be taken as in-situ marker during the experiments.

#### **References:**

1. J. Gribbin, M. Gribbin, Richard Feynman: A Life in Science, Viking, 1997, P. 170.
2. Synthesis and characterization of block copolymer-mediated gold nanoparticles, Debes Ray, PhD Thesis HBNI, 2012.
3. S. Iijima, Nature 354 (1991) 56.
4. M.S. Dresselhaus, G. Dresselhaus, P. Avouris (Eds.), Carbon Nanotubes: Synthesis, Structure, Properties and Applications, Springer, Heidelberg, 2001.

5. T.T. Baby, R.B. Rakhi, N. Ravi, S. Ramaprabhu, J. Nanosci. Nanotech. 12 (2012) 6718.
6. R. Kar, S.G. Sarkar, C.B. Basak, A. Patsha, S. Dhara, C. Ghosh, D. Ramachandran, N. Chand, S.S. Chopade, D.S. Patil, Carbon, 94 (2015) 256.
7. R. Vidu, M. Rahman, M. Mahmoudi, M. Enachescu, T.D. Poteca, I. Opris, Front. Syst. Nanosci. 8 (2014) 91.
8. C.N.R. Rao, R. Voggu, A. Govindaraj, Nanoscale (2009) 96.
9. X. Lu, Z. Chen, Chemical Reviews. 105 (2005) 3643.
10. C. N. R. Rao, B. C. Satishkumar, A. Govindaraj, M. Nath, Chem.Phys.Chem. 2 (2001) 78.
11. P.A. Tesner, E.Y. Robinovich, E.F. Arefieva, Carbon 8 (1970) 435.
12. M. Meyyappan, Lance Delzeit, Alan Cassell, David Hash, Plasma Sources Sci. Technol. 12 (2003) 205.
13. Y. Wu, P. Qiao, T. Chong, Z. Shen, Adv. Matter. 14 (2002) 64.
14. M. Hiramatsu, K. Shiji, H. Amano, M. Hori; App. Phys. Lett. 84 (2004) 4708.
15. K. Kobayashi, M. Tanimura, H. Nakai, A. Yoshimura, H. Yoshimura, K. Kojima, M. Tachibana; J. Appl. Phys. 101 (2007) 094306.
16. E. Luais, M. Boujtita, A. Gohier, A. TAILLEUR, S. Casimirius, M. A. Djouadi, A. Granier, P. Y. Tessier; App. Phys. Lett. 95 (2009) 014104.
17. R. Kar, N.N. Patel, S.S. Chopade, S. Mukherjee, A.K. Das, D.S. Patil, J. Exp. Nanosci. 9 (2014) 575.
18. T. Machino, W. Takeuchi, H. Kano, M. Hiramatsu, M. Hori, Appl. Phys. Exp. 2 (2009) 025001.

19. O. Tanaike, N. Kitada, H. Yoshimura, H. Hatori, K. Kojima, M. Tachibana, *Solid State Ionics* 180 (2009) 381.
20. [https://www.chemie.uni-hamburg.de/pc/mews/research/nanotubes/neu\\_CNWs.jpg](https://www.chemie.uni-hamburg.de/pc/mews/research/nanotubes/neu_CNWs.jpg)
21. T. Itoh, S. Shimabukuro, S. Kawamura, and S. Nonomura: *Thin Solid Films* 501 (2006) 314.
22. M. Miyake, A. Ogino, M. Nagatsu, *Thin Solid Films* 515 (2007) 4258.
23. S.P. Hong, H. Yoshikawa, K. Wazumi, Y. Koga, *Diamond Relat. Mater.* 11 (2002) 877.
24. H. Zhou, J. Watanabe, M. Miyake, A. Ogino, M. Nagatsu, R. Zhan, *Diamond Relat. Mater.* 16 (2007) 675.
25. M. Chen, X.G. Jian, F.H. Sun, B. Hu, X.S. Liu, *J. Mater. Process. Technol.* 129 (2002) 81.
26. Y.C. Chen, D.C. Lee, C.Y. Hsiao, Y.F. Chung, H.C. Chen, J.P. Thomas, W.F. Pong, N.H. Tai, I.N. Lin, I.M. Chiu, *Biomaterials* 30 (2009) 3428.
27. F.F. Chen, 'Introduction to plasma physics and controlled fusion', 2<sup>nd</sup> edition, Volume-1: Plasma physics, Springer, 1974.
28. R. Kar, S.A. Barve, S.B. Singh, D.N. Barve, N. Chand, D.S. Patil, *Vacuum* 85 (2010) 151.
29. A. Bogaerts, E. Neyts, R. Gijbels, J van der Mullen, *Spectrochimica Acta Part B* 57 (2002) 609.
30. A. Ganguli, R. D. Tarey, *Current Science* 83 (2002) 279.
31. R.Kar, N.N. Patel, N.Chand, Shilpa R. K., R. O. Dusane, D.S. Patil, S.Sinha, *Carbon* 106 (2016) 233.
32. [http://www.rzuser.uni-heidelberg.de/~hb6/labor/rem/index\\_en.html](http://www.rzuser.uni-heidelberg.de/~hb6/labor/rem/index_en.html)



33. <https://www2.warwick.ac.uk/fac/sci/physics/current/postgraduate/regs/mpags/ex5/techniques/structural/tem/>
34. Gardiner, D.J. (1989). Practical Raman spectroscopy, Springer Verlag, ISBN 978-0-387-50254-0.
35. <https://www3.nd.edu/~kamatlab/images/Facilities/raman%20spectroscopy.jpg>
36. S.A. Linnik, A.V. Gaydaychuk, Vacuum 103 (2014) 28.
37. [http://www.d2phaser.com/images/d2-phaser/images/Bilder\\_1-1/Bilder\\_1-1-1.jpg](http://www.d2phaser.com/images/d2-phaser/images/Bilder_1-1/Bilder_1-1-1.jpg)
38. P. Jarillo-Herrero, J.A. Van Dam, L.P. Kouwenhoven, Nature 439 (2006) 953.
39. S. Fan, M.G. Chapline, N.R. Franklin, T.W. Tombler, A.M. Cassell, H. Dai Fan, Science 283 (1999) 512.
40. K.B.K. Teo, E. Minoux, L. Hudanski, F. Peauger, J.P. Schnell, L. Gangloff, P. Legagneux, D. Dieumegard, G.A.J. Amaratunga, W.I. Milne, Nature 437 (2005) 968.
41. Y.S. Woo, D. Y. Jeon, I.T. Han, Y.J. Park, H.J. Kim, J.E. Jung, J.M. Kim, J App. Phys. 94 (2003) 6789.
42. J. Ali, A. Kumar, S. Husain, S. Parveen, R. Choithrani, Md. Zulfequar, Harsh, M. Husain, J. Nanosci. 2014 (2014) 437895.
43. F. Hoshi, K. Tsugawa, A. Goto, T. Ishikura, S. Yamashita, M. Yumura, T. Hirao, K. Oura, Y. Koga, Diam. Rel. Mater. 10 (2001) 254.
44. C.M. Hsu, C.H. Lin, H.L. Chang, C. T. Kuo, Thin Solid Films 420 –421 (2002) 225.
45. S. Talapatra, S. Kar, S.K. Pal, R. Vajtai, L. Ci, P. Victor, M. M. Shaijumon, S. Kaur, O. Nalamasu, P. M. Ajayan, Nature Nanotech. 1 (2006) 112.
46. <http://www.nanoamor.com/home>
47. <http://www.timesnano.com/>

48. J. Asmussen, J. Vac. Sci. technol. A7 (1989) 883.
49. S. A. Barve, N. S. Nandurkar, N. Chand, S. B. Singh, N. Mithal, Jagannath, B. M. Bhanage, D. S. Patil, L. M. Gantayet, J. Phys.: Conf. Ser. 114 (2008) 012045.
50. W. Yi, Q. Yang, Diam. Rel. Mat. 19 (2010) 923.
51. M. Hirakawa, S. Sonoda, C. Tanaka, H. Murakami, H. Yamakawa App. Surf. Sci. 169-170 (2001) 662.
52. S. Sridhar, L. Ge, C. S. Tiwary, A. C. Hart, S. Ozden, K. Kalaga S. Lei, S.V. Sridhar, R. K. Sinha, H. Harsh, K. Kordas, P. M. Ajayan, R. Vajtai, ACS App. Mater. Interfaces 6, (2014) 1986.
53. M.L. Terranova, S. Orlanducci, A. Fiori, E. Tamburri, V. Sessa, Chem. Mater. 17 (2005) 3214.
54. A.J.S. Fernandes, M. Pinto, M.A. Neto, F.J. Oliveira, R.F. Silva, F.M. Costa, Diam. Rel. Mater. 18 (2009) 160.
55. N. Shankar, N.G. Glumac, M. Yu, S.P. Vanka, Diam. Relat. Mater. 17 (2008) 79.
56. D. Takagi, Y. Kobayashi, Y. Homma, J. Am. Chem. Soc. 131 (2009) 6922.
57. Y.Q. Hou, D.M. Zhuang, G. Zhang, M.S. Wu, J.J. Liu, Appl. Surf. Sci. 185 (2002) 303.
58. C.R. Kumaran, M. Chandran, M.K. Surendra, S.S. Bhattacharya, M.S.R. Rao, J. Mater. Sci. 50 (2015) 144.
59. Q. Yang, Y. Tang, S.L. Yang, Y.S. Li, A. Hirose, Carbon 46 (2008) 589.

## **Chapter 2**

### **Description of Experimental Systems**

This chapter describes the experimental procedures adopted during the deposition of carbon nanostructures which are being reported in this thesis. As mentioned in the last chapter CNWs, CNTs and NCDs were deposited by PECVD method during the course of this work. While ECR-PECVD was used for the synthesis of CNWs, MPECVD was used for the production of all the other nanostructures. This chapter will discuss these two different PECVD systems in details with all hardware and their functions. Apart from that, this chapter will also discuss about our choice of substrates for deposition of different carbon nanostructures and their preparation methods prior to deposition.

#### **2.1 ECR-PECVD system**

The schematic of the microwave ECR-PECVD system is shown in Figure 2.1 [1]. For microwave generation and transmission, the hardware consists of various components. A magnetron based microwave generator continuously generates 2.45 GHz microwave signal and a rectangular  $TE_{10}$  waveguide is used to transfer microwave radiation to the deposition system. A three-port circulator with water cooled dummy load takes away the reflected power and a cross coupler is attached with microwave power meters to measure forward and reflected powers of the generated microwave. The impedance matching between the dynamic plasma load and the microwave system is done with the help of three stub tuners and a sliding short attached to the waveguide. In the present system, a mode converter ( $TE_{10}$  to  $TM_{01}$ ) is additionally added to make the electric field present in the waveguide radially symmetric. Microwaves are launched in the ECR plasma source chamber through a

quartz window that also serves as vacuum isolation between the microwave transmission line and ECR plasma chamber [2, 3]. The ECR plasma generation chamber (150 mm diameter and 550 mm height) is surrounded by two water cooled electromagnet coils (separately powered by DC current regulated power supplies) capable of generating a desired magnetic field profile required for the ECR condition. The axial magnetic field profile in the chamber is generated by passing a current of 130 A (top coil) and 170 A (bottom coil) and the generated magnetic field profile is shown in Figure 2.2 which was measured by Singh et al. [2]. After setting up the magnetic field profile, required gases (mixture of CH<sub>4</sub> and H<sub>2</sub> in this case) are fed into the source chamber from the inlet located near the quartz isolation window. Next, microwave power is supplied into the chamber for plasma generation. It is launched axially from the high-field region, where  $\omega_{ce}$  (electron plasma frequency) <  $\omega$  (frequency of incident radiation), these waves in the plasma propagate axially along the magnetic field before getting absorbed at the resonance layer where  $\omega_{ce} \sim \omega$ . It helps in obtaining dense and stable plasma [4]. Three stub tuners and sliding short, if required, are adjusted to minimize the reflected power to get a stable plasma generation. After generation this plasma expands into a processing chamber (400 mm diameter x 500 mm height) under the influence of the magnetic field gradient.

Stable plasma generation is necessary for any plasma assisted CVD process. Initial experiments to generate stable microwave ECR plasma indicated that stability of the generated plasma is better when operating pressure is in the range of  $10^{-4}$  -  $10^{-5}$  mbar hence all depositions were done in this specified pressure range.

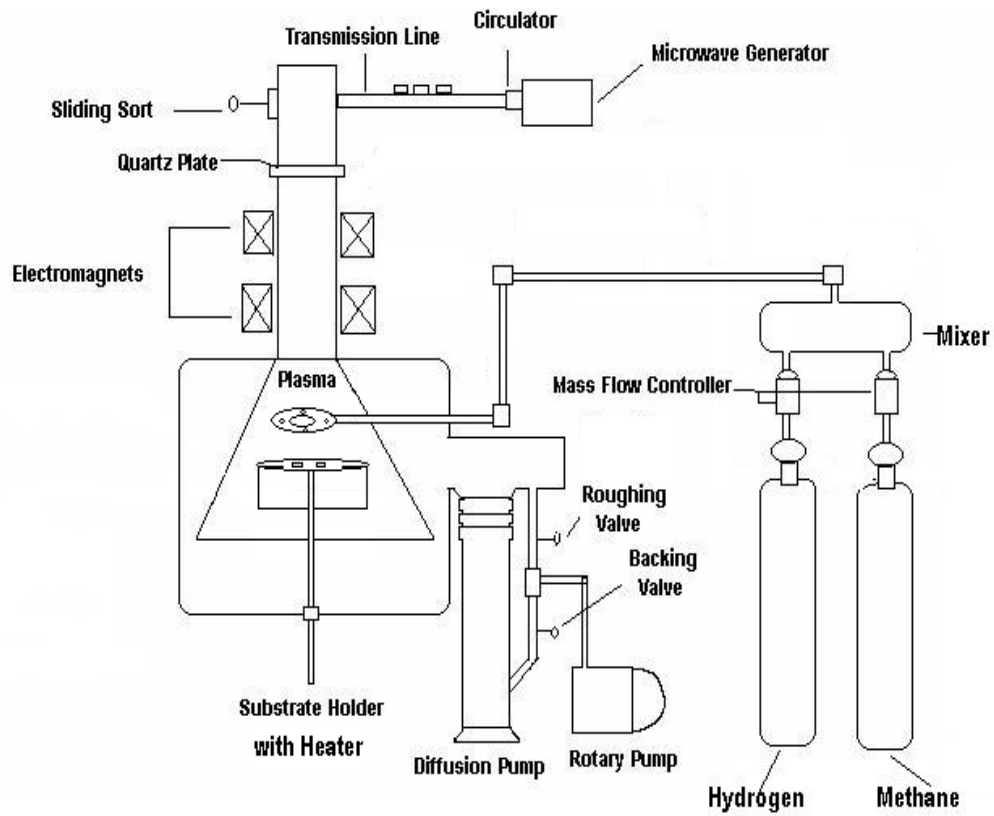


**Figure 2.1:** Schematic of the ECR-PECVD facility [1].

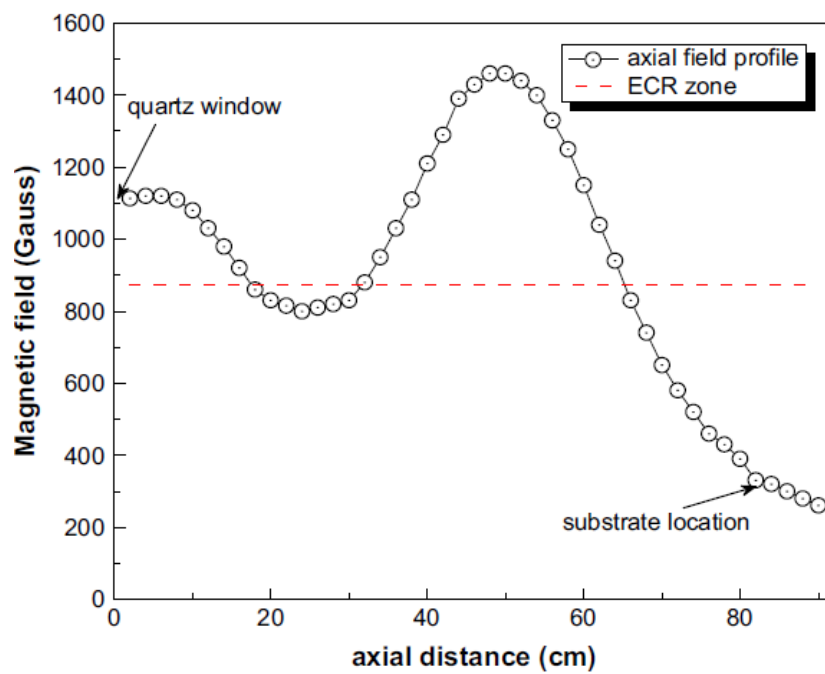


**Figure 2.2:** Variation of magnetic field profile with axial distance. [2].

## 2.2 MPECVD system

Schematic of the MPECVD system which was used in the growth of CNTs is shown in Figure 2.3 [5]. The hardware part of the system is similar to ECR-PECVD setup (except the presence of electromagnets in the ECR system) as both system uses microwave for plasma generation. This system consists of a 2.45 GHz, 2KW water-cooled magnetron for microwave generation, rectangular waveguide for propagation of TE<sub>10</sub> mode, a three port circulator and water cooled dummy load, cross coupler, power indicating meters, three stub tuners, a sliding short and a microwave mode converter for TE<sub>10</sub> to TM<sub>01</sub> mode conversion. During deposition, maximum power transfer to the plasma load in the process chamber is achieved with the help of three stub tuners and sliding short. Microwave hardware is isolated from vacuum of the process chamber by a quartz isolation window Purpose served by all the components mentioned above are similar to what has been discussed in the preceding section.

Substrates for deposition were placed on a substrate holder which can be heated independently to a temperature of 1000<sup>0</sup>C with the help of a Molybdenum heater. However, for conducting the experiments mentioned here, this heater was not required as plasma itself provided temperature ~ 800-1200<sup>0</sup>C. The chamber was initially evacuated to a pressure of ~ 5 x 10<sup>-2</sup> Torr with the help of a rotary pump connected to the chamber. The precursor gases were then fed into the chamber through mass flow controllers and these gases were mixed together in a gas mixer before reaching the chamber (as shown in the schematic). The gas load took the chamber to the desired operating pressure during experiments.

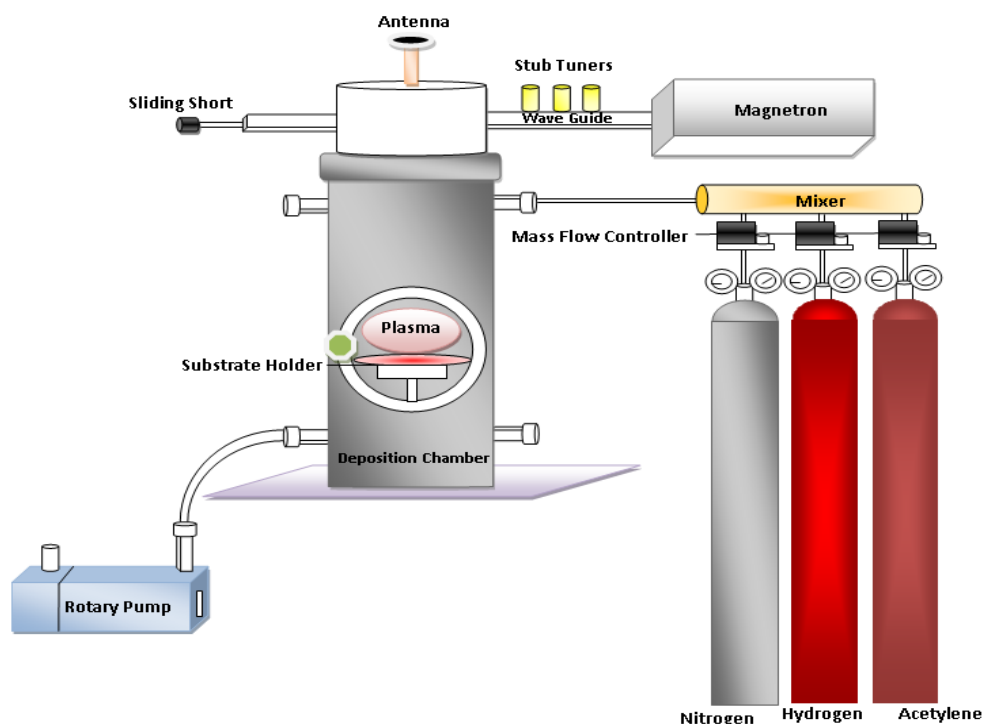


**Figure 2.3:** Schematic diagram of the MPECVD set up used for the deposition of CNTs [5].

### 2.3 Choice of substrates and substrate preparation methods

Different substrates were chosen for deposition of CNTs, CNWs/GNWs and NCDs during the course of this thesis. GNWs/CNWs were always deposited on Si substrates while Inconel was chosen in all the experiments for deposition of CNTs. Si is a common choice as substrate for deposition of thin films and nanostructures because of its easy availability, economical methods of crystallization, relative strong mechanical property and possibility of easy doping with suitable materials among others.

As stated in the previous chapter, Inconel was chosen as the substrate for deposition of CNTs for the development of a practical and rugged cathode where intimate contact between the substrate and CNTs are important [6]. Inconel is an

alloy and different varieties of this alloy are commercially available with widely varying compositions but all have predominantly Ni with Cr as the 2<sup>nd</sup> most abundant element. We have used Inconel 600 for our work. It has 72% Ni, 14-17% Cr and 6-10 % Fe. Balance amount is constituted by Si, C and S [7]. Inconel was chosen as it is a mixture of 3-D transition elements like Ni, Cr, Fe which are known to work as catalysts for deposition of CNTs. Our idea was to prepare in-situ catalyst particles during experiment from the substrate itself on which CNTs would grow after super saturation.

### ***2.3.1 Preparation of Si substrate for CNW/GNW deposition by ECR-CVD***

Si substrates used for deposition were initially cleaned by Radio Corporation of America (RCA) procedures [8]. The RCA clean is a standard set of wafer cleaning steps and it was performed before loading the Si substrates in the chambers. We have done three step RCA process. In the first step, substrates were cleaned for removing organic contaminants in a solution with mixture of 5 (deionized H<sub>2</sub>O):1 (NH<sub>4</sub>OH):1 (H<sub>2</sub>O<sub>2</sub>) at 80<sup>0</sup>C for 10 minutes. Next process was the removal of ionic contamination which was done by heating the substrates at 80<sup>0</sup>C for 10 minutes in a solution mixture of 6 (deionized H<sub>2</sub>O):1 (HCl):1 (H<sub>2</sub>O<sub>2</sub>). After that these substrates were dried under infrared lamp. Some of the Si wafers were coated with 15 nm Ni layer as catalyst by DC magnetron sputtering for deposition of CNWs. There were two types of substrates prepared for Ni coating; one type was heated in air at 650<sup>0</sup> C for 2 hours for formation of a native oxide layer on it prior to Ni deposition while other was left untreated before Ni coating.



### ***2.3.2 Preparation of Si substrate for CNW/ GNW and NCD deposition by MPECVD***

For these particular set of experiments, Si substrates were prepared in different manner altogether. RCA cleaning was not done for these substrates. For these experiments, Si wafers were first cut into rectangular pieces by a diamond cutter; next they were cleaned ultrasonically in methanol for 10 minutes and dried under infrared lamp. For deposition of GNWs these Si substrates were directly loaded into the MPECVD chamber on top of Inconel 600 substrates. For deposition of NCD by MPECVD, Si substrates were prepared by first scratching them with a 320 grade emery paper. After scratching marks become visible under optical microscope, Si substrates were ultrasonicated for 10 minutes in a solution of methanol mixed with 25  $\mu\text{m}$  diamond powder. This process was done as it is often mentioned in literatures that random scratches filled with diamond particles is the primary requirement to initiate diamond nucleation [9, 10]. After that substrates were loaded in the MPECVD chamber and mounted on the top of Inconel 600 substrates. The Si sample mounted on the top of Inconel substrate acted as an attenuator for the incident microwave radiation and also helped in co-deposition process. More details about this experimental scheme will be discussed in chapters 4 & 5.

### ***2.3.3 Preparation of Inconel 600 substrate for CNT deposition by MPECVD***

Inconel substrates chosen for the deposition of CNTs were button type. They had a 12.5 mm circular cross-section with a thickness of 3 mm. In few experiments, larger Inconel substrates were also chosen. Substrates of larger sizes affected uniformity of plasma and subsequently affected the deposition itself. The experimental results with larger substrates will be discussed in detail in chapter 5. Two different methods were employed to prepare Inconel substrates deposition

experiments. In the first method, as received substrates were cleaned ultrasonically in methanol for 10 minutes and loaded into the process chamber. In the second method, prior to ultrasonic cleaning in methanol, Inconel 600 substrates were heated in air to 1100°C for 2 hours. These heated Inconel substrates were then ultrasonicated in methanol for 10 minutes and used for the growth of CNTs. Oxidation of the Inconel substrates were deliberate and they improved the surface density of the deposited CNTs. The reason for such enhancement will be discussed in detail in chapter 4 of this thesis.

### **References:**

1. R. Kar , N.N. Patel , S.S. Chopade , S. Mukherjee , A.K. Das, D.S. Patil, J. Exp. Nanosci. 9 (2014) 575.
2. S.B. Singh, N. Chand, D.S. Patil, Vacuum, 83 (2009) 372.
3. R. Kar, S.A. Barve, S.B. Singh, D.N. Barve, N. Chand, D.S. Patil, Vacuum 85 (2010) 151.
4. A.O. Popov J. Vac. Sci. Tech. A 9 (1991) 711.
5. R. Kar, S.G. Sarkar, C.B. Basak, A. Patsha, S. Dhara, C. Ghosh, D. Ramachandran, N. Chand, S.S. Chopade, D.S. Patil, Carbon, 94 (2015) 256.
6. S. Talapatra, S. Kar, S.K. Pal, R. Vajtai, L. Ci, P. Victor, M. M. Shaijumon, S. Kaur, O. Nalamasu, P. M. Ajayan, Nature Nanotech. 1 (2006) 112.
7. <https://en.wikipedia.org/wiki/Inconel>
8. W. Kern 137 (1990) 1887.
9. M. Vojs, M. Varga, O. Babchenko, T. Ižák, M. Mikolášek, M. Marton et al. App. Sur. Sci. 312 (2014) 226.
10. T. Chein, J. Wei, Y. Tzeng, Diamond Relat. Mater. 8 (1999) 1686.

## **Chapter 3**

### **Deposition and Characterization of Carbon Nanowalls synthesized by ECR-CVD Method**

#### **3.1 Introduction**

The investigations reported here describe the synthesis of Carbon nanowalls (CNW) by ECR plasma assisted CVD process without application of any external bias to the substrate during growth. CNWs were grown on Silicon (Si) substrates by two different plasma compositions of  $\text{H}_2/\text{CH}_4$  and  $\text{N}_2/\text{CH}_4$  plasma. In both the cases the substrates were heated to  $650^0\text{ C}$  with the help of an additional heater during deposition. Ni was chosen as the catalyst for synthesis of CNWs. Formation of CNWs on the Si substrates in both the cases were confirmed by scanning electron microscopy (SEM), transmission electron microscopy (TEM), energy dispersive electron spectroscopy (EDS) and Raman Spectroscopy. A qualitative model for growth mechanism of CNWs in this case has also been discussed which highlights the possible involvement of localized surface plasmons during the deposition.

It is known that ECR plasma generation is an efficient process for generation of large area uniform plasma [1] and this process works at low operating pressures, low temperature regime [2] which makes atom-by-atom deposition possible. This leads to a precision in the deposition which is very important for nanomaterial growth via self-assembly. Also, plasma generation mechanism in this case is of electrode-less nature and it leads to very low contamination compared to other plasma processes. In spite of having these advantages there are very few reports available on the successful deposition of Carbon nanowall by ECR plasma CVD [3, 4, 5]. The main difference

between synthesis routes reported by others and the one presented here is that no external substrate bias was applied during growth process. Generally an electrical substrate bias (-50 to -200 V) is used during the growth of Carbon nanostructures in ECR plasma as it is expected to be essential for enhancement of ion bombardment energy to increase attraction for more positive species [6]. But our investigations showed that electrical bias is not necessary for the growth of CNW.

### 3.2 Experimental Details

Figure 3.1 shows a schematic of the ECR plasma processing facility used in the synthesis of CNWs. Detailed description of this facility is provided in chapter 2, section 2.1. In short, magnetron generates 2.45 GHz microwave which then passes through a three port circulator connected to water cooled dummy load before reaching the chamber through a quartz isolation window. Power matching is done through three stub-tuners and one sliding short and ECR condition is maintained by two water cooled electromagnets by setting up a specific magnetic field among them [7]. A substrate heater is inserted from bottom on which we placed the substrates for deposition.

N-type Silicon (Si) was chosen as substrate for the deposition of CNWs. Three different kinds of substrates were prepared for the experiment. One was bare Si wafer without any catalyst coating or treatment. Other two were coated with 15 nm Ni layer by DC magnetron sputtering. Among these two substrates one was heated in air at 650<sup>0</sup> C for 2 hours for formation of a native oxide layer on it prior to Ni deposition. It is well known that a native Oxide layer on Si prior to Ni deposition helps in formation of a diffusion-barrier layer of SiO<sub>2</sub> preventing Silicide formation which is a common problem for transition metal layer deposition on Si [6, 8]. However, there are also

reports of Carbon nanostructure growth without any diffusion barrier layer and sometimes even in absence of any catalyst layer at all [9]. The scheme chosen by us was aimed at exploring the feasibility of growth of Carbon nanostructures on differently conditioned substrate when used in the same ECR-CVD deposition set-up.

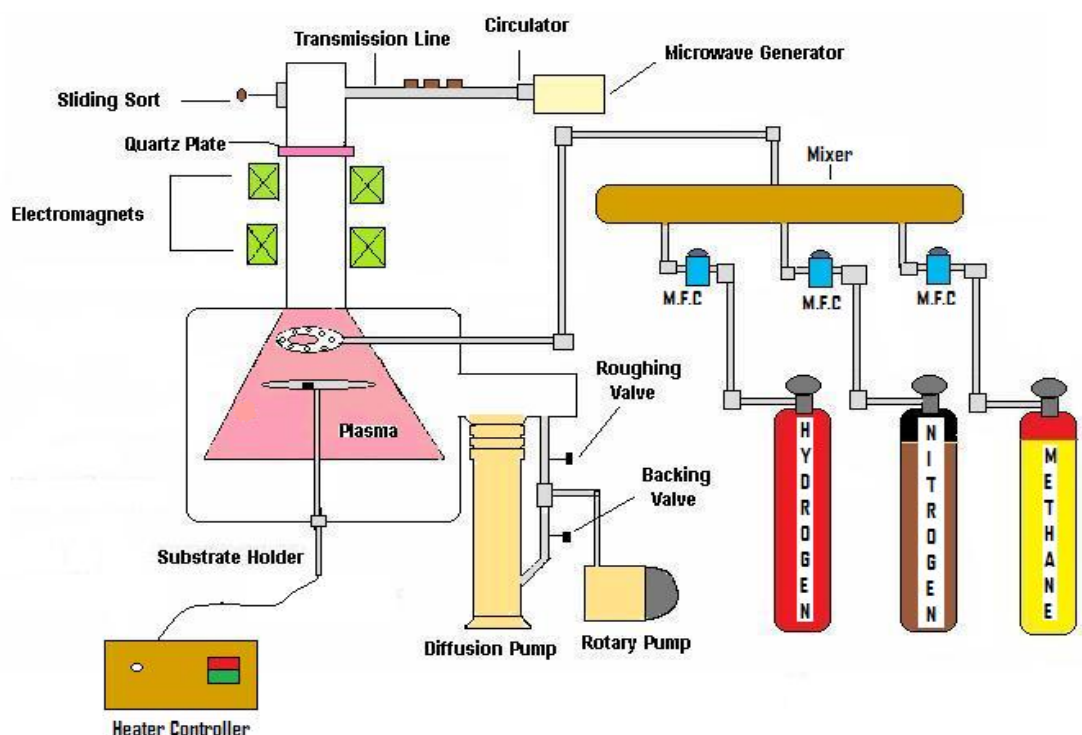


**Figure 3.1:** Schematic of the ECR-PECVD facility used for deposition of CNWs.

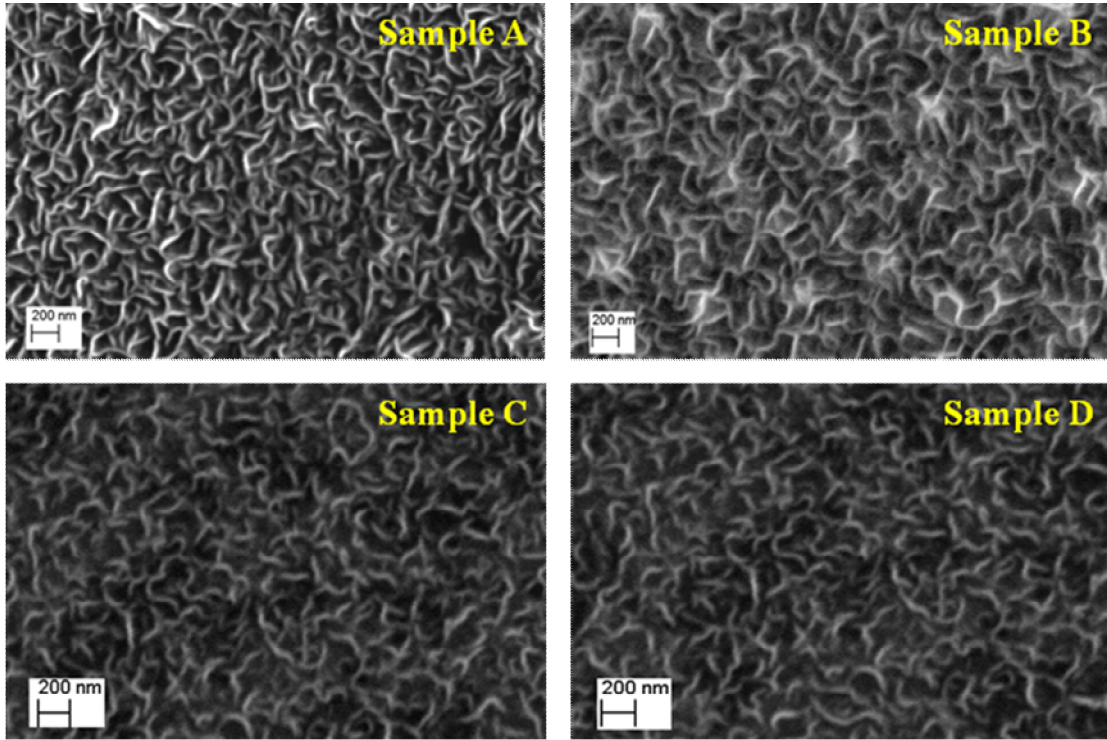
Prior to the experiments, the ECR-PECVD chamber was evacuated to a base pressure of  $\sim 2 \times 10^{-5}$  mbar in each case. Next, 20 SCCM  $H_2$  plasma was generated for pre-treatment of deposited Ni layer. It is assumed that  $H_2$  plasma treatment helps in the formation of Ni nano particles which then acts as the catalyst during deposition of CNWs. Two different sets of experiments were conducted after pre-treatment. In the 1<sup>st</sup> set, after 20 minutes the plasma composition in the chamber was changed by reducing  $H_2$  flow to 2 SCCM and 18 SCCM of  $CH_4$  was introduced in the chamber for further 20 minutes for the growth of CNWs while in the 2<sup>nd</sup> set,  $H_2$  was completely

replaced by  $N_2$  with a flow rate of 2 SCCM. Substrate temperature and microwave power were kept fixed at  $650^0\text{ C}$  and 780 watt respectively in both the experiments. After deposition it was found that thick black film deposited on all substrates. The films deposited on the Si substrates with Ni catalyst layer were characterized for further analysis. However, the film deposited on the bare (untreated) Si substrate peeled off within a week before any characterization could be done. These four samples henceforth would be named as sample A ( $H_2/CH_4$  plasma, with substrate surface heated), sample B ( $H_2/CH_4$  plasma, with substrate surface unheated), sample C ( $N_2/CH_4$  plasma, with substrate surface heated) and sample D ( $N_2/CH_4$  plasma, with substrate surface unheated) throughout this chapter.

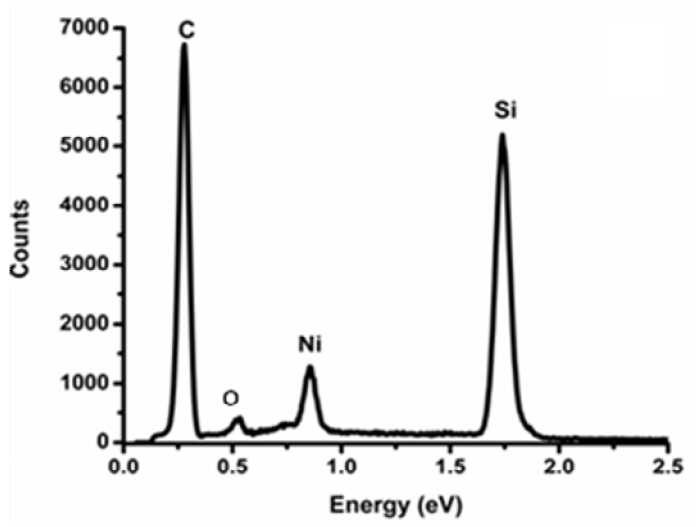
### 3.3 Results

Figure 3.2 shows the SEM images of the deposited CNWs on Si samples. The images were taken using a Carl-Zeiss EVO 40 SEM device. From the figures it is seen that nanostructures have been deposited in all four cases so it can be safely said that the problem of Silicide formation did not occur in the unheated Si substrate and in all the cases growth of dense CNWs are observed.

Figure 3.3 shows a typical EDS spectrum taken for CNWs sample with the help of a Bruker Quanta EDX system with a 20 KeV electron beam. The spectrum as expected shows the two most intense peaks as C and Si. The former in this case is the deposited element and the latter is the substrate element itself. Apart from these Ni which was applied as the catalyst also shows its presence in the spectrum. O is the least intense peak present in the spectrum. Combining SEM and EDS results one can conclude that CNWs have been deposited on the Si substrate during the deposition process.



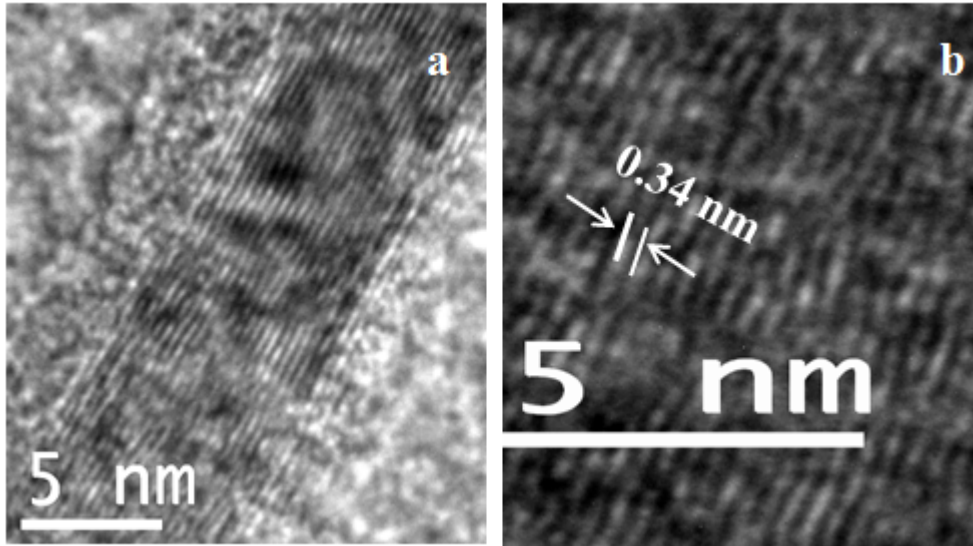
**Figure 3.2:** SEM image of the deposited four samples of CNWs.



**Figure 3.3:** A typical EDS spectrum of the deposited CNWs.

Figure 3.4 shows the typical high-resolution TEM (HRTEM) images of CNWs obtained in these experiments. Figure 3.4(a) shows that the deposited CNWs as layers of continuous parallel graphene sheets which is expected in this case. The measurement of inter-layer spacing between two different graphene sheets has been

made in Figure 3.4(b) with the help of ImageJ software. The value turns out to be  $\sim 0.34$  nm which is the known value for inter-layer spacing between two graphene sheets.



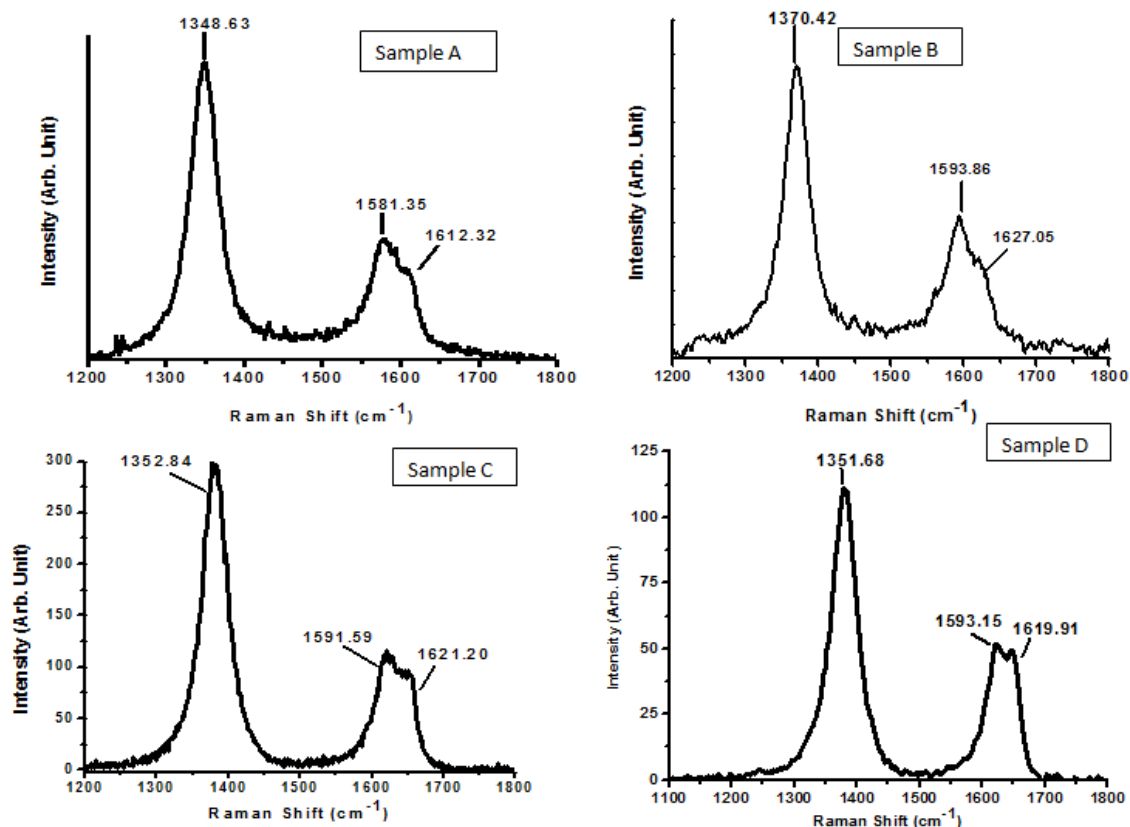
**Figure 3.4:** (a) Typical HRTEM image of deposited CNWs, (b) measurement of inter-layer spacing between two graphene sheets.

Figure 3.5 shows the obtained Raman spectra of the grown CNWs on heated and unheated substrates using a 488 nm Ar-ion laser. Each obtained band was analyzed by fitting it with a Lorentzian profile. As shown in Figure 3.5 there are three peaks in each figure. The peak at  $1350\text{-}1370\text{ cm}^{-1}$  is the D band peak which is a second order Raman mode corresponding to the disorder induced phonon mode. This band originates from the disorder induced mode in graphite of the same name [10]. This band usually arises due to the presence of in-plane substitutional heteroatoms, grain boundaries, vacancies and other defects. This band primarily indicates defects and disappears for highly ordered pyrolytic graphite (HOPG). It signifies the disorder in the graphitic structure. The peak around  $1580\text{-}1590\text{ cm}^{-1}$  is called G-band peak and it is the only first order Raman band seen in the case of CNWs. It originates at the 1<sup>st</sup>



Brillouin zone centre of the of graphene unit cell. This band signifies the formation of graphitic structure [11]. It is observed that another peak accompanying G band peak is visible as the shoulder peak around 1610-1620  $\text{cm}^{-1}$ . It is called D' peak and it is another second order peak generated due to the presence of defects in the graphitic structure. This peak is observed in some disordered graphitic carbon structures [12] including graphene [11]. D and D' are dispersive in nature and their position in the Raman spectra changes with incident laser wavelength [13, 14]. The dispersive behavior of D and D' bands can be understood in terms of double resonant Raman scattering [14].

The integrated intensity ratio of D and G band ( $I_D/I_G$ ) is a measure of defect in the graphitic structure. Larger ratio indicates higher degree of defect in the graphitic structure [15]. The values of this parameter for the samples A, B, C and D are 1.84, 1.82, 2.95 and 2.83 respectively. From the values it can be said that, the defect is more for the samples C & D compared to samples A & B. So, use of  $\text{N}_2$  in the plasma causes more defects in the deposited CNWs. Another important observation remains that whether the substrate is heated or not, there is no favourable growth of CNWs in terms of defects on the heated substrate.



**Figure 3.5:** Raman spectrum of the deposited four samples of CNWs.

### 3.4 Discussion

SEM, EDS, HRTEM and Raman spectra clearly show the formation of CNWs in ECR plasma. We have followed catalytic PECVD route for this work by depositing 15 nm thick Ni layer on the Si substrates to act as catalyst. This layer got transformed into Ni nanoparticles under the H<sub>2</sub> plasma treatment. Figure 3.6(a) shows a typical SEM image of Ni nanoparticles after plasma treatment of Ni thin film. Figure 3.6(b) shows the histogram of these nanoparticles. From the plot it is seen that these particles have dimensions ranging from 20-100 nm though ~ 80% of these nanoparticles falls within 30-60 nm. A closer inspection of the image 3.6(a) also reveals that all the particles seen here are not exactly circular in shape and they can be referred as ‘nano-islands’ in general after some previous researchers [15, 16]. Figure 3.6(c) shows

signature of few such nano-islands (marked by yellow circles) even after the formation of CNWs on the substrate. From these two images it can be concluded that, unlike some other reports [9] the CNW deposition in our case depends on catalytic activity of Ni during deposition.

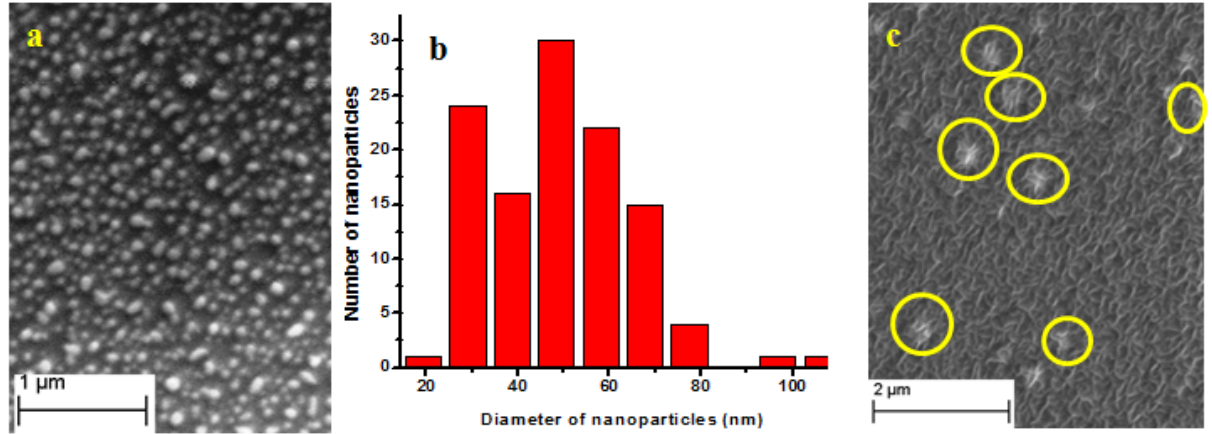


**Figure 3.6:** (a) Typical SEM image showing formation of Ni nano-islands after plasma pre-treatment of Ni thin film, (b) histogram plot of dimensions of Ni nano-islands, (c) Sporadic presence of nano-islands marked by yellow circles in SEM image of CNWs.

For finding out the possible growth mechanism of CNWs in a low pressure plasma process like ECR CVD, we need to explore all the possible options available and compare them with the experimental findings. But, there are actually very few reports which tried to understand the growth mechanism of CNWs [15, 16]. After discovering CNWs, Wu et al. pointed out that growth mechanism behind the formation of CNWs is the emergence of strong lateral fields due to the non-uniform charging of Ni catalyst islands [15]. They could deposit CNWs on sapphire substrates by MPECVD process and also applied an external DC bias. They pointed that they could only deposit CNWs on dielectric substrates with conducting catalyst nano-islands present on them. So, non-uniform charge accumulation on these metallic nano-

islands built a lateral field which helped in formation of CNWs. It is earlier seen that growth of any crystalline Carbon nanostructure in ECR-CVD normally requires an external electrical bias [17] but the opposite was observed in this case. They later conducted more experiments and proved that emergence of strong lateral field with localized surface plasmon resonance [16] is the reason for the growth of CNWs. Localized surface plasmons are non-propagating excitations of the conduction electrons of metallic nanostructures coupled to the electromagnetic field. These modes arise when a sub-wavelength conductive nanoparticle is placed in an oscillating electromagnetic field. The interaction leads to field amplification both inside and in the near-field zone outside the particle. The metallic curved surface exerts an effective restoring force on the driven electrons. This resonance is called the localized surface plasmon resonance (LSPR) [18].

Wu et al. used Au nanoparticles to excite LSPR on the substrate surface and obtained different flower like patterns on substrate surface along with CNWs. They proved that these patterns emerge during the growth of CNWs due to LSPR of Au nanoparticles [16]. During our experiments, we obtained many similar type of patterns and two of them are shown in Figure 3.7. Presence of these patterns gives an indication of LSPR in this case. However, it is important to note unlike Wu et al. [16] nothing was done intentionally here to modify the localized electric field to enhance plasmonic effect. Also, in our case we did not use any external bias and used a doped Si as a substrate. In spite of all these differences with the experiments conducted by Wu et al. we could possibly see the signatures of LSPR through the presence of the patterns shown in Figure 3.7.

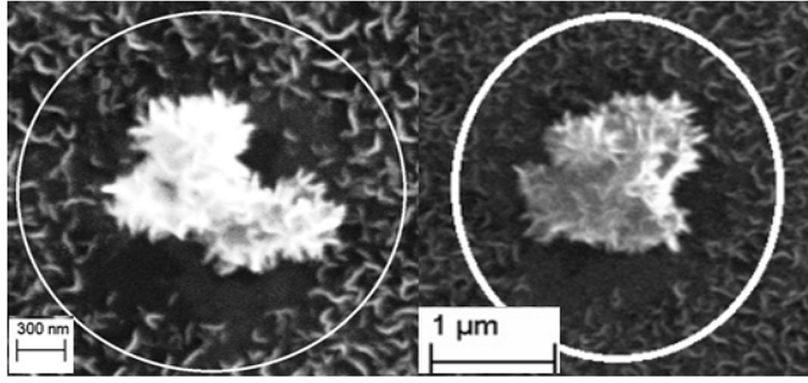


**Figure 3.7:** SEM images of two typical flower-like patterns obtained during deposition of CNWs.

However, it is generally not expected that Ni nanoparticles would respond to LSPR to enhance the electric field over substrate surface. But, recently Yeshchenko et al. [19] have studied surface plasmons resonance in Ni nanoparticles embedded in Silica and identified the band corresponding to the surface plasmons in its absorption spectra. Their extensive work proved that it is possible to excite surface plasmons in Ni nanoparticles. It is known that LSPR occurs due to enhancement in electronic polarizability ( $\alpha$ ) when dimension of the nanoparticles are much smaller than the wavelength of the electromagnetic wave [20]. In such situation  $\alpha$  is given as,

$$\alpha = 4\pi a^3 [(\epsilon_{Ni} - 1) / (\epsilon_{Ni} + 2)]$$

Where,  $a$  &  $\epsilon_{Ni}$  are radius of the Ni nanoparticles and dielectric function of Ni respectively. Using dielectric function data for Ni [21], one can plot

against wavelength ( ) which is shown in Figure 3.8. It shows that

has maxima between 345-400 nm which falls in UV region. Therefore, if ECR plasma can serve as a source radiation in this wavelength region, LSPR of Ni nanoparticles could become possible. Interestingly, ECR plasma in fact, has long been reported as a source of VUV / UV radiation [22, 23]. Unlike microwave plasma used by Wu et al. [15, 16] where LSPR

needed to be excited by using Au nanoparticles, low pressure plasmas are very rich source of UV radiation which can easily trigger LSPR in transition metal nanoparticles.

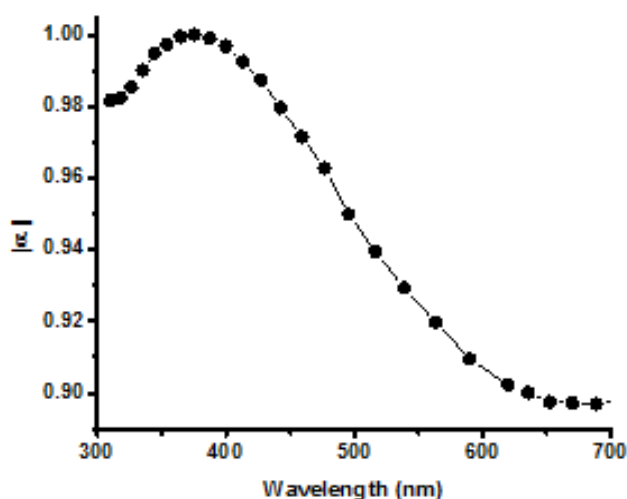


**Figure 3.8:** Electronic polarizability vs. wavelength plot for Ni.

Based on our experimental findings and associated literature survey, we propose an qualitative growth mechanism model for the bias independent growth of CNWs by ECR-CVD. Figure 3.9 shows schematic representation of the growth mechanism of CNWs by this method. The growth mechanism is divided into a four stage process here. In stage 1, 30 nm thick Ni thin film (deposited by magnetron sputtering) which generally becomes  $\text{NiO}_x$  in ambience gets reduced during  $\text{H}_2$  plasma pre-treatment. Depending on optimized pre-treatment time and gas flow rate this film gets converted into large number of Ni nano-islands which is shown schematically in stage 2. After this,  $\text{CH}_4$  is introduced into the CVD chamber for deposition of CNWs. An exaggerated schematic of the situation is shown in the figure as stage 3. Here, a small nano-island is approximated into a spherical nanoparticle and the effect of plasma on this particle is shown. As UV radiation from plasma is continuously being

showered on the Ni nanoparticle it undergoes LSPR provided requisite conditions are met. Transient creation of nanoparticle dipole occurs and electric fields present both outside and inside the nanoparticle gets amplified [21]. Meanwhile, CH<sub>4</sub> gas which acts as the precursor gets decomposed inside the plasma and decomposed ions get accelerated from the plasma sheath towards the substrate where they encounter the high electric field surrounding the nanoparticle. The next step shown is stage 4 where CNWs grow laterally because in absence of any 'vertical' applied bias, 'lateral' enhancement due to LSPR guides the decomposed carbon species to form web-like network on the substrate resulting in formation of CNWs. The direction of the growth inside plasma is decided by the interplay of complex plasma sheath electric field, applied vertical electric field due to external bias and lateral electric field due to the surface plasmons. The growth of CNWs is decided by the dominating electric field. Without the application of an external bias to the substrate there is no guiding vertical electric field on the substrate and in this case the dominating electric field might be the lateral electric field due to surface plasmons. This ultimately results in the deposition of lateral growth resulting in CNW formation.

The model we presented above is qualitative based on the findings of the experiments and more experiments are needed to confirm this model. This type of model explores a new possibility and can be further generalized to suit the growth of any carbon nanostructures. It is well known that any deposition process in PECVD depends on the interplay of plasma sheath electric field and the electric field due to an externally applied bias. Normally both these fields help in attracting positive species to the substrate which help in deposition. In our opinion, not only the electric field but

one should look for the radiation induced changes such as LSPR during plasma processing of materials in low pressure PECVD processes more seriously.

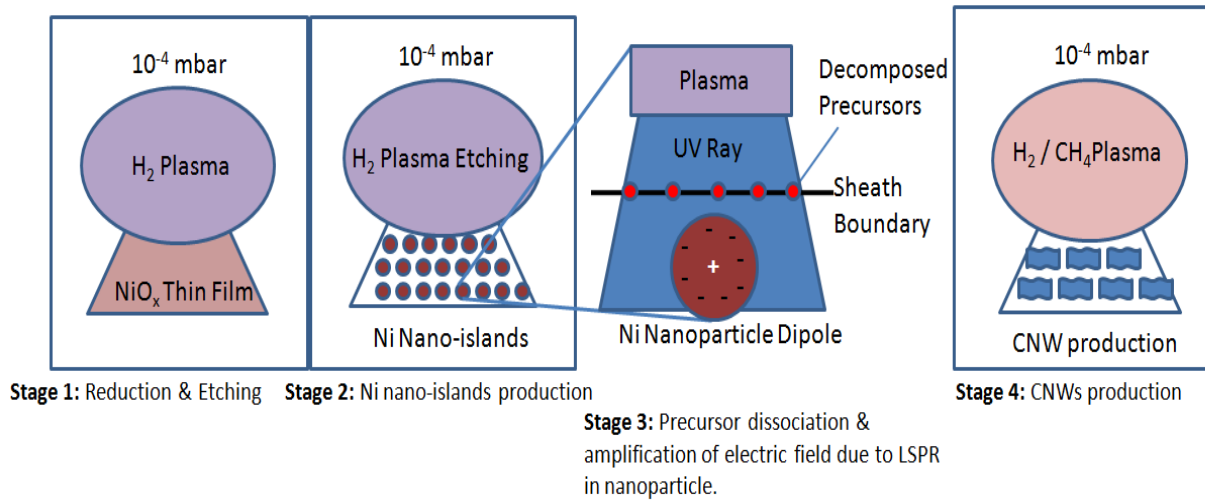


**Figure 3.9:** Schematic representation of different stages during growth of CNWs by ECR-CVD.

### 3.5 Conclusion

The investigations reported here indicate that it is possible to grow high density CNWs on Si substrates without application of external bias to the substrates during the growth using ECR-CVD process. It is also seen that the problem of silicide formation does not occur whether the substrate has a diffusion resistant barrier or not. Characterization results showed that CNWs got deposited on all the four samples but CNWs deposited in the presence of  $\text{N}_2$  had more defects. A qualitative model on the growth mechanism of CNW is also proposed based on the LSPR effect on Ni nanoparticles. A part of this work has already been published in Journal of experimental nanoscience [5].

### References:



1. S. A. Barve, N. S. Nandurkar, N. Chand, S. B. Singh, N. Mithal, Jagannath, B. M. Bhanage, D. S. Patil, L. M. Gantayet, J. Phys.: Conf. Ser. 114 (2008) 012045.
2. J. Asmussen, J. Vac. Sci. technol. 7 (1989) 883.
3. E. Luais, M. Boujtita, A. Gohier, A. Tailleur, S. Casimirius, M. A. Djouadi, A. Granier, P. Y. Tessier; App. Phys. Lett. 95 (2009) 014104.
4. Y.S. Woo, D. Y. Jeon, I.T. Han, Y.J. Park, H.J. Kim, J.E. Jung, J.M. Kim; J App. Phys. 94 (2003) 6789.
5. R. Kar , N.N. Patel , S.S. Chopade , S. Mukherjee , A.K. Das, D.S. Patil, J. Exp. Nanosci. 9 (2014) 575.
6. C.H. Lin, S.H. Lee, C.M. Hsu, C.T. Kuo, Diam. Rel. Mater. 13 (2004) 2147.
7. S.B. Singh, N. Chand, D.S. Patil, Vacuum, 83 (2009) 372.
8. F. d'Heurle, C. S. Petersson, J. E. E. Baglin, S. J. La Placa, C. Y. Wong, J. Appl. Phys. 55 (1984) 4208.
9. K. Tanaka, M. Yoshimura, A. Okamoto, and K. Ueda: Jpn. J. Appl. Phys. 44 (2005) 2074.
10. M. S. Dresselhaus, G. Dresselhaus, R. Saito, A. Jorio, Phys. Rep. 409 (2005) 47.
11. L. M. Malard, M. A. Pimenta, G. Dresselhaus, M. S. Dresselhaus, Phys. Rep. 473 (2009) 51.
12. Z. H. Ni, H. M. Fan, Y. P. Feng, Z. X. Shen, B. J. Yang, Y. H. Wu, The J. Chem. Phys. 124 (2006) 204703.
13. A. K. Gupta, T. J. Russin, H. R. Gutierrez, P. C. Eklund, ACS nano. 3 (2009) 45.
14. A. C. Ferrari, J. Robertson, Phys. Rev. B. 61 (2000) 14095.
15. Y. Wu, B. Yang, Nano Lett., 2 (2002) 355.
16. Y. Wu, B. Yang, B. Zong, H. Sun, Z. Shen, Y. Feng. J Mater Chem. 14 (2004) 469.

17. C.H. Lin, S.H. Lee, C.M. Hsu, C.T. Kuo, *Diam. Rel. Mater.* 13 (2004) 2147.
18. S.A. Maier, *Plasmonics: Fundamentals and Applications*. New York, Springer, 2007.
19. O.A. Yeshchenko, I.M. Dmitruk, A.A. Alexeenko, A.M. Dmytruk, *J. Phys. Chem. Sol.* 69 (2008) 1615.
20. 22. E.W. Palik, *Handbook of Optical Constants of Solids*. Orlando, Academic, 1985.
22. C. Cismaru, J.L. Shohet, *App Phys Lett.* 74 (1999) 2599.
23. T. Yunogami, T. Mizutani, K. Suzuki, S. Nishamatsu, *Jap. J. App. Phys.* 28 (1989) 2172.

## **Chapter 4**

### **Deposition, Characterization and Field Emission Studies on Multi-walled Carbon Nanotubes by MPECVD Method**

#### **4.1 Introduction**

Carbon nanotubes (CNTs) are one of the most researched nanostructures in the world because of their promising applications in diverse fields ranging from electronics to medicine [1-5]. Due to their excellent electron emission properties CNTs have a strong potential application as a cold cathode [6, 7, 8]. Field emission properties have been explored by many researchers and all have tried to enhance field emission current density by a variety of methods like surface modification [9], doping with transition elements or coating of CNT-emitters with a lower work function material and nano-particles [10-12].

For field emission application it is always preferable to grow CNTs directly on the metal surface for ensuring better contact with the conducting substrate. It also offers good mechanical integrity and low contact resistance between CNTs and the substrate [13]. But, this technique requires in-situ formation of catalyst nanoparticles on the substrate [14, 15] which is often difficult to achieve experimentally. Nevertheless, there are some existing reports regarding this type of growth [13-29]. Talapatra et al. [13] have grown vertically aligned CNTs on Inconel substrates using CVD process for applications as double-layer capacitors and field-emitter devices. Yi et al. [14, 15, 20] reported growth of CNTs on Inconel substrates by hot filament chemical vapour deposition (HFCVD) process. They highlighted the necessity of oxidation of Inconel substrates prior to the growth of CNTs and reported that it is not

possible to grow CNTs on Inconel by HFCVD without oxidizing the substrates. Similarly, Gao et al. [22] reported growth of CNTs on Inconel 600 by pyrolysis of Iron phthalocyanine in the presence of  $C_2H_4$  and Hirakawa et al. [18] investigated growth of CNTs on different substrates like Inconel 600, Invar-42, SS 304, and Ni using DC-PECVD and compared their field emission behavior. They obtained maximum current density of around  $6 \text{ mA/ cm}^2$  at an electric field of  $5 \text{ V/ } \mu\text{m}$  for Invar-42. Ting et al [27] investigated field emission behavior of CNTs grown on Fe-Si thin films by a two-step growth process and found that catalyst particles got re-activated in the second step when they switched off the plasma and gas flow for some time and then again restored it for further growth of CNTs. Yang et al. [23] witnessed growth of CNTs during diamond deposition experiments by MPECVD process. In their experiment diamond got deposited on the substrate holder while CNTs got deposited on the Inconel made bottom plate of their substrate holder. Lu et al. [19, 26] have first shown the effect of microwave shield on the growth of CNTs using MPECVD process. They reported about the catalyst assisted growth of CNTs on Cu and Ni substrates and observed that growth of CNTs dramatically increased when one uses a Si wafer as a microwave shield during the growth process. Their work highlighted the problem of microwave reflection from the metal surface and its effect on the growth of CNTs. In a recent work, Sridhar et al. [28] have grown CNTs by water assisted CVD on Si and Inconel 718 substrates with the use of Al buffer layer and Fe catalyst. They obtained a maximum field enhancement factor of 7300 for the grown CNTs. Shin et al. [29] has also recently shown that drastic enhancement on the growth of CNTs on Inconel 600 is possible by air-annealing the substrates prior to the growth. Masarapu et al. [24] and Baddour et al. [25] highlighted the necessity of

surface pre-treatment of SS substrates prior to the growth of CNTs. They discussed about the necessity of prior substrate etching for the successful growth of CNTs.

For our work, we have grown CNTs directly on Inconel 600 substrates by MPECVD without using any external catalyst. Inconel was chosen as the substrate as it has a high Ni and Fe content in it which can act as catalysts for the growth of CNTs. Grown CNTs were characterized by field emission scanning electron microscopy, high resolution transmission electron microscopy, X-ray diffraction, Raman spectroscopy and field emission measurements. Unlike previous reports, our present work systematically introduces the concept of substrate heating and microwave attenuation to understand their effects on CNT growth and its field emission properties. The role of plasma sheath on the growth of CNTs is also investigated and explained unlike previously published reports. Our efforts resulted in enhancing field enhancement factor (FEF) over 6700 which is new for CNTs grown directly on Inconel without application of external catalyst.

## **4.2. Experimental**

Details of the MPECVD set-up has already been discussed in section 2.2 and here Figure 4.1 shows an image of the actual set-up used during these experiments with the important components duly labeled.

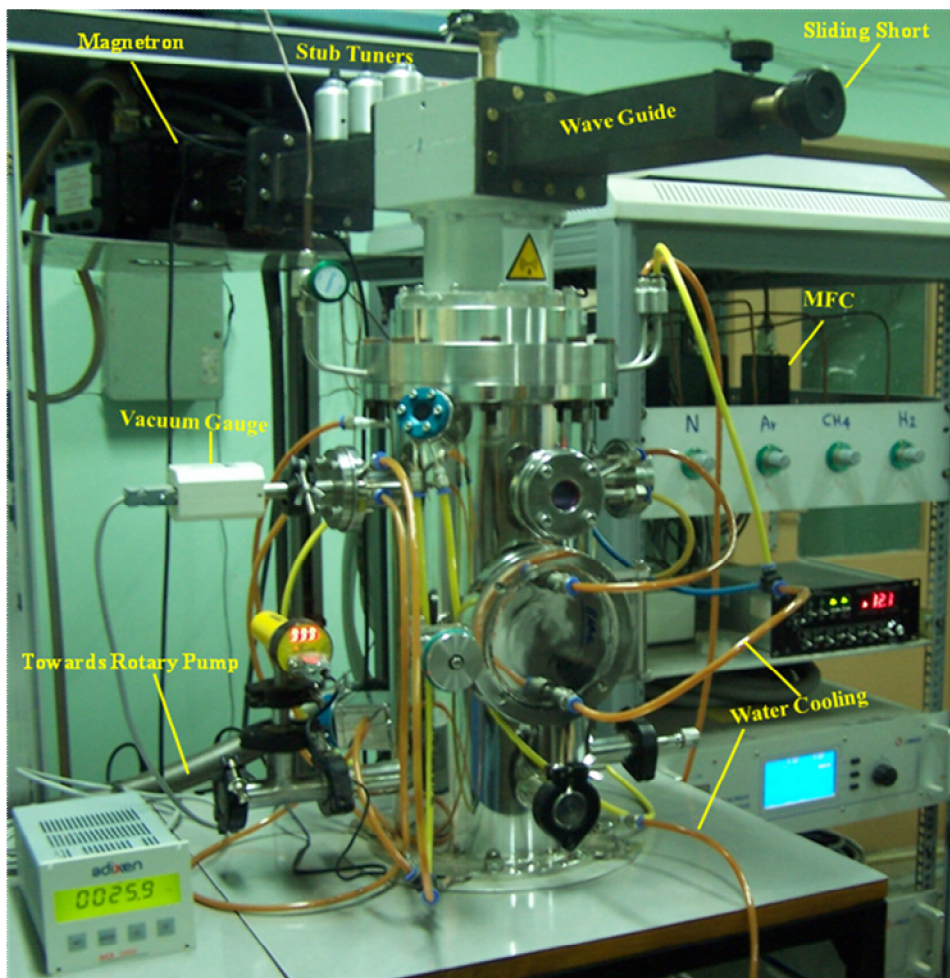


**Figure 4.1:** Actual photograph of MPECVD system used during the experiments.

Initially, Inconel 600 substrates were cleaned ultrasonically in methanol and loaded into the process chamber. Plasma was then generated for pre-treatment of the loaded substrates for which 100 SCCM  $H_2$  gas was fed into the chamber. The idea behind this was to reduce the oxide on the top surface of the Inconel substrate and to prepare fresh transition metal nanoparticles on the substrate surface itself. After 15 minutes of pre-treatment, 20 SCCM  $C_2H_2$  was fed into the chamber along with  $H_2$ , for the growth of CNTs on the substrate. Substrate temperature and deposition time was kept fixed at  $\sim 900^\circ C$  and 5 minutes, respectively. Three different sets of experiments were performed to grow CNTs on these substrates. Above mentioned experimental conditions were kept constant for all these sets but changes were introduced during

substrate preparation for each case. In the first case, as received mirror polished Inconel 600 substrate was kept on the substrate holder inside the chamber. In the 2<sup>nd</sup> case, prior to ultrasonic cleaning in methanol, Inconel 600 substrates were heated in air by heating it to 1100°C. This heated Inconel substrates were cleaned in methanol and used for the growth of CNTs. For the 3<sup>rd</sup> case, a similarly oxidized Inconel 600 substrate was used but while placing it on the substrate holder inside the chamber, a 0.5 mm thick Si wafer was placed on top of it as a microwave attenuator. In the subsequent text these samples will be referred to as samples A, B and C respectively.

After the experiments it was seen that each of the substrates was coated with a black film. Next, these deposited films were characterized by various characterization techniques to study their morphology, bonding and field emission behavior. A Carl Zeiss EVO 40 scanning electron microscope (SEM) and Carl Zeiss Auriga field-emission SEM (FESEM) were used to investigate the morphology of the substrate and deposited films. For further investigations on the grown structures a FEI Tecnai G2 F30 high resolution transmission electron microscope (HRTEM) with Gatan image filter facility was used. The TEM specimens were prepared by scratching the CNT films from the substrate followed by dispersing them in methanol through ultrasonication. One drop of such solution was taken onto a carbon coated grid and allowed to dry overnight under a lamp. These samples were then taken for microscopic analysis. Reinshaw inVia micro-Raman analyzer with a 514.5 nm Ar ion laser was used for assessing quality and associated defects of the deposited CNTs by Raman spectroscopic measurements. A Rigaku Miniflex II - X-ray diffractometer (XRD) was used for diffraction analysis of the substrate for assessing the differences before and after the substrate heat-treatment. Finally, field-emission of the grown

three samples was studied by an indigenously developed field-emission characterization unit to be described in next section.

### **4.3. Characterization Results**

#### **4.3.1 Electron microscopy**

Figure 4.2 (a-h) shows the SEM / FESEM images of all three samples and their associated histogram plot. Figure 4.2 (a-c) shows the SEM images of the substrate and CNT grown for sample A in different stages. Figure 4.2a shows the as received mirror polished Inconel substrate which was used for the experiment. Apart from the scratches present due to machining there are no special features on the surface. Figure 4.2b shows the same substrate after H-plasma pre-treatment. After the pre-treatment, roughness caused by H- plasma etching can be seen along with machining scratches. Figure 4.2c shows FESEM image of the grown CNTs for sample A and it is seen that short and bundled tubes are grown in this case. Figure 4.2 (d-f) shows the details of sample B in different stages. Figure 4.2d shows the Inconel substrate surface just after heating it in the air at 1100°C. It is seen that heating completely changes the surface morphology of the substrate in this case. The surface seems to be made of different fragments protruding out of the surface. Figure 4.2e shows the same surface after H-plasma pre-treatment. As expected, pre-treatment etches out the surface and produces finer particles on the surface. Figure 4.2f shows the FESEM image of formation of CNTs for sample B and it shows that forest like growth occurs on the surface without any preferred orientation in this case. Here, it is seen that length of the CNTs and their growth rate have increased compared to sample A. Figure 4.2g shows the FESEM images on sample C after deposition. As mentioned earlier, substrate condition for samples B and C are same except the use of microwave



attenuator on sample C during deposition. So, Figures 4.2d & e can be treated as the images of the substrate before deposition and after pre-treatment respectively in this case also. CNTs observed in sample C are the longest among three samples and most of them are well above 10  $\mu\text{m}$  in length. The low-resolution SEM image provided as the inset image in Figure 4.2g shows long nanotubes grown in sample C. The growth rate in this case is very high and CNTs grow horizontally without any preferred orientation as in previous cases. The FESEM image also reveals that there is complete absence of unwanted carbon soot apart from CNTs. Figure 4.2h shows the associated histogram plot of diameter distribution of the three samples. It is seen that while sample A & B has comparable average diameter distribution, sample C has much larger average diameter compared to the two samples. From the histogram plot it can be undoubtedly said that in all the three cases, multi-walled carbon nanotubes (MWCNTs) have grown on the substrates as single walled carbon nanotubes (SWCNTs) will always have diameter below  $\sim 5\text{nm}$ .

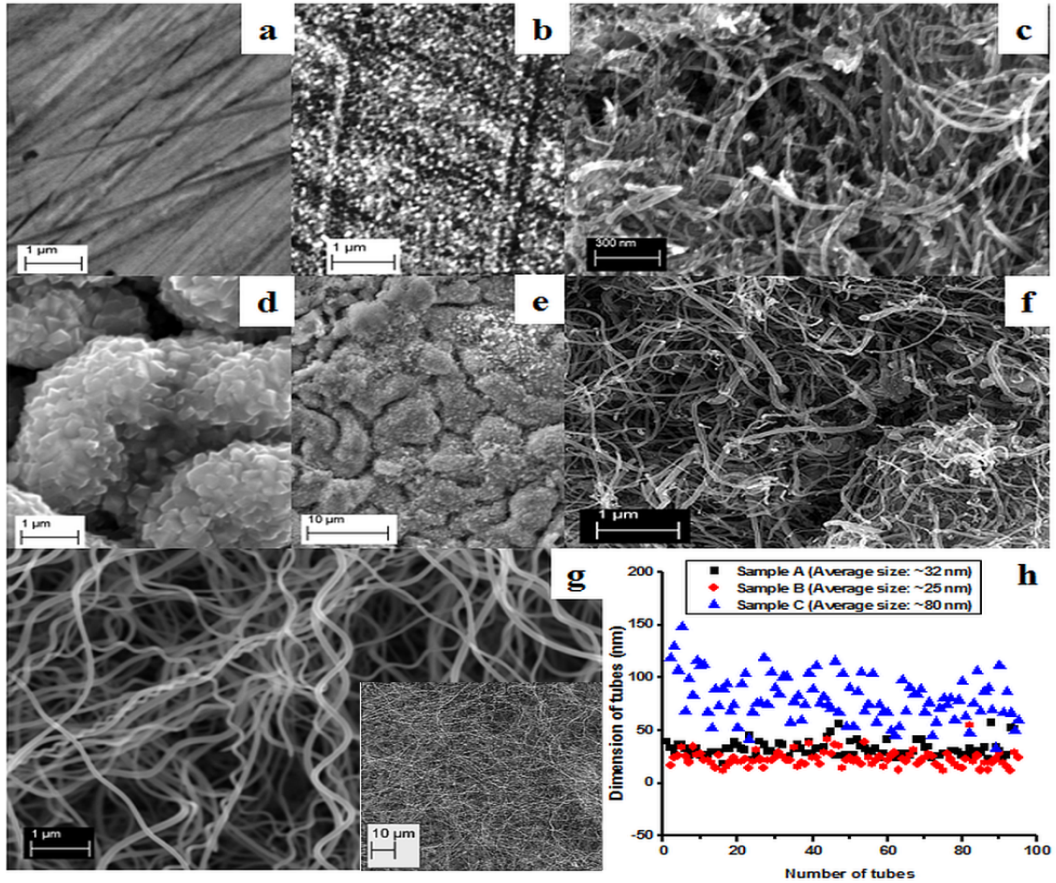


**Figure 4.2:** (a) SEM image of the as-received Inconel substrate, (b) As-received Inconel substrate after H<sub>2</sub> plasma pre-treatment, (c) SEM image of CNTs grown in sample A, (d) SEM image Inconel substrate heat-treated at 1100°C, (e) SEM image of heat-treated Inconel substrate after H<sub>2</sub> plasma pre-treatment, (f) FESEM image of CNTs grown in sample B, (g) FESEM image of CNTs grown in sample C; inset image showing low resolution SEM image for this sample, (h) Histogram plot of diameter distribution of CNTs grown for all three samples.

Figure 4.3(a-g) shows the TEM & HRTEM analysis of the three samples. Figure 4.3a shows TEM image of sample A, showing few MWCNTs at the top portion with a lot of amorphous carbon, a big tubular structure and some metallic portions (black spots) at the bottom. Figure 4.3b shows the HRTEM image of this sample. The hollow cores seen in the image confirms the formation of CNTs. In some cases

formation of carbon nanofibers (CNFs) are also seen. Defects are seen in this image in the wall of the tubes and in the form of a graphitic loop are marked by arrows. Figures 4.3c & d show HRTEM images of sample B. While Figure 4.3c shows the image of bundled tubes present in the sample; Figure 4.3d shows HRTEM image of a MWCNT where the black spot present inside the tube indicates trapping of a metal nanoparticle in the core of the tube. The image also shows the presence of defect in the walls of the MWCNTs marked by an arrow in the figure. Figures 4.3e & f show the HRTEM images of sample C. Figure 4.3e shows that CNTs grown here are almost free from unwanted amorphous carbon deposition but there are places where metal nanoparticles are trapped in the core here just like in the case of sample B (black spots inside the tubes). Figures 4.3e & f show the presence of bamboo-like defects (marked by arrows) in the CNTs. Presence of these defects is only seen for sample C among the three samples.

Figure 4.3g shows the STEM-XEDS analysis of metal nanoparticles trapped in the core of CNTs. Peaks corresponding to Fe and Ni are found in the STEM-XEDS analysis which indicates that nanoparticles which got trapped inside the CNTs are in general nano-fragments of the substrate Inconel. After comparing electron microscopy results of samples A, B, & C it can be easily said that most dense and longest CNT formation occurred for sample C. From the FESEM images on different samples, it is also seen that quality of grown CNTs improved dramatically when the substrate is heat-treated and a microwave attenuator is added during deposition. The changes brought by combination of these two aspects can be seen by comparing Figures 4.2c & 4.2g.

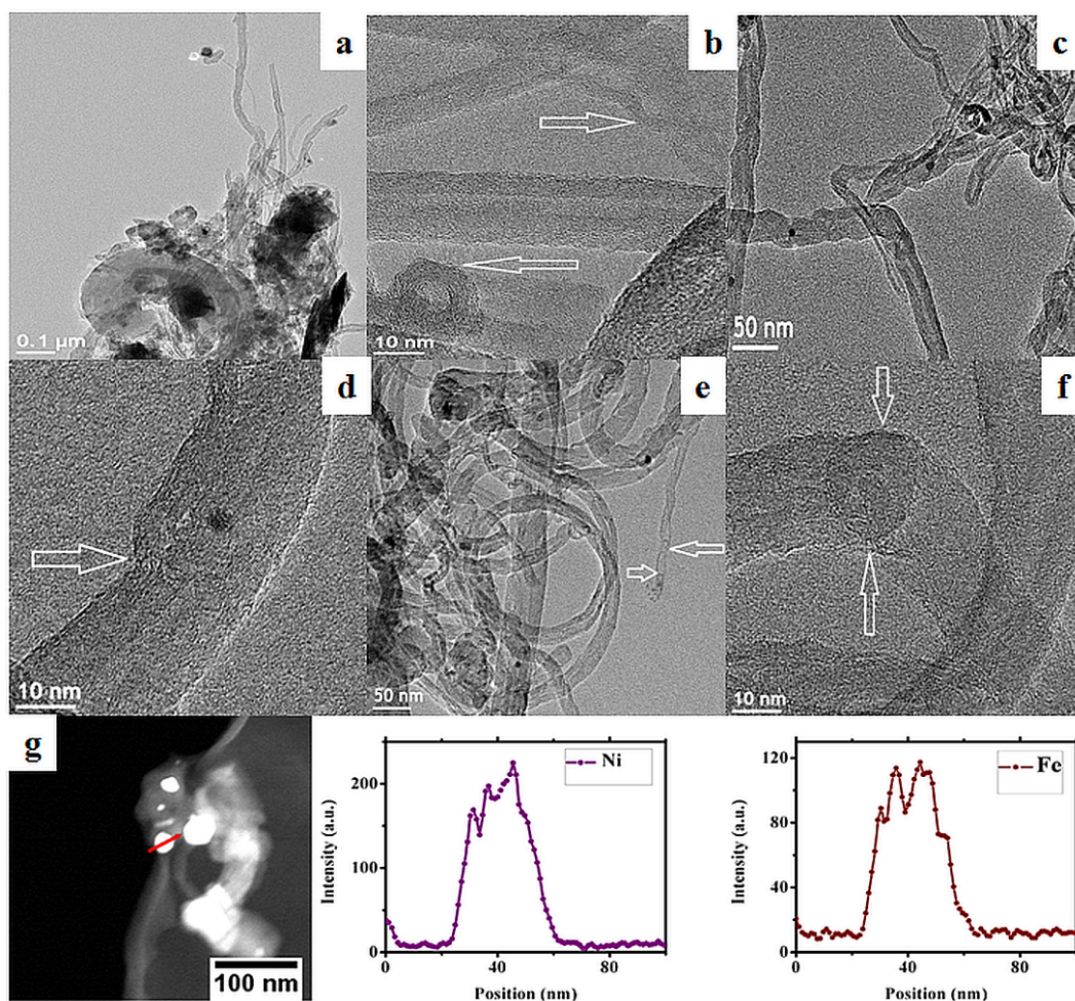


**Figure 4.3:** (a) TEM image of sample A showing large metal particles along with CNTs, (b) HRTEM image of sample A showing hollow core and defects marked by arrows, (c) HRTEM image of sample B showing clusters of CNTs with varied diameter distribution, (d) HRTEM image of a CNT in sample B showing defect on the wall of the tube (marked by arrow) and presence of trapped metal nanoparticle inside the core, (e) HRTEM image of CNTs in sample C showing large number of CNTs, bamboo like defect shown by arrows, (f) bamboo-like defect shown in a CNT marked by arrows in sample C, (g) STEM-XEDS analysis of a typical metal nanoparticle showing presence of Ni & Fe in nanoparticles.

#### **4.3.2 X-Ray diffraction (XRD)**

Figure 4.4 shows the comparison of XRD spectra taken on the as received Inconel and heat-treated Inconel at 1100<sup>0</sup>C. While the as-received Inconel shows the presence of XRD peaks corresponding to Inconel 600 (Cr 0.18, Fe 0.09, Ni 0.73) only, the heat-treated Inconel indicates the additional presence of Fe<sub>3</sub>O<sub>4</sub> and Cr<sub>2</sub>O<sub>3</sub> apart from the peaks corresponding to Inconel substrate. By comparing SEM images of Figures 4.2a & 4.2b with 4.2d & 4.2e along with the Figure 4.4, it can be said that protruded regions (Figure 4.2d & 4.2e) are produced in the case of heat-treated Inconel, as Cr and Fe oxides comes to the surface due to diffusion during heating and the grain boundaries become more prominent in this process [14]. Precipitation of Cr along the grain boundary has earlier been seen for heat-treatment of Inconel at lower temperatures of 800<sup>0</sup>C [30]. It seems that heat-treatment at higher temperature also cause precipitation of Fe along with Cr in the grain boundary. The two spectra at Figure 4.4 also shows slight shift of Inconel peaks towards higher angle after heat-treatment and also there are changes in the relative normalized intensities in both the cases. The slight shift might be due to the slight change in lattice parameters due to thermal stress which developed during heat-treatment and the changes in relative intensities may be attributed to the occurrence of new oxide phases which causes structural changes on the surface of the alloy.

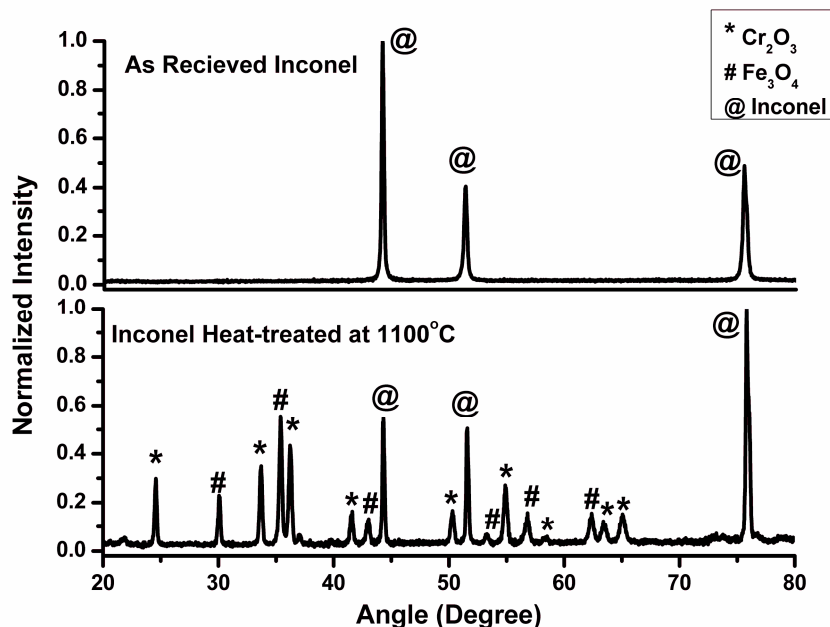


**Figure 4.4:** Comparison of XRD spectrum of as-received and heat-treated Inconel substrate.

#### 4.3.3 Raman spectroscopy

Figure 4.5(a-c) shows the Raman spectra taken on samples A, B & C respectively. All samples are showing the presence of D and G bands confirming the growth of CNTs in them. These bands are de-convoluted and shown in the figures for all three samples. The de-convoluted bands are shown in green and the fitted spectra are shown in red for all cases. De-convolution shows the emergence of D' Raman band inside G band for all three cases. Peak positions, ratio of integrated intensities of different peaks, full width at half maxima (FWHM) are few important parameters to form a quantitative idea about these samples. Table 4.1 shows data obtained from Raman spectroscopic measurement on these three samples. D band originates from the disorder induced mode in graphite of the same name and it signifies defect in carbon systems [31-33]. This band appears at  $1350\text{ cm}^{-1}$  for 2.41 eV (514.5 nm) laser and it shifts  $50\text{ cm}^{-1} / \text{eV}$  with change in probing energy [32]. G band is the only band which



originates from the first order Raman spectrum of CNTs around  $1580\text{ cm}^{-1}$  [32] and it signifies the presence of crystalline graphitic structure in the sample. It originates from the in-plane C-C bond vibration and is of non-dispersive nature.  $D'$  is another second order Raman band that appears as a shoulder peak of G band and visible around  $1620\text{ cm}^{-1}$ . This peak is observed in some disordered graphitic carbon structures including graphene [31-33]. This peak is not possible to occur under defect free conditions.

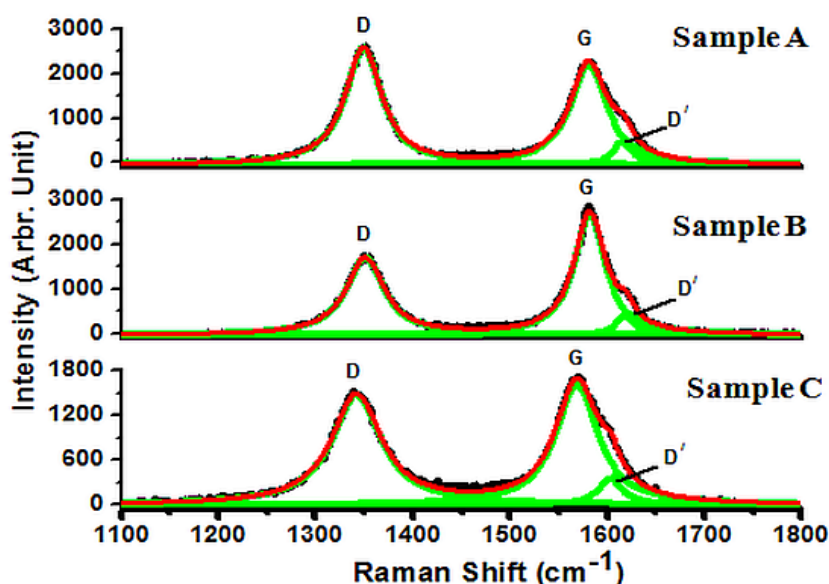


**Figure 4.5:** Deconvoluted micro-Raman image of samples A, B & C showing presence of D, G and  $D'$  peaks.

From Table 4.1 it is also seen that integrated intensity ratios of D & G band designated as  $I_D/I_G$  shows a minimum for sample B and almost comparable for samples A & C.  $I_D/I_G$  ratio is considered defect dependent [34, 35]. Decrease in this value indicates decrease in the defect density for CNTs. From the table it appears that sample B has the least defect density among these samples. Sample A shows slightly higher defect density than sample C. However, Antunes et al. [35] have pointed out

that finding defects from  $I_D/I_G$  ratio alone in case of MWCNTs is not appropriate as curvature effects induce variation on the D band relative intensity or linewidth. The product of FWHM (D) and  $I_D/I_G$  is a better parameter to conclude the overall defect density. From the table it is seen that this product is maximum for sample C and minimum for sample B while sample A has an intermediate value closer to sample C. Therefore sample C is the most defective sample among the three and sample B is the least defective one. Increase of FWHM of D, G is also related to defects in the MWCNTs [35]. However, the exact type of the defects cannot be deduced from them. From the table it is seen that the trend of FWHMs of G and  $D'$  is similar to that of the  $(FWHM(D) \times I_D/I_G)$  ratio. These observations confirm that sample C in spite of having the highest growth rate among the three also has the highest defect density. It is apparently paradoxical that sample C in spite of being free from amorphous soot, turned out to be the most defective in Raman analysis. It seems that the reason behind this is that majority of the defects produced in sample C are inherent in the tubes itself unlike other two samples which can be justified from the presence of bamboo-like defects in this sample (Figure 4.3f).

Another important observation from the Table 4.1 is the downshifting of all peaks to lower wave numbers for sample C compared to sample A and B. While  $\sim \pm 2 \text{ cm}^{-1}$  shift is considered normal [36] the observed shift for sample C is much higher. Here D, G,  $D'$  are down-shifted by  $\sim 7, 12, 16 \text{ cm}^{-1}$  respectively. The down-shifting of Raman peaks for CNTs is normally understood on the basis of strains produced in C-C bonds [36]. Elongation of C-C bond causes strain, making the bond weaker and eventually lowers the vibrational energy. Our results suggest that CNTs grown in case of sample C are strained. It should be mentioned that high value of laser power is



sometimes found to be responsible for strained CNTs during Raman spectroscopic measurements as excessive heating may induce damages in the tubes. However here 0.4 mW laser power is used for all three samples which is much less compared to the values quoted in literature [37, 38] to cause any significant laser heating in the tubes damage them structurally. Also, same laser power has been used in all three cases, hence there is no reason why the sample C alone would be affected by laser heating. Moreover, 0.4 mW  $\text{Ar}^+$  laser with focusing diameter of  $\sim 3 \text{ mm}^2$  could not be suspected as significant power density ( $0.13 \text{ mW/mm}^2$ ) as the thermal conductivity of Inconel 600  $\sim 15 \text{ W} \times (\text{m} \times \text{K})^{-1}$ . It is therefore reasonable to assume that the strain present in grown nanotubes (sample C) originated during the growth process itself rather than being generated during Raman spectroscopic studies. Also higher strain could be correlated to the presence of defects in sample C which is found to be the highest among the three samples.

**Table 4.1:** Raman spectroscopic measurement data for three samples

Samples	Raman shift ( $\text{cm}^{-1}$ ) & FWHM			$I_D/I_G$	FWHM (D)* $I_D/I_G$
	D band (FWHM)	G band (FWHM)	D' band (FWHM)		
Sample A	1349.47 (46.05)	1580.51 (45.43)	1616.19 (24.95)	1.18	54.34
Sample B	1351.44 (47.94)	1581.68 (38.35)	1619.04 (23.03)	0.80	38.35
Sample C	1342.38 (62.84)	1568.64 (51.97)	1603.63 (30.42)	1.10	69.12

#### 4.3.4 Field emission measurement

The schematic of the field emission measurement set-up is shown in Figure 4.6. This indigenously developed set-up consists of a vacuum chamber, a fixed cathode holder and a movable anode assembly. The cathode holder is made up of stainless steel and is electrically insulated from the chamber and connected to the high-voltage power supply through a feed through in the cathode flange. The CNT grown substrates were kept on the cathode holder and the distance between the emitting surface and the anode could be adjusted using a micrometer controlled translational stage. A minimum gap of 20 micron and a maximum gap of 5 cm could be provided by this arrangement. The measurement chamber was initially evacuated to  $1 \times 10^{-6}$  mbar and all the measurements were done under this condition. A DC voltage power supply was used to bias the cathode and field emission current was measured with micro ampere accuracy.

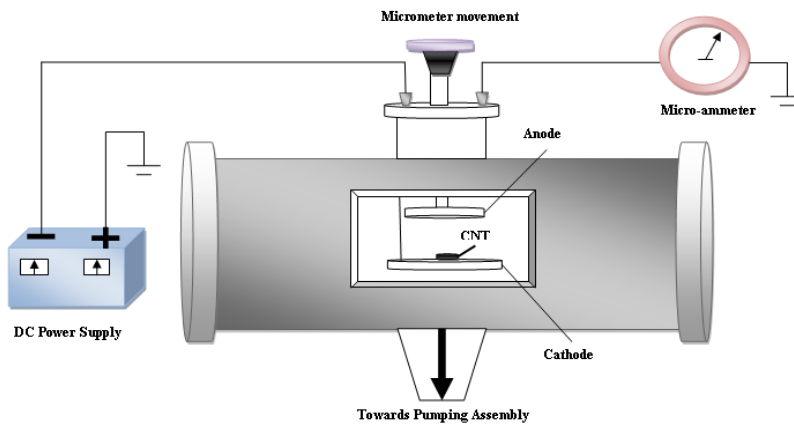


**Figure 4.6:** Schematic diagram of field-emission set-up used in the experiment.

Figure 4.7 shows field emission measurement results on the samples A, B and C respectively. It is known from the previous works [15, 18, 39, 40] that field emission from CNTs is governed by Fowler-Nordheim (F-N) equation as given below [39-41].

$$J = (A\gamma^2 E^2 / \phi) \exp [(-B \phi^{3/2}) / (\gamma E)] \quad (4.1)$$

In the above equation  $J$  is the emitted current density ( $A/m^2$ ),  $\phi$  (eV) is the work function,  $E$  is the local electric field and the constants  $A$  and  $B$  are  $1.541 \times 10^{-6} A eV V^{-2}$  and  $6.831 \times 10^9 eV^{-3/2} V m^{-1}$ , respectively and value of work function  $\phi$  is taken as 4.7 eV [41],  $\gamma$  is the field enhancement factor (FEF) which indicates the quality of the CNTs that are responsible for field emission. Equation 4.1 can be rewritten as,

$$\ln J = \ln [A (\gamma^2 E^2 / \phi)] - (B \phi^{3/2} / \gamma E) \quad (4.2)$$

From equation 4.2 it is seen that, a plot of  $\ln J$  vs.  $1/E$  should be linear and FEF can be calculated from the slope of the graph. Figure 4.7a shows current density ( $J$ ) Vs. Electric field ( $E$ ) plot for all the three samples while the inset image shows  $\ln J$  vs.  $1/E$  plots for these samples. From this figure, it is clearly seen that current density increases continuously from sample A to sample C. Sample C showed the best result where a maximum current density of  $14.6 mA/cm^2$  was observed at a low electric field of  $1.6 V/\mu m$ . Figure 4.7b shows a plot of turn-on field vs. FEF for these three samples. Here turn-on field is defined as the electric field for which current reaches  $10 \mu A/cm^2$ . From Figure 4.7b, it is evident that FEF systematically increased (from sample A to C) with decrease in turn-on electric field, a maximum FEF of 6740 was observed in case of sample C.

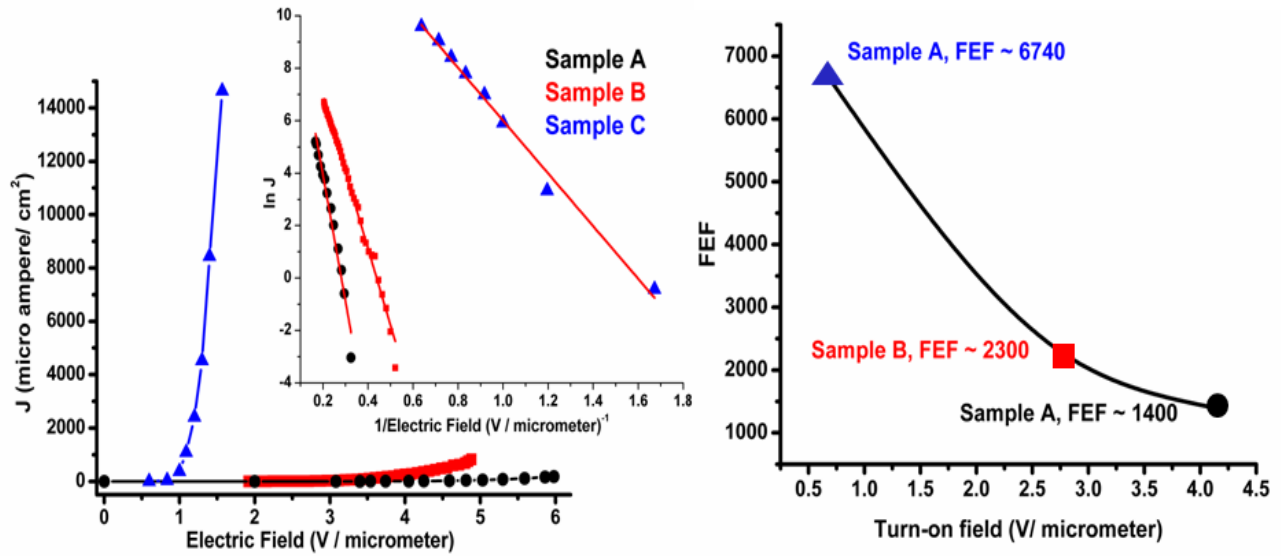


**Figure 4.7:** (a)  $J$  vs.  $E$  plot for sample A, B & C. Inset image showing  $\ln J$  vs.  $1/E$  plot for three samples, (b) Variation of Turn-on voltage vs. Field enhancement factor for samples A, B and C.

#### 4.4. Discussion

Effect of heat-treatment of Inconel substrate has been discussed previously by Yi et al. [13, 14] who mentioned that it is not possible to grow CNTs on Inconel via HFCVD without heat-treatment. Contrary to this, we found CNTs can grow even in absence of heat treatment by MPECVD process (sample A). Plasma has abundant number of highly energetic species which helps in the efficient decomposition of precursor leading to the formation of CNTs for sample A. However, heat-treatment of the substrates prior to deposition certainly enhances density of CNTs and improves their field emission behavior as seen from the characterization results. From SEM analysis (Figures 4.2a & 4.2d) and XRD results (Figure 4.4), it is seen that Inconel undergoes a surface modification during heat-treatment. It is seen that continuous grain-boundary of Inconel 600 before heat-treatment changes into semi-continuous nature after heat-treatment is done. It is also evident that Cr and Fe which was

uniformly distributed prior to heat-treatment, precipitates along the grain boundaries forming oxide phases [30].

During H-plasma pre-treatment, these oxidized phases get reduced to produce fresh transition metal nanoparticles which act as catalyst for growth of CNTs. The carbon-containing precursor gas gets decomposed at the surface of the catalyst particle (Ni & Fe in this case), and the carbon is transported to the edges of the particle, where it forms the nanotubes. However, some of these nanoparticles come inside the core of the CNTs during its formation (Figures 4.3c-e). This is why only metal particles were found during STEM-XEDS analysis and not their oxides. In our opinion changes on the surface morphology of Inconel surfaces increases the presence of active sites for CNT growth in case of the heat-treated Inconel substrates resulting in denser growth of CNTs in case of sample B. Alloy nanoparticle consisting of Fe and Ni are seen inside the tube (Figure 4.3g) indicates that they are acting as catalyst for growth of CNTs. Also Cr & Fe being transition metal can combine relatively easily with C by thermally assisted diffusion process. The segregation of separate Cr & Fe phases thus enhances the growth rate for sample B.

From the SEM images (Figures 4.2c, 4.2f and 4.2g), it is also seen that the grown CNTs show a dense forest like lateral growth whereas vertical array of CNTs are preferred as ideal field emitter in literature. In spite of this lateral growth a good FEF is observed here. The reason could be the fact that emission from CNTs in our case has been less hampered by screening effects from neighboring tubes [42-44]. In their extensive studies on the screening effect on the field emission behavior of CNTs, Nilsson et al. [44] have shown that morphology of the individual CNTs as well as the distance between two CNTs are critical for getting high field-emission current density.

Too many CNTs per unit area would essentially make it a flat metal film without any significant field penetration. They concluded that growth of CNTs with medium density and high aspect ratio shows optimum field emission performance. Suh et al. [43] showed that FEF increases with aspect ratio initially and attains a maxima when inter tube distance is comparable to tube height and then it decreases again when inter tube distances become less than the tube height. Kimura et al. [42] showed that this screening effect is less of a problem for lateral growth and hence it enhances the field emission current density of CNTs. Thus, the lateral forest like growth that is observed in our case may actually help in enhancing the FEF here instead of reducing it.

Contact between CNTs and the substrate has also been a major factor affecting their field emission behavior. Normally, it is seen that if the contact resistance is high it causes resistive heating which in turn would reduce field emission current. Further, increasing electric field may cause sublimation or melting of CNTs. To keep contact resistance a minimum it is generally preferred that substrate and CNTs have comparable work function value [45]. In our case, for sample A we used as-received Inconel as substrate which has a work function value  $\sim 4.8$  eV [46] close to that of CNTs (4.7 eV). For sample B and C, Inconel was heat-treated at  $1100^{\circ}\text{C}$  which resulted in the formation of additional  $\text{Cr}_2\text{O}_3$  and  $\text{Fe}_3\text{O}_4$  phases on its surface as seen from XRD results. From literature, it is seen that  $\text{Cr}_2\text{O}_3$  has a work function  $\sim 4.8$  eV [47] but  $\text{Fe}_3\text{O}_4$  has work function  $\sim 5.5$  eV [48] which is higher than that for CNTs'.

To understand their respective effects on the substrate-CNT interface, we have performed energy dispersive X-ray spectroscopy (EDS) on the heat-treated Inconel after their pre-treatment with  $\text{H}_2$  plasma. Figure 4.8 shows the EDS spectrum of the sample along with the elemental composition. The figure shows presence of Cr, Mn,

Ni, Si, Fe and O. Cr and O peaks are merged near 0.5 eV in the figure. From the elemental composition presented, it is seen that amount of Fe on the surface is very small compared to Cr. So,  $\text{Cr}_2\text{O}_3$  will be the major phase after heat-treatment and not  $\text{Fe}_3\text{O}_4$ . Thus contact resistance will mostly be determined by  $\text{Cr}_2\text{O}_3$  and not by  $\text{Fe}_3\text{O}_4$ . Hence, the contact resistance even after heat-treatment of the substrate is not expected to be very high. By combining XRD results (Figure 4.4) and the EDS result presented here it can be concluded that heat-treatment modifies the external surface of Inconel with partial formation of  $\text{Cr}_2\text{O}_3$  and  $\text{Fe}_3\text{O}_4$  while original Inconel phases also remain present.  $\text{Cr}_2\text{O}_3$  and Inconel both have matching work function with CNTs and this would lead to low contact resistance between substrate and deposited CNTs.

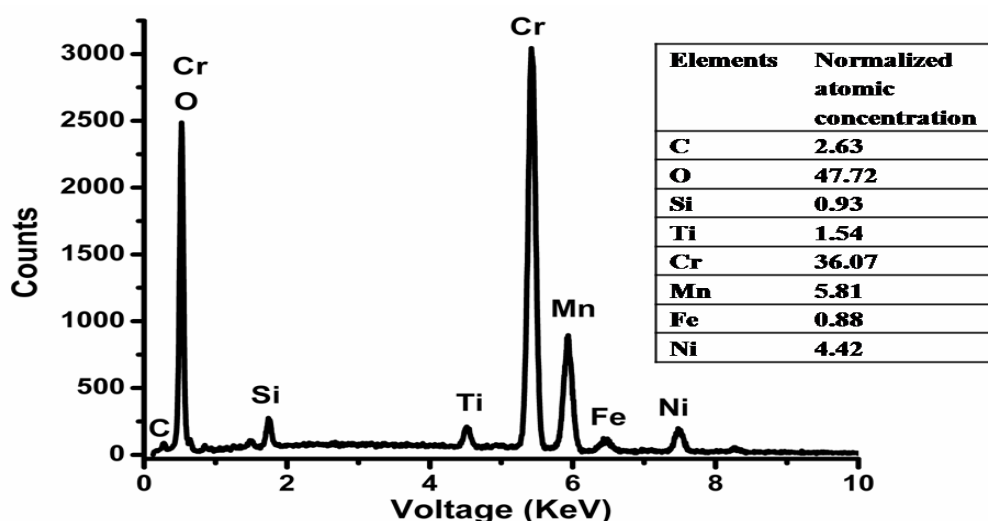


**Figure 4.8:** EDS spectrum of the heat-treated Inconel substrate with elemental composition of different elements present.

From Figure 4.2g it can be easily seen that CNTs grown in sample C have the highest growth rate and highest aspect ratio compared to other two samples. This is definitely a reason for such high field emission observed from sample C. Interestingly, this sample also has maximum defects as seen from Raman spectroscopic analysis results (product of FWHM (D) and  $I_D/I_G$  is maximum for this sample). It has been

observed that defects in the grown nanotubes sometimes actually help in field emission by lowering the turn-on voltage [49-51]. FESEM images for sample C (Figure 4.2g) showed clear MWCNT formation without any amorphous soot. So, this defect probably occurred due to bamboo-like structures as seen in the HRTEM image for sample C (Figure 4.3e & 4.3f). Our results suggest that bamboo-like structures is one of those rare favorable defects which actually help in increasing field emission current density and FEF. Bamboo-like defects seem to be a major reason for maximum FEF in sample C in spite of being most defective. In fact, N<sub>2</sub> has been specifically used during CNT deposition experiments to generate bamboo-like defects for obtaining enhanced field emission behavior [49, 50]. Although, we did not add N<sub>2</sub> during the experiment still bamboo-like growth was observed in case of sample C. This defect normally arises when tube close and re-nucleation occurs again from the tube end [49]. In a molecular dynamics study Ding et al. [52] have shown that bamboo-like CNTs can only grow at high dissolved carbon concentrations. Though there was no change in the feed rate of C<sub>2</sub>H<sub>2</sub> for deposition of all samples in our study bamboo-like defect was observed only in case of sample C.

The main difference between samples B & C was that sample C was covered with a Si wafer during deposition. This Si wafer was used as the microwave attenuator on top of the oxidized Inconel surface. Use of microwave attenuator for the growth of CNTs has been reported earlier by Lu et al. [19]. They have reported that in case of MPECVD process, plasma was unable to enhance the growth rate of CNTs when a metal substrate was used. This happened since microwave got reflected from the metal surface and this reflection loss hindered the deposition of different species onto the substrate thereby affecting the growth rate.



To enhance the carbon nanotube growth rate it is beneficial to make use of microwave attenuator on the top of the growing substrate surface during the growth. Equation 3 shows the shielding effectiveness (SE) of a material.  $SE_A$  represents absorption loss,  $SE_R$  represents reflection loss and  $SE_M$  represents multiple reflection loss term in the equation.

$$SE = SE_R + SE_A + SE_M \quad (4.3)$$

Equations 4.4 to 4.7 give details of the different terms presented in equation 4.3 [53].

$$SE_R = 39.5 + 10 \log (\sigma / 2\pi f \mu_p) \quad (4.4)$$

$$SE_A = 8.7 (t/\delta) \quad (4.5)$$

$$SE_M = 20 \log |1 - e^{-(2t/\delta)}| \quad (4.6)$$

$$\delta = 1 / (\pi f \mu_p \sigma)^{1/2} \quad (4.7)$$

Where  $\sigma$ ,  $f$ ,  $\mu_p$ ,  $t$ ,  $\delta$  are electrical conductivity of the attenuator material, frequency of incident radiation, magnetic permeability of the shield material, thickness of the shield and skin depth of the shield material respectively.

In the present experiment we have used a p type boron doped Si wafer of thickness 0.5 mm having  $\sigma$  value as 1 S/ cm. Using equation 4.7 one can calculate  $\delta \sim 1$  mm. Now since, thickness of attenuator in our case is lesser than the skin depth, some effectiveness of the shield will be lost due to multiple reflections [26]. Using above equations, one can obtain  $SE_R = 17$  dB,  $SE_A = 4.35$  dB,  $SE_M = -4$  dB and value of 17.35 dB has been obtained for SE in our case. It roughly means that only  $\sim 1.85$  % of incident power gets transmitted to reach the substrate. Thus, in the case of sample C, attenuation helps in stopping the microwaves from reaching to the substrate to major extent so that it cannot get reflected from Inconel surface.

To estimate the extent of actual gap between Si wafer and heated Inconel substrate, stylus profilometry of both these surfaces have been conducted to measure their roughness. It is seen that Inconel wafer alone has a roughness  $\sim 0.4 \mu\text{m}$  while backside of Si wafer adds another  $\sim 0.3 \mu\text{m}$  to it. So, a gap of  $\sim 0.7 \mu\text{m}$  is expected when Si wafer is placed on top of a heated Inconel substrate. Since the substrate is covered from the top, decomposed precursor now cannot directly reach from the top to the substrate surface and it has to travel a longer way from the four sides to reach the substrate. The actual photograph of an Inconel substrate with Si wafer on top of it is shown in Figure 4.9a while an exaggerated schematic of the situation within plasma is shown in Figure 4.9b. As shown in the figure, plasma glow finishes just above the Si wafer and  $\sim 0.7 \mu\text{m}$  gap which remains dark during operation forms a part of the plasma sheath through which decomposed carbon species (ions/ radicals) can still reach the substrate promoting rapid growth of CNTs. Also once these species reach the substrate their residence time would increase due to the presence of the attenuator over it. This situation is pictorially described in Figure 4.9b where sputtered out decomposed precursor are again reflected back to the substrate surface. This would definitely increase the chance of carbon radicals to get dissolved in the transition metal nano structures causing increase in nucleation density for formation of CNTs on the substrate. This is another reason why growth rate and length of CNTs increased dramatically for sample C. Also carbon radicals would now have more time to form crystalline structure which is evident as amorphous soot was non-existent on this sample.

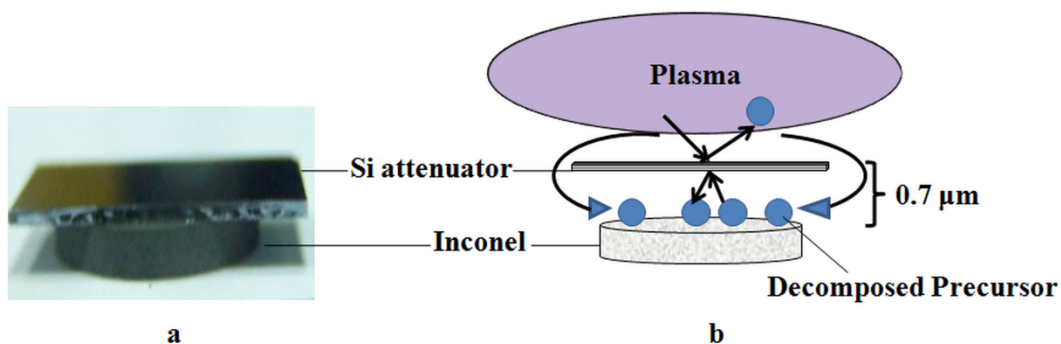


**Figure 4.9:** (a) Photograph of Inconel substrate with Si wafer on top, (b) Schematic diagram showing how reflector helps in increased deposition rate of CNTs.

The growth rate here became so high that it actually led to tube closure and re-nucleation leading to bamboo-like growth. They prevented stagnation of growth and thus helping in elongating the tubes further. It is also seen from Raman spectroscopic results that all major Raman bands for sample C are down-shifted which is a signature of strains occurring between C-C bonds in the CNTs. The very high growth rate and bamboo-like defects for the sample C might be the reason for occurrence of strains in the sample C. By comparing electron microscopy images (Figures 4.2c, 4.2f and 4.2g) one can clearly see that the combined effect of heat-treatment of the substrate, microwave attenuation and increased residence time resulted in the formation of most dense and longest CNTs in case of sample C that in turn also resulted in improved aspect ratio of CNTs here. Combination of high aspect ratio, improved density and bamboo-like defects resulted in the sharp enhancement of FEF for sample C with lower turn on voltage (Figure 4.7b).

#### 4.5. Conclusion

The investigations reported here show the systematic changes in the field emission behavior of the carbon nanotubes grown on Inconel substrates with variation in the process parameters using MPECVD process. It is seen that with the proper

substrate pre-conditioning (heat-treatment) and by using microwave attenuator on the top of the growing surface, it is possible to achieve high FEF ( $\sim 6740$ ) at a low turn on electric field of ( $\sim 0.65$  V). The reasons for such enhanced field emission current density and FEF have been discussed. It is shown that the presence of clearer grain boundaries that are created during heat-treatment helps in formation of transition metal nanoparticles more efficiently. Further, it is concluded that incorporation of the microwave attenuator on the growing surface promotes the higher growth rate, higher aspect ratio and favorable defects in CNTs. This entire work has already been published in Carbon [54].

#### **References:**

1. S. Iijima, Nature 354 (1991) 56–58.
2. M.S. Dresselhaus, G. Dresselhaus, P. Avouris (Eds.), Springer, Heidelberg, 2001.
3. P. Jarillo-Herrero, J.A. Van Dam, L.P. Kouwenhoven, Nature 439 (2006) 953.
4. S. Fan, M.G. Chapline, N.R. Franklin, T.W. Tombler, A.M. Cassell, H. Dai Fan, Science 283 (1999) 512.
5. K.B.K. Teo, E. Minoux, L. Hudanski, F. Peauger, J.P. Schnell, L. Gangloff et al., Nature 437 (2005) 968.
6. T.T. Baby, R.B. Rakhi, N. Ravi, S. Ramaprabhu, J. Nanosci. Nanotech. 12 (2012) 6718.
7. J. Zhang, G. Yang, Y. Cheng, B. Gao, Q. Qiu, Y.Z. Lee et al. Appl. Phys. Lett. 86 (2005) 184104.

8. C. Chien-Chao, T. Tsung-Yen, T. Nyan-Hwa, *Nanotechnology* 17 (2006), 2840.
9. W. Wei, J. Kaili, W. Yang, L. Peng, L. Kai, Z. Lina et al. *Appl. Phys. Lett.* 89 (2006) 203112.
10. F. Jin, Y. Liu, C.M. Day, S.A. Little, *Carbon* 45 (2007) 587.
11. A. Wadhawan, R.E. Stallcup II, J.M. Perez, *Appl. Phys. Lett.* 78 (2001) 108.
12. M. Khazaei, Y. Kawazoe, *Surf. Sci.* 601 (2007) 1501.
13. S. Talapatra, S. Kar, S.K. Pal, R. Vajtai, L. Ci, P. Victor et al., *Nature Nanotech.* 1 (2006) 112.
14. W. Yi, Q. Yang, *Diam. Rel. Mat.* 19 (2010) 870.
15. W. Yi, Q. Yang, *Diam. Rel. Mat.* 19 (2010) 923.
16. M. Meyyappan, L. Delzeit, A. Cassel, D. Hash, *Plasma Sources Sci. Tech.* 12 (2003) 205.
17. S. Sugimoto, Y. Matsuda, H. Mori, J. *Plasma Fusion Res. Ser.* 8 (2009) 522.
18. M. Hirakawa, S. Sonoda, C. Tanaka, H. Murakami, H. Yamakawa, *App. Surf. Sci.* 169-170 (2001) 662.
19. F. Lu, J. Ting, *Acta Materialia* 61 (2013) 2148.
20. W. Yi, Q. Yang, *Appl. Phys. A* 98 (2010) 659.
21. Y.S. Li, A. Hirose, *App. Surf. Sci.* 255 (2008) 2251.
22. L. Gao, A. Peng, Z.Y. Wang, H. Zhang, Z. Shi, Z. Gu et al. *Sol. State Comm.* 146 (2008) 380.
23. Q. Yang, Y. Tang, S.L. Yang, Y.S. Li, A. Hirose, *Carbon* 46 (2008) 589.
24. C. Masarapu, B. Wei, *Langmuir* 23 (2007) 9046.
25. C.E. Baddour, F. Fadlallah, D. Nasuhoglu, R. Mitra, L. Vandsburger, J. Meunier, *Carbon* 47 (2008) 313.

26. F. Lu, K. Liao, J. Ting, J. Electrochem. Soc. 159 (2012) K50.
27. J. Ting, W. Lin, Nanotechnology, 20 (2009) 025608.
28. S. Sridhar, L. Ge, C. S. Tiwary, A. C. Hart, S. Ozden, K. Kalaga et al. ACS App. Mater. Int. 6 (2014) 1986.
29. E. Shin, G. Jeong, Cur. App. Phys. 14 (2014) 8.
30. J.J Kai, C.H. Tsai, T.A. Huang, M.N. Liu, Metal. Transac. A 20A (1989) 1077.
31. M.S. Dresselhaus, G. Dresselhaus, R. Saito, A. Jorio, Phys. Rep. 409 (2005) 47.
32. L.M. Malard, M.A. Pimenta, G. Dresselhaus, M.S. Dresselhaus, Phys. Rep. 473 (2009) 51.
33. L. Bokobza, J. Zhang, eXpress Polymer let. 6 (2012) 601.
34. F. Tunistra, J.L. Koenig, J. Chem. Phys 53 (1970) 1126.
35. E.F. Antunes, A.O. Lobo, E.J. Corat, V.J. Trava-Airoldi, Carbon 45 (2007) 913.
36. S. B. Cronin, A. K. Swan, M. S. Unlu, B. B. Goldberg, M. S. Dresselhaus, M. Tinkham, Phys Rev. Letts. 93 (2004) 167401.
37. N.J. Everall, J. Lumsdon, Carbon 29 (1991) 133.
38. H. Kagi, I. Tsuchida, M. Wakatsuki, K. Takahashi, N. Kamimura, K. Iuchi et al. Geochimica et Cosmochimica Acta, 58 (1994) 3527.
39. K. Hii, R.R. Vallance, S.B. Chikkamaranahalli, M.P. Mengüç, A.M. Rao, J. Vac. Sci. Technol. B 24 (2006) 1081.
40. M. Kumari, S. Gautam, P.V. Shah, S. Pal, U.S. Ojha, A. Kumar et al. App. Phys. Lett. 101 (2012) 123116.
41. R.P. Gao, Z. Pan, Z. Wang, Appl. Phys. Lett. 78 (2001) 1757.
42. H. Kimura, B. Zhao, D.N. Futaba, T. Yamada, H. Kurachi, S. Uemura et al. APL Mat. 1 (2013) 032101.

43. J.S. Suh, K.S. Jeong, J.S. Lee, I. Han, Appl. Phys. Lett. 80 (2002) 2932.
44. L. Nilsson, O. Groening, C. Emmenegger, O. Kuettel, E. Schaller, L. Schlapbach et al. Appl. Phys. Lett. 76 (2000) 2071.
45. S.C. Lim, J.H. Jang, D.J. Bae, G.H. Han, S. Lee, I. Yeo et al. Appl. Phys. Lett. 95 (2009) 264103.
46. M. Manda, D. Jacobson, IEEE transact. Plas. Sci. 6 (1978) 200.
47. M. Wilde, I. Beauport, F. Stuhl, K. Al-Shamery, H.-J. Freund, Phys. Rev. B, 59 (1999) 13401.
48. W. Weiss, W. Ranke, Prog. Surf. Sci. 70 (2002) 1.
49. V. Kaushik, H. Sharma, A. K. Shukla, V. D. Vankar, AIP Conf. Proc. 1451, (2012)148.
50. S.K. Srivastava, V.D. Vankar, D.V. Sridhar Rao, V. Kumar, Thin Solid Films 515 (2006) 1851.
51. B. Padya, D. Kalita, P.K. Jain, G. Padmanabham, M. Ravi, K.S. Bhat, Appl. Nanosci. 2 (2012) 253.
52. F.Ding, K. Bolton, A. Rosèn, J. Elec. Mat. 35 (2006) 207.
53. M.H. Al-Saleh, U. Sundararaj, Carbon 47 (2009) 1738.
54. R.Kar, S.G. Sarkar, C.B. Basak, A. Patsha, S. Dhara, C. Ghosh et al. Carbon 94 (2015) 256.

## **Chapter 5**

### **An Investigation on the Co-deposition Mechanism of Different Carbon Nanostructures by MPECVD Method**

#### **5.1. Introduction**

Different forms and allotropes of carbon have been in use for different purposes since a long time. While diamond is most popular for its gem value, graphite is mostly used as pencil-tip, dry lubricant for machinery and as a conducting material. Laboratory grown synthetic diamond has many desirable properties such as high mechanical hardness, thermal conductivity, electrical resistivity, chemical inertness and broad optical transparency. Several investigations have been reported on the potential and actual applications of poly, nano and single crystal diamond films [1-5]. Apart from diamond, present day interest in nanotechnology has also lead to the popularity of different graphitic carbon nanostructures due to possibilities of their exciting applications. Carbon nanotube (CNT) and graphene nanowall (GNW) are two such nanostructures. Introduction of these two nanostructures have already been given in chapter 1 (section 1.2), chapter 3 (section 3.1) and chapter 4 (section 4.1). For completeness and making this chapter stand alone, brief outline and their importance is mentioned in short.

Since the discovery of CNTs in 1991 it has been given the status of another allotrope of carbon. CNTs are being projected for different applications nowadays in diverse fields ranging from electronics to medicine [6-9]. Due to their excellent electron emission properties CNTs have a strong potential application as a cold cathode [10, 11]. GNW which is sometimes also called carbon nanowall (CNW) is a



relatively newer nanostructure compared to more famous CNT is also less explored. Presently, available data on GNW has shown that it can be used as a good catalyst support structure for fuel cell [12], and also as the negative electrode for lithium ion battery [13]. Moreover, its field-emission capabilities are also comparable to that of CNT [14, 15].

MPECVD is a popular technique for depositing all carbon based structures. It is also well known fact that the possible operation of microwave plasma in comparatively higher operating pressure regime (up to even 100 Torr) allows deposition of crystalline diamond using this method. In fact, microwave plasma CVD is almost tailor made for diamond deposition as it offers a higher operating pressure and temperature regime with good plasma density compared to other plasma CVD methods [16-18]. Apart from growing diamond, microwave plasma has also been used routinely to deposit CNT and GNW. But, deposition of sp<sup>3</sup> hybridized diamond and sp<sup>2</sup> hybridized graphitic nanostructures like CNT and GNW occur in different operational regimes [19]. The basic reason behind this is the deposition rates of sp<sup>2</sup> hybridized graphitic structures are much higher than that of sp<sup>3</sup> hybridized diamond. So, for deposition of diamond, the preferred operational regime is one where etching rate of sp<sup>2</sup> hybridized carbon is much more than sp<sup>3</sup> hybridized carbon. The technique normally is to force more H<sub>2</sub> inside plasma so that nascent H can etch graphitic structures while nucleated and chemically inert diamond seeds remain almost intact [1,20, 21]. The duration of deposition is also long and sometimes goes beyond 10 hours. For deposition of graphitic nanostructures like CNT or GNW one wants a controlled way to deposit sp<sup>2</sup> hybridized graphitic nanostructures on the substrate. In this case, a higher amount of carbon containing precursor as compared to diamond

deposition is fed into the plasma CVD chamber at a pressure which is almost one order of magnitude less than that for diamond deposition. The deposition time normally is much less when compared with former.

Recently, a lot of work has been reported on the deposition methods and basic properties of CNT and nanocrystalline diamond (NCD) based composite materials to establish a new class of nano composites which can have superior physical properties than either CNT or diamond. Terranova et al. [22] showed one-step synthesis method of CNTs coated with NCD by modified CVD method and Fernandes et al. [23] then showed simultaneous synthesis of CNT/NCD by MPCVD. Apart from this, Shankar et al. [24] showed the possibility of nanodiamond/ CNT formation by hot filament CVD (HFCVD) using commercially produced CNTs and Takagi et al. [25] showed that it is possible to grow CNT from diamond. It has previously been shown that heat treated nano-diamond particles can help in the growth of CNTs and CNTs can also nucleate diamond under specific conditions [25, 26]. Very recently Kumaran et al. [27] have used HFCVD to grow isolated diamond particles, continuous diamond films and CNT films on unseeded, seeded and catalysts pre-treated substrates, respectively.

All the above reports discuss co-deposition of two different kinds of carbon nanostructures on the same substrate but our interest remains in the co-deposition of two different types of nanostructures in a single experiment on two different substrates so that mixing of different nanostructures does not occur. These types of reports are very limited in number. One available work by Yang et al. [28] shows that co-deposition of  $sp^3$  hybridized diamond and  $sp^2$  hybridized CNT is possible in a single experiment. During their experiment they could deposit diamond thin film on Si substrate while CNTs were deposited on Inconel which was placed 53 mm below the

Si substrate, at bottom plate of the substrate holder. However, to facilitate growth of diamond they kept an additional polycrystalline graphite sheet on the substrate holder so that transitional hydrocarbon radicals could be formed due to hydrogen etching of graphite. Also, they added a negative bias to the substrate without which CNTs could not be grown. Apart from this, there is another work of Ali et al. [19] which reports about simultaneous growth of graphite and diamond thin films by HFCVD. They deposited needle like nanostructured graphite and diamond thin film at the different locations of the reactor and also saw transformation of diamond into graphite during the experiment due to restricted presence of atomic hydrogen in the reaction.

Our efforts have been focussed to understand the process and mechanism of the co-deposition in a PECVD reactor where same experimental parameter leads to deposition of different type of nanostructures. Knowing the actual role of plasma, effect of substrate choice and location is expected to allow better control in co-deposition saving process time and energy consumption. This kind of knowledge significantly accelerates and expands industrial applications of different carbon nanostructures.

In the present work, we have shown that it is possible to simultaneously deposit sp<sup>3</sup> and sp<sup>2</sup> hybridized carbon structures by identifying an operating window that allows co-deposition of these two structures. Apart from these we have also been able to deposit two different graphitic nanostructures like GNW and CNT together in a single experiment by appropriately tuning experimental parameters. The detailed mechanism involving co-deposition of sp<sup>3</sup> and different sp<sup>2</sup> hybridized nanostructures has been investigated through a series of experiments. During deposition plasma has been characterized by optical emission spectroscopy (OES) and the deposited material

have been characterized by scanning electron microscopy (SEM), high resolution transmission electron microscopy (HRTEM), micro-Raman spectroscopy and Raman imaging. These characterization results support our claim of co-deposition. It is seen that the choice of the substrate inside the vacuum chamber and its location during deposition play major roles in deciding which micro/nano-structure is deposited on the substrate. Characterization results revealed that combination of substrate surface preparation, carbon precursor feeding rate and deposition time are the deciding factors for growth of a particular type of nanostructure. Raman spectroscopic results showed that GNWs behave like nano form of turbostratic graphite and it is seen that they can be deposited even when the plasma is highly perturbed and non-uniform. Optical emission spectroscopy results indicated that an increase in the intensity of C2 swan band increases deposition of graphitic nanostructures but decreases the required control for uniform deposition. The role of plasma sheath in co-deposition is explained with the help of a schematic model.

## **5.2. Experimental**

The microwave plasma CVD facility used here for the experiments has already been described in section 2.2 and a photograph of the original system also shown in the section 4.2. A series of experiments were conducted using this facility to determine conditions for the co-deposition. All the experimental parameters and findings are tabulated in Table 5.1 for easy understanding. Experiments 1 and 4-7 were conducted by keeping Inconel as the substrate and putting a Si piece on top of it as microwave attenuator. The reason for using this particular arrangement is described in detail in the previous chapter. In short, this arrangement helps in transmitting only ~ 2 % of microwave power to the metal substrate reducing the chance of microwave

reflection from metal to a great extent. Figure 5.1 shows the actual photograph of this arrangement inside the PECVD reactor during an experiment. From the photograph it is seen that Si attenuator and Inconel substrate both have become red hot during the experiment and  $H_2-C_2H_2$  plasma is seen over them. While CNTs have always been deposited on Inconel during experiments 1, and 4-7, depending on the gas composition, plasma temperature and condition of Si surface either no deposition occurred or GNWs / NCD could be deposited on the Si attenuator. Experiments 2 and 3 were conducted for diamond deposition by keeping only a Si piece as the substrate inside the reactor. As often reported, random scratches filled with diamond particles is the primary requirement to initiate diamond nucleation [21, 30, 31]. For experiments 2 and 3, Si substrates were prepared by first scratching it with a 320 grade emery paper. After scratching marks become visible under optical microscope, Si substrates were ultrasonicated for 10 minutes in a solution of methanol mixed with 25  $\mu m$  diamond powder. After that substrates were loaded in the PECVD chamber for these experiments. For experiments 1 and 5 & 6 Si attenuators were scratched and they were prepared in similar manner as experiment 2 and 3 but for experiment 4, a plane Si piece without any scratching was used as the attenuator. Experiment 7 was conducted by keeping the experimental parameters same as experiment 6 but the Si attenuator used in experiment 5 was reused in this case as the attenuator.

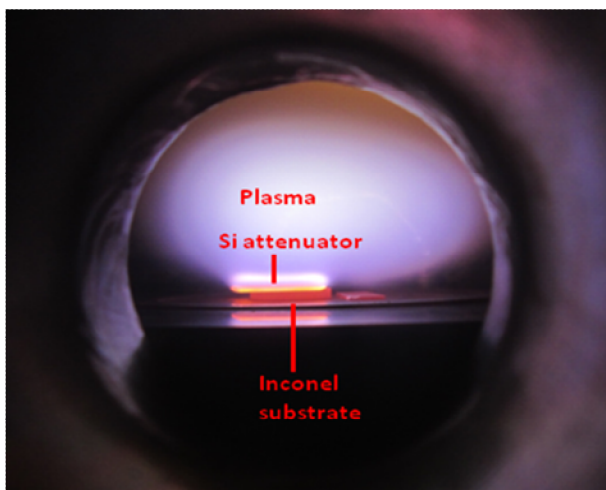


**Figure 5.1:** Actual photograph of experimental condition for CNT deposition inside MPECVD reactor.

Experiment 1 was conducted as the standalone experiment for growing CNTs on Inconel while experiments 2 & 3 were conducted as the standalone experiments for depositing diamond on the Si substrates. Experiments 4 to 6 were conducted to check the possibility of co-deposition of two different carbon allotropes in the same experiment. During experiments plasma was characterized by an Andor Mechelle optical emission spectroscopy (OES) unit fitted with ikon-M CCD camera. The deposited coatings were characterized using various characterization methods. A Carl Zeiss EVO 40 scanning electron microscope (SEM) and Carl Zeiss Auriga field-emission SEM (FESEM) were used to investigate the morphology of the deposited films. For further investigation of the-grown structures a FEI Tecnai G2 F30 high resolution transmission electron microscope (HRTEM) with Gatan image filter facility was used. Reinshaw inVia micro-Raman analyzer (514.5 nm Ar ion laser) with Raman imaging facility was used for Raman imaging of the sample. Another 532 nm He-Ne laser based micro-Raman spectrometer was also used for determining defects and obtaining bonding information of deposited structures.

**Table 5.1:** Details of experiments conducted for the co-deposition of different carbon structures.

Ex pt. No.	Gas mixture	Microwave power (Kw)	Operating pressure (Torr)	Substrate details	Attenuator details	Depositi on time (mins.)	Final outcome
1.	100 SCCM H <sub>2</sub> + 20 SCCM C <sub>2</sub> H <sub>2</sub>	1	~ 45-50	Inconel substrate at ~ 900°C.	Scratched Si piece at ~ 1000°C.	20	CNTs deposited on Inconel substrate. Almost nothing deposited on Si attenuator.
2.	95 SCCM H <sub>2</sub> +5 SCCM Ar + 2 SCCM C <sub>2</sub> H <sub>2</sub>	1.2	~ 75-80	Si substrate at ~ 950°C.	Not applicable.	300	A mixture of NCD and micro- crystalline diamond deposited on Si substrate.
3.	98 SCCM	1.5	~ 115- 120	Si substrate	Not applicable.	360	Diamond deposited

	H <sub>2</sub> + 2 SCCM C <sub>2</sub> H <sub>2</sub>			at ~ 1000°C.			on Si substrate.
4.	75 SCCM H <sub>2</sub> + 25 SCCM N <sub>2</sub> + 20 SCCM C <sub>2</sub> H <sub>2</sub>	1	~ 45-50	Inconel substrate at ~ 950°C.	Si piece without scratching ~ 1000- 1200°C.	60	CNTs deposited on Inconel substrate. GNW deposited on Si attenuator.
5.	75 SCCM H <sub>2</sub> + 25 SCCM N <sub>2</sub> + 20 SCCM C <sub>2</sub> H <sub>2</sub>	1	~ 45-50	Inconel substrate at ~ 900°C.	Scratched Si piece at ~ 1000°C.	150	CNTs deposited on Inconel substrate. GNW deposited on Si attenuator.
6.	75 SCCM H <sub>2</sub> + 25 SCCM N <sub>2</sub> + 5	1	~ 45-50	Inconel substrate at ~ 900°C.	Scratched Si piece at ~ 1000°C.	150	CNTs deposited on Inconel substrate. NCD



	SCCM $C_2H_2$						deposited on Si attenuator.
7.	75 SCCM $H_2$ + 25 SCCM $N_2$ + 5 SCCM $C_2H_2$	1	~ 45-50	Inconel substrate at ~ 900°C.	Si attenuator used in expt. 5 at ~ 1000°C.	150	CNTs deposited on Inconel substrate. NCD deposited on Si attenuator.

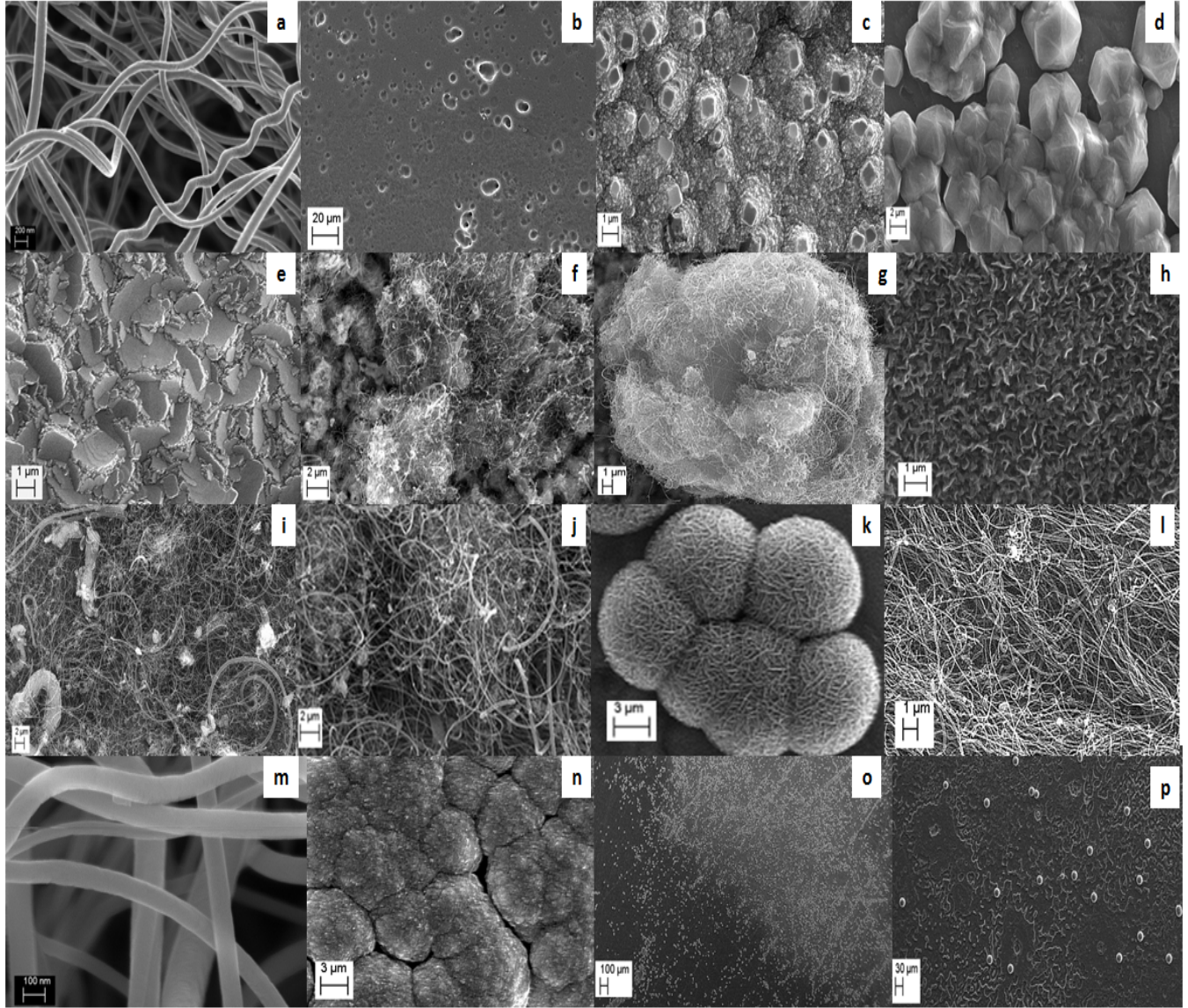
### 5.3. Characterization results

Figure 5.2 shows the detailed SEM result panel obtained for all the samples mentioned in the previous section. Figure 5.2a shows the FESEM image of the CNTs deposited in the 1<sup>st</sup> experiment. Figure 5.2b shows the SEM image of the Si attenuator on that sample. From the image it is seen that the attenuator contains  $\mu m$  sized holes and pits. These are the result of scratching the Si piece with emery paper. However, no deposition is observed in this case. Figures 5.2c shows SEM image of deposited diamond film on Si substrates for experiment 2. It is seen that introduction of Ar in the gas mixture during diamond deposition facilitates growth of diamond cubic crystals on the substrate. It confirms that 100 micro-crystalline diamond (MCD) phases had started to grow from cauliflower like NCD phases [32]. From the image it is clear that the conversion from NCD to MCD was incomplete in the process. Earlier,

investigations showed that Ar enhances the rate of deposition of diamond by helping in the creation of  $C_2$  dimers which are normally thought to play an important role in the deposition [33]. But, it has also been observed that larger amount of Ar in the plasma results in formation of NCD from polycrystalline phase [33, 34]. Figures 5.2d and 5.2e show the image of diamond films deposited without addition of Ar in plasma. It shows formation of octahedral MCD in some places while defective MCD crystals are also seen in some regions (Figure 5.2e). Figures 5.2f-5.2h show the SEM image of coatings deposited in experiment 4. While Figures 5.2f and 5.2g shows the CNT deposition on the Inconel substrate, Figure 5.2h shows GNW deposited on the Si attenuator. It is seen that as the deposition time is increased from 20 to 60 minutes in this experiment compared to experiment 1, the control on deposition of CNT is lost and large CNT balls get deposited with long CNTs in random places on the substrate. Figures 5.2i-5.2k show SEM images of the deposited coatings in experiment 5. Comparing figures 5.2f & 5.2g with 5.2i & 5.2j, one can easily see that after increasing time from 60 to 150 minutes CNTs have become longer and denser. However, still the amount of control on the quality of CNTs is less as seen from Figure 5.2i. It is clearly seen that micron sized tubes; amorphous carbon and other unwanted structures also got deposited with CNTs in this case. Figure 5.2k shows deposition occurred on the attenuator in this experiment. It seems that GNWs have been deposited in the shape of graphitic balls where layers can clearly be seen from the image. It is to be noted that apart from the deposition time there are two more differences between experiment 4 and 5. The attenuator for the experiment 5 was scratched in quest to study the possibility of diamond deposition unlike the attenuator in experiment 4. Also, the temperature of the attenuator reached ~200 degrees more in

some places in the experiment 4. The temperature difference occurred in experiment 4 as a larger attenuator was used which was almost equal in dimension to the plasma and it extended upto the edges of the plasma ball. The actual photograph taken during experiment 4 is shown in Figure 5.3. Comparing Figures 5.1 and 5.3, it is seen that as the attenuator is comparable to the spread of the plasma, it modifies the normal oval shaped plasma ball (Figure 5.1) into an elongated and deformed ellipsoid (Figure 5.3). The modified plasma for the case of experiment 4 was not as uniform as the case of other five experiments and this plasma caused non-uniform heating of the attenuator. So, the CNTs obtained in experiment 4 could have also been affected by this change in the plasma. Figures 5.2l-5.2n show the SEM images obtained for experiment 6. Here, first two images shows that best quality CNTs could be deposited in this case. It becomes obvious that by reducing the  $C_2H_2$  flow from experiment 4 and 5 to experiment 6, gives a much better control on the deposition. CNTs deposited here are very long (more than 20 microns) and defect free (Figure 5.2m). Figure 5.2n shows the SEM images of the deposited coating on the attenuator in this case. From the SEM images it is seen that cauliflower shaped NCD could be deposited in this case. Figures 5.2o and 5.2p shows deposition that occurred on Si attenuator used in experiment 7. It is seen from Figure 5.2o that deposition of the diamonds are following the tracks provided by scratches on the Si surfaces which is normal for diamond deposition. But, Figure 5.2p gives interesting information about the co-deposition. It is seen from the image that during the co-deposition experiment, graphitic GNWs deposited in experiment 5 have been etched away in H environment but diamond particles remained stuck on the attenuator and they remain unaffected by plasma. It seems from

the figure that during etching coating-substrate interface between GNWs and Si got damaged. This last experiment ensures repeatability of the co-deposition experiments.



**Figure 5.2:** (a) FESEM image of CNTs deposited in experiment 1, (b) SEM image of the Si attenuator used in the experiment 1, (c) SEM image of the NCD and MCD deposited in the experiment 2, (d) SEM image of octahedral diamond crystals deposited in experiment 3, (e) SEM image of the defective MCD crystals deposited in the experiment 3, (f) SEM image of the CNTs deposited in the experiment 4, (g) SEM

image of the CNTs deposited in the ball shape in experiment 4, **(h)** SEM image of the GNWs deposited on the Si attenuator in the experiment 4, **(i)** SEM image of the CNTs deposited in the experiment 5 along with micron sized larger diameter tubes and thicker bunches, **(j)** magnified SEM image of the CNTs deposited in the experiment 5, **(k)** SEM image of GNWs deposited in ball shape on the Si attenuator in the experiment 5, **(l)** SEM image of the CNTs deposited in the experiment 6, **(m)** FESEM image of the CNTs deposited in the experiment 6 showing formation of defect free CNTs, **(n)** SEM images of the NCDs deposited on the Si attenuator in the experiment 6, **(o)** SEM image of the Si attenuator showing the diamond formation along the scratch marked tracks, **(p)** SEM image of the reused Si attenuator previously used in the experiment 5. It shows removal of ball shaped GNWs and presence of diamond particles on it.

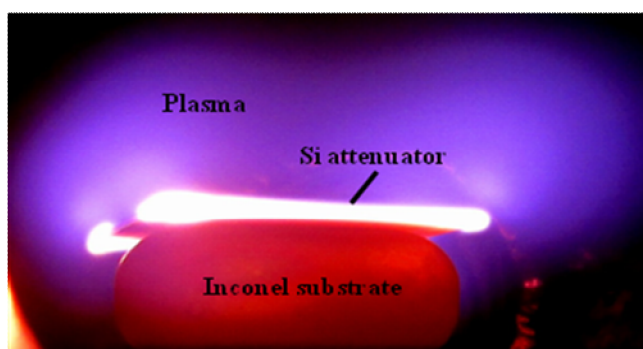


**Figure 5.3:** Actual photograph of the plasma condition inside the reactor in experiment 4.

Figure 5.4 shows the HRTEM images of CNTs and GNWs deposited during experiments 5 and 6. Figure 5.4a shows the HRTEM image of the CNTs deposited in experiment 5. From the image, large numbers of black spots are seen to be present inside the CNT core. STEM-XEDS analysis performed earlier on this type of black spots revealed that these nano particles which got trapped inside the CNT core are

nano-fragments of Inconel itself and no particular metal is favored in the process [11]. It has been seen that due to etching by H-plasma nano sized particles of Inconel themselves get trapped inside the tubes during the growth. Figure 5.4b shows the HRTEM image from experiment 6. It is seen that with lower feeding rate of  $C_2H_2$  there is almost no inclusion of Inconel particles inside CNTs. It is also seen that control on the growth is much more enhanced in this case. Figure 5.4c shows the image of bamboo-like defects produced within the CNTs. This defect was produced both in experiments 5 and 6 signifying high growth rates of CNTs in both the cases [37, 38]. Figure 5.4d shows a typical low resolution image of GNWs deposited in these experiments. From the figure only ribbon-like structures are seen and to obtain further information HRTEM is performed. Figures 5.4e and 5.4f show the HRTEM images of GNWs produced during experiment 4 and 5 respectively. Both the images show the presence of graphene layers in the sample. As expected, there is no tubular shape present and only stacking of graphene layers have been observed in both the cases. HRTEM images confirm the formation of GNWs on the Si attenuator during the course of these experiments.



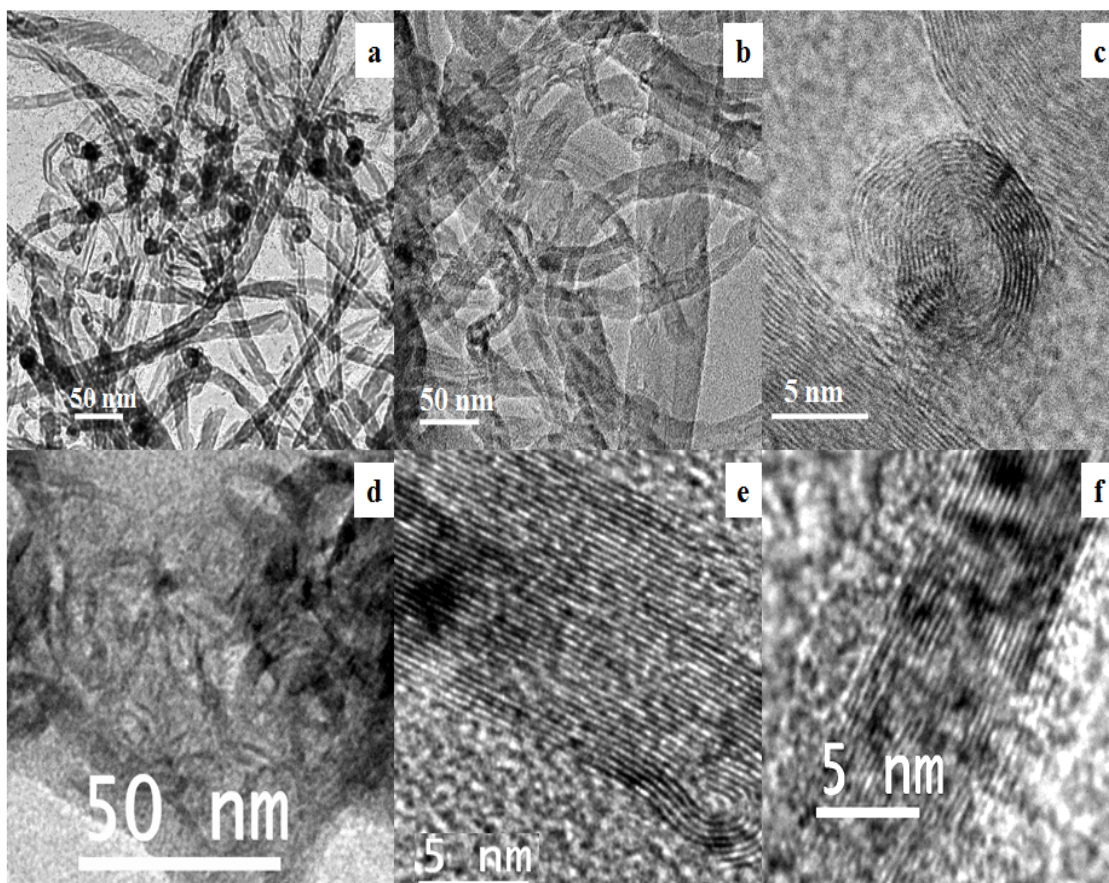


**Figure 5.4:** (a) HRTEM image of the CNTs deposited in experiment 5, (b) HRTEM image of CNTs deposited in experiment 6, (c) HRTEM image of typical bamboo-like defects seen inside the tubes in experiment 5 and 6, (d) Typical TEM image of GNWs deposited in experiment 4 and 5, (e) HRTEM image of GNWs deposited in experiment 4, (f) HRTEM image of GNWs deposited in experiment 5.

Figure 5.5 shows the micro-Raman spectra taken on the deposited coatings. Figure 5.5a shows the typical Raman spectrum taken of diamond sample deposited here. The figure shows the emergence of the diamond peak at  $\sim 1333 \text{ cm}^{-1}$ . Graphitic contribution is also seen in the form of a broad band which is normally the case when MCD or NCD is formed by CVD/PECVD method [23, 27, 37]. Figures 5.5b and 5.5c show the micro-Raman spectra of the GNWs deposited on the attenuator during experiment 4. The spectra are in agreement with observations as discussed by many

authors for GNWs/CNWs [38, 39]. The spectra show presence of D, G, D' and G' bands. Figures 5.5d and 5.5e show the micro-Raman spectra of the ball like GNW structures deposited on the Si attenuator in the experiment 5. Similar to the GNW Raman spectrum presence of D, G, D' and G' is seen in this case also. The first Raman band present in Figures 5.5b and 5.5d  $\sim 1350 \text{ cm}^{-1}$  is called D band [40]. In Figures 5.5b and 5.5d the band around  $1580 \text{ cm}^{-1}$  is called G band and it is the only band which originates from the first order Raman scattering [41]. Also, this peak in both these cases has a small shoulder peak called D' which occurs due to second order Raman scattering around  $1620 \text{ cm}^{-1}$ . This peak is observed in some disordered graphitic carbon structures [39] including graphene [41]. This peak cannot occur under defect free conditions and it is observed when there are more chances of defect generation in graphene sheets.

Figure 5.5c and 5.5e show another intense band around  $2700 \text{ cm}^{-1}$ . This band is normally called G' [42-44] and it arises from a two-phonon, intervalley, second-order process. A monolayer graphene exhibits a single, intense Lorentzian peak due to double and triple Raman scattering. For bilayer graphene, four Lorentzian peaks can be fitted due to the splitting of  $\pi$  electronic structure of graphene. With an increase in number of layers, the number of double resonance process also increases and eventually the shape converges to graphite with only two Lorentzian peaks present [41, 43]. For turbostratic graphite, in which the stacking of the graphene layers is rotationally random with respect to one another G' band can be fitted with a single Lorentzian peak just as monolayer graphene but with a larger FWHM. For monolayer graphene, FWHM is around  $24 \text{ cm}^{-1}$  unlike  $45\text{-}70 \text{ cm}^{-1}$  for turbostratic graphite [43]. Table 5.2 shows the detailed Raman spectroscopic data obtained for GNW samples



from experiment 4 and 5. Defects produced in these nanostructures have been quantified and presented by  $I_D/I_G$  ratio. It is seen that Experiment 5 has produced more defective GNWs. From the table it is also seen that,  $G'$  peak in both the cases has FWHM  $\sim 70\text{-}75\text{ cm}^{-1}$  and it can be fitted with a single Lorentzian peak in both the cases. The nature of this peak is similar to the  $G'$  band observed in the turbostratic graphite. It suggests that GNWs are formed due to stacking of graphene sheets without having any favorable orientations and they can be viewed as turbostratic graphite structure in nanoscale.

Figure 5.5f shows the Raman spectrum of the Si attenuator from experiment 6. Presence of peak at  $1333\text{ cm}^{-1}$  confirms deposition of NCD in this case and graphitic band is quite broad here compared to what was observed in Figure 5.5a. It essentially tells that quality of diamond films deposited in the stand alone experiments was better. To ensure the quality of the diamond deposited in the co-deposition experiment, Raman imaging of the attenuator was also done. During this process isolated large particle consisting of many smaller NCD particles which got deposited on one side of the scratched Si attenuator from experiment 6 was taken for analysis. Analysis of this data provides a measure of what fraction of the particle responds to the diamond characteristic Raman signal of  $1333\text{ cm}^{-1}$  and what fraction is responsible the  $1547\text{ cm}^{-1}$  signal characteristic of the graphite. Figure 5.6 shows the images obtained during this process. Figure 5.6a shows the actual microscopic image of the particle while Figures 5.6b and 5.6c show the Raman imaging spectra taken on the same particle for  $1333\text{ cm}^{-1}$  and  $1547\text{ cm}^{-1}$  band respectively. The vertical axes on the right hand side of these two images show the counts for their respective signals. From the images 5.6b and 5.6c it can be concluded that though the chosen particle is

predominantly in  $sp^3$  hybridized form but there is also incorporation of  $sp^2$  hybridized graphitic form which is highlighted by the large graphitic band in the Figure 5.5f also.

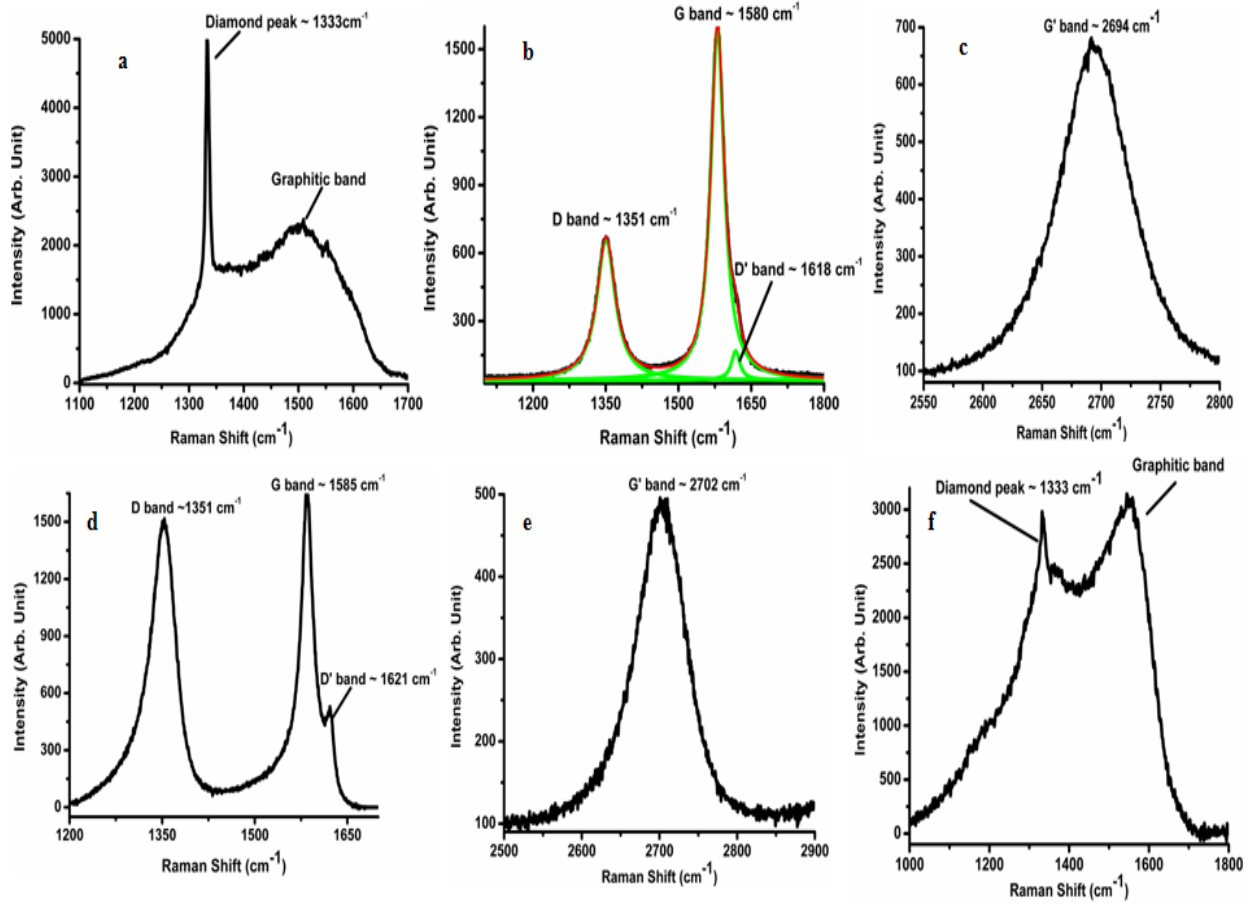


**Figure 5.5:** (a) Typical Raman spectrum of deposited MCD films in experiment 2 and 3, (b) Raman spectrum of GNWs deposited on Si attenuator in experiment 4 between 1100-1800  $cm^{-1}$ , (c) Raman spectrum of GNWs deposited on Si attenuator in experiment 4 between 2500-2800  $cm^{-1}$ , (d) Raman spectrum of GNWs deposited in ball shape on Si attenuator in experiment 5 between 1200-1850  $cm^{-1}$ , (e) Raman spectrum of GNWs deposited in ball shape on Si attenuator in experiment 5 between 2500-2900  $cm^{-1}$ , (f) Raman spectrum of NCD films deposited on Si attenuator in experiment 6.

**Table 5.2:** Raman spectroscopic measurement data of GNW samples.

Expt. No	Raman shift ( $\text{cm}^{-1}$ ) and FWHM				$I_D/I_G$
	D band (FWHM)	G band (FWHM)	D' band (FWHM)	G' band (FWHM)	
4	1350.61 (45.63)	1580.39 (33.69)	1617.78 (21.19)	2694.17 (68.74)	0.54
5	1350.79 (48.60)	1584.58 (26.16)	1621.38 (8.85)	2701.65 (74.14)	1.83

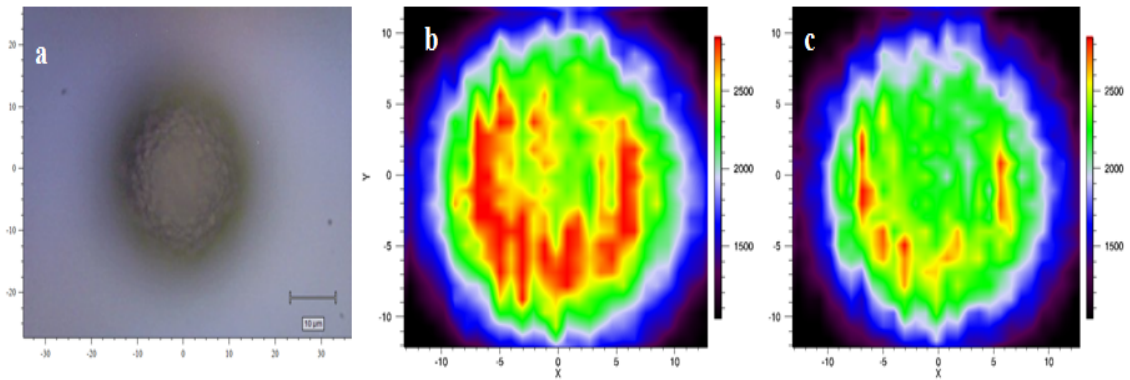


**Figure 5.6:** (a) Optical microscopic image of the particle taken for Raman imaging, (b) Raman imaging of the particle for  $1333 \text{ cm}^{-1}$ , (c) Raman imaging of the particle with  $1547 \text{ cm}^{-1}$ .

To understand the deposition mechanism of different carbon based structures in a single experiment, OES of the plasma was performed during experiment 5 and 6. Figures 5.7a and 5.7b show the OES spectra of the experiments 5 and 6 respectively. Both the figures show the prominent presence of CN and H $\alpha$  bands. This is natural as dissociated C<sub>2</sub>H<sub>2</sub> and N<sub>2</sub> inside plasma form CN band while dissociated H<sub>2</sub> gives rise to H $\alpha$ . The major differences between the two are the clear presence of C<sub>2</sub> band and a

decreased integrated intensity ratio of CN: H $\alpha$  in Figure 5.7a as compared to Figure 5.7b. It suggests that decreased feeding rate of C<sub>2</sub>H<sub>2</sub> inside the reactor changes plasma chemistry making it easier for C to form CN band with dissociated N<sub>2</sub> rather than formation of C<sub>2</sub> Swan bands as carbon supply diminishes.

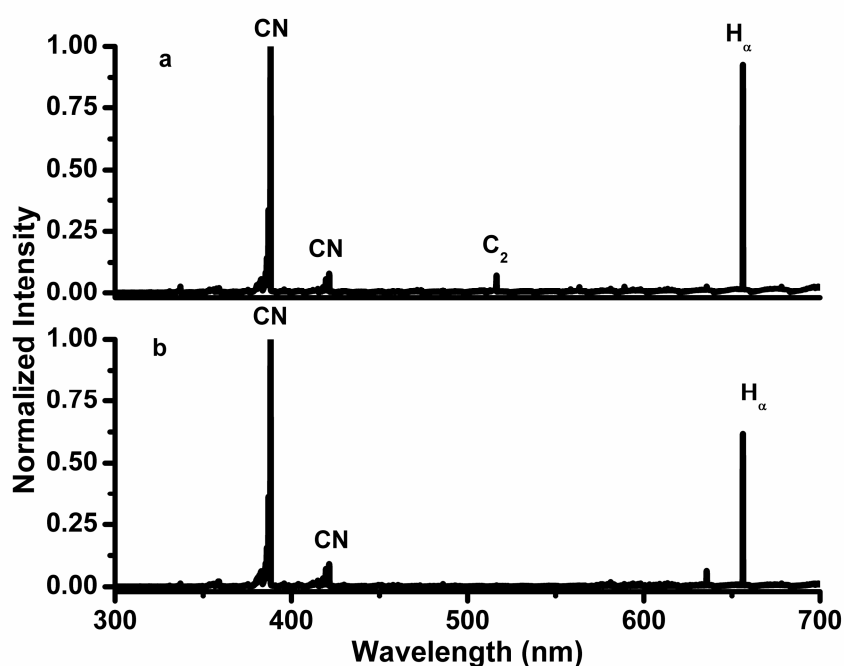


**Figure 5.7:** (a) OES spectrum of the plasma taken during experiment 5, (b) OES spectrum of the plasma taken during experiment 6.

#### 5.4. Discussion

Figures 2-6 from the preceding section conclusively proves that it is possible to deposit different types of carbon nanostructures in a single experiment at different locations in a PECVD chamber. OES spectra shown in Figure 5.7 reveal the situation inside plasma during co-deposition experiments. As stated in the previous section it is seen that with decreasing flow of C<sub>2</sub>H<sub>2</sub> inside plasma intensity of CN band increases with respect to C<sub>2</sub> and H $\alpha$ . Decreasing C<sub>2</sub> band intensity indicates lowering of active carbon radical concentration in the plasma. It is also important to note that in

experiments 4 & 5 where  $C_2$  swan band is appreciable, control on the deposition is less. This is observed comes from the SEM images of CNTs in Figures 5.2f, 5.2g (experiment 4) and 5.2i, 5.2j (experiment 5). It is seen that in both of these cases, CNTs have grown with lot of unwanted structures like amorphous soot and bunched tubular growths. It is also seen from these images that in spite of having similar experimental and substrate preparation conditions in both the cases, CNTs deposited in experiment 5 are of better quality. The reason behind this will be discussed later in this section. Again in both these experiments, we could not deposit any type of diamond along with CNTs. Presence of  $C_2$  radical has also been recently observed by Linnik et al. [44] who observed that during diamond deposition increase in  $C_2$  swan band intensity increases non-diamond carbon content in the film. Comparing SEM images with OES spectra and noting the experimental parameters it is seen that co-deposition of two contrasting carbon allotropes like diamond and CNT is only possible when carbon feeding rate is controlled below a certain level in a PECVD system. The effect of the limiting flow rate for a type of deposition system can be correlated to the intensity of  $C_2$  band in OES spectra.

Another interesting fact observed during the exercise is that substrate surface preparation and condition of the plasma over the substrate play major role in deciding which type of carbon nanostructure gets deposited on the substrate. That is the reason why same experimental conditions in experiments 4 and 5 resulted in two different kinds of nanostructures on Si attenuator. It is seen that planar GNWs could be deposited in experiment 4, while spheres of GNWs could be deposited in experiment 5. If one looks carefully into these two experiments, it can be seen that there were differences in the size and surface preparation of the Si attenuator. Si attenuator in

experiment 4 was not scratched with emery paper and also it was about 4 cm x 4 cm in size. In contrast, Si attenuator in experiment 5 was scratched with emery paper to check its feasibility to grow diamond and it has a size of ~2 cm x 2 cm. The change of the attenuator size affects uniformity of the plasma itself. The microwave plasma ball generated during the MPECVD experiments is normally an ellipsoid with major axis of around 5 cm (Figure 5.1) but when the large attenuator was used in the experiment 4 it perturbed the uniformity of the plasma.

The exact situation in experiment 4 can be seen in the Figure 5.3. Here, the large attenuator extends almost upto the region where plasma physically ends and it seems that the plasma gets divided into two brighter lobes with a little dimmer central portion. The sides of the attenuator which had no direct contact with Inconel gets heated up very easily and starts glowing (Figure 5.3) as Si is not a good conductor of heat. The situation is well explained by an exaggerated schematic showing two denser plasma lobes with rarer plasma existing between them (Figure 5.8a). The reason for this behavior of the plasma is the changes in the electric field brought with the introduction of the larger attenuator. It is well known that normally plasma has a constant potential inside called plasma potential without having any electric field present inside it. But near the boundary where plasma slowly ceases to exist electric potential starts gradually decreasing to zero. So, larger attenuator goes upto the extent where potential starts falling. In that zone sharp sides of the attenuator cause some enhancement in the electric field and plasma density increases along the sides of the attenuator. This is the reason for two brighter spherical lobes as seen on the two sides. In central portion the electric field is not modified and hence plasma looks comparatively dimmer in this region. But when a 2x2 cm Si piece is kept as attenuator,

it does not perturb the uniformity of the plasma. Perturbation of plasma is also the reason why the CNTs deposited in experiment 4 (Figures 5.2f, 5.2g) is of inferior quality than those deposited in experiment 5 (Figures 5.2i, 5.2j).

Another schematic in Figure 5.8b shows the situation on the top of Si attenuator where random scratch marks are filled with diamond particles which act as the seed for further growth. Figure 5.8c gives a pictorial depiction of the situation prevailing inside the PECVD chamber during deposition in the presence of the Si attenuator. This schematic can be taken as the general scheme for experiments 4-6. In all these cases, various ions get accelerated towards the Si attenuator after entering plasma sheath due to sheath electric field. For experiment 4, it is beyond doubt that denser plasma has higher number density of charged species which in turn would result in a stronger sheath electric field. So, deposition rate in the two brighter lobes will be higher. This is exactly what is shown in Figure 5.8a suggesting the coating at the two sides would be thicker leaving the central region as a black patch only. This was confirmed experimentally too. The deposited coating in experiment 4 was black and thick at the two edges with a grayish central portion. However, SEM indicated that GNWs were deposited all over the Si attenuator and the color difference only indicated that the deposition rate was quite low in central portion. As abundant diatomic carbon was present in this experiment (visible  $C_2$  band Figure 5.7a), it easily came to the plasma sheath and got deposited on Si. It is well known that diatomic carbon normally aggregates into graphitic deposition and inside plasma medium under the presence of strong sheath electric field ( $\sim 10^4$  V/m), diatomic carbon and carbon ions got deposited on the Si surface in the form of small graphene sheets [44]. Again no external electrical bias was provided on the substrate and hence there will not be

any vertical guiding electric field. Only electric field present would be the sheath electric field. Depending on the experimental condition, this electric field will guide the ions and radicals which enter the sheath to finally be deposited on the substrate surface forming GNW structures.

For experiment 5, the attenuator did not disturb the plasma and the surface of the Si was also laced with diamond particles lodged inside the scratches as shown in Figure 5.8b. In this particular case, the micron sized diamond particles served as a template for carbon based deposition very easily. However, as the feeding rate of carbon was quite high, etching of sp<sup>2</sup> hybridized structures were not enough and we ended up with GNWs on spherical template provided by the diamond particles (Figure 5.2k). The confirmation of this kind of deposition is also evident from the Raman spectroscopic results.

Having analyzed the difference between experiments 4 and 5 it is imperative to look into the experiment 6, where diamond could be deposited on the Si attenuator. From table 5.2, it is seen that the major difference in this case was the lowering of C<sub>2</sub>H<sub>2</sub> flow rate from 20 to 5 SCCM. Naturally, with low carbon precursor feeding rate etching of graphitic carbon by nascent H was more effective and also the diamond particles present on the Si surface helped to initiate nucleation of diamond particles. This is exactly what enabled deposition of diamond particles in this case. From, OES spectra (Figure 5.7), one can conclude that when N<sub>2</sub> is present in the plasma during diamond deposition in MPECVD, intensity of C<sub>2</sub> Swan band has to be very weak for successful deposition. Decomposed precursors will get deposited on the Si attenuator and their nature of formation will depend on the C<sub>2</sub>H<sub>2</sub> flow rate, substrate condition and deposition time.



Now, in all the above experiments CNTs could always be deposited on the Inconel substrate placed below the attenuator. The mechanism of CNT formation in this kind of experimental arrangement has been discussed in detail in our previous work [11]. In short, when carbon based structures are being deposited on the attenuator escaped carbon ions and radicals will also enter the gap between the attenuator and the Inconel. It has been earlier proved with the help of stylus profilometer that this gap is  $\sim 0.7 \mu\text{m}$  [11]. When they are placed within the sheath, the carbon species which enter this  $0.7 \mu\text{m}$  gap cannot escape very easily and sometimes reflected back. Their residence time on the substrate increases, increasing the chance of deposition of carbon based structures (Figure 5.8c). It has to be understood that co-deposition only becomes possible if the attenuator and the top of the Inconel surface is within the plasma sheath, otherwise no deposition can occur.

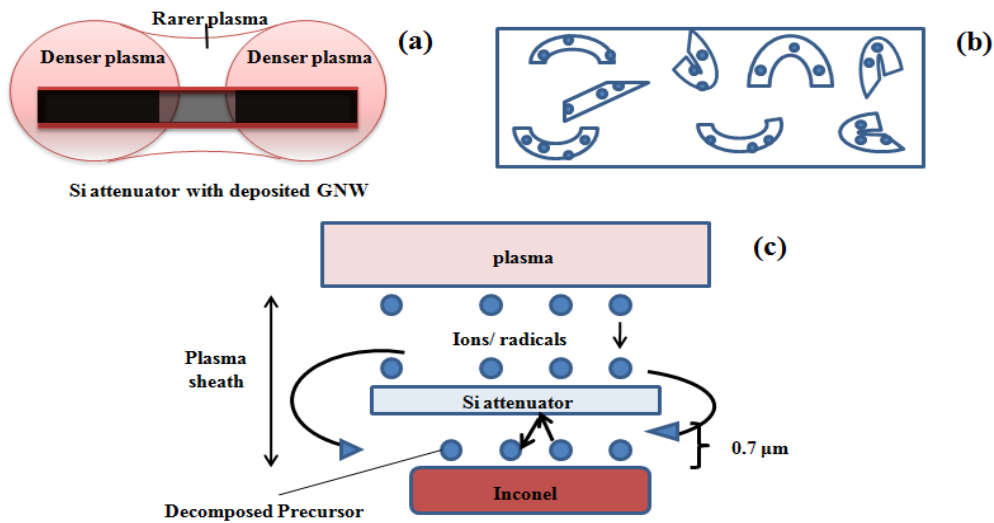


**Figure 5.8:** (a) Schematic representation of the condition of the plasma over the Si attenuator in experiment 4, (b) schematic representation of scratched Si attenuator used in experiments 5 and 6, (c) Schematic of deposition condition inside MPECVD chamber with presence of Si attenuator inside plasma sheath.

It is to be mentioned that in all the co-deposition experiments, the primary attention was always given to the growth of CNTs. Now, if one analyzes the OES spectra (Figure 5.7) from the perspective of CNT deposition by MPECVD then one can also see that, disappearance of  $C_2$  band from the major lines of the OES spectrum gives a better control on CNT deposition. Diatomic carbon always help in increasing deposition rate of carbon based structures but from the SEM images we conclude that this increase comes at the cost of loss of control over the deposition process.

GNW/CNW is basically a discontinuous array of stacked and defective graphene sheets. This very basic graphitic nanostructure can form in PECVD easily even without much control on the experimental scheme. To consolidate this fact another set of experiment was conducted and this time Si attenuator was of a size of  $\sim 5\text{ cm} \times 5\text{ cm}$ . The idea here was to disturb the plasma to a maximum possible extent and study the type of nanostructure gets deposited. The experimental condition was kept identical to experiment 4. Figures 5.9 (a-c) show the actual photograph of plasma during deposition. It is seen that, in this case plasma is disturbed to the extent that four lobes are formed on the four corners of the Si attenuator and plasma is generated surrounding the lobes as electric field also gets a boost at the corners. The temperature in this localized zone was  $\sim 1200^\circ\text{C}$  and material started depositing in the corners and they started spreading downwards from all four sides. With passing time the length of these structures increased as the lobes got more and more localized (Figures 5.9b and 5.9c). Figure 5.9d shows the Si attenuator after it was taken out from the chamber. It is seen that black, sharply pointed structures that came down from the edges are strong enough to take the weight of Si piece. It is also observed that deposition mainly took place at the four corners and the central portion had nothing but a black patch. When

examined under SEM (Figure 5.9e), it was seen that GNWs had formed in all these black sharp structures while the central portion was almost devoid of any particular type of nanostructures. It shows that whenever, there is carbon feedstock present in the plasma with reasonably high temperature, then without any surface modification and external bias on the Si substrate, GNWs will form unhindered.

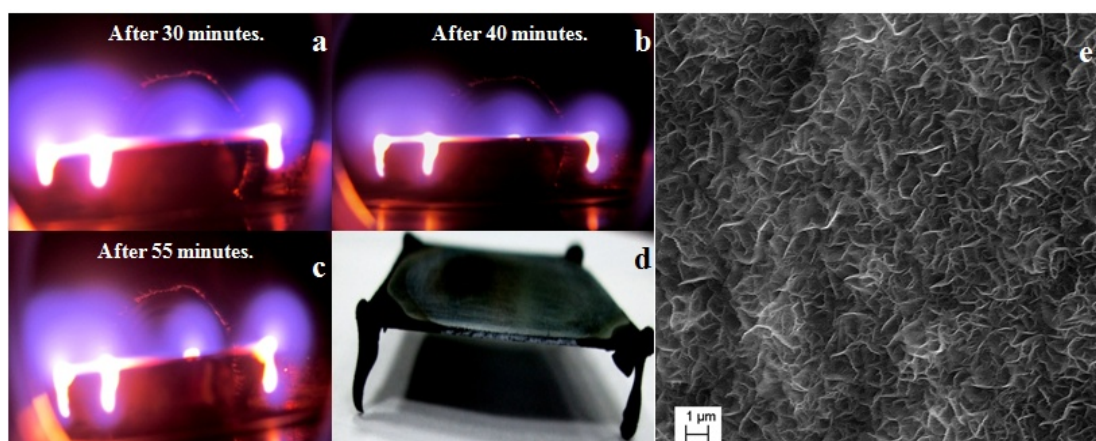


**Figure 5.9:** Actual photograph of the deposition (a) after 30 minutes, (b) after 40 minutes, (c) after 55 minutes; (d) actual photograph of the Si attenuator after it was taken out of the chamber, (e) SEM image of the deposited black mass on the Si attenuator showing presence of the GNWs.

Most important facts shown by these experiments is that unlike popular belief it is possible to find a window for co-deposition of  $sp^2$  and  $sp^3$  hybridized carbon structures in a single experiment on different substrates in a PECVD chamber with proper control on carbon containing precursor flow. It is also seen that substrate positioning and pre-treatment plays a big role in deciding what type of deposition occurs.

## 5.5. Conclusion

Investigations reported here show that co-deposition of sp<sup>2</sup> and sp<sup>3</sup> hybridized carbon nanostructures are possible by MPECVD. It is shown that choice and surface treatment of the substrate is important for a particular type of deposition and precursor flow rate is a major controlling factor for co-deposition experiments. When an unscratched Si surface is used as attenuator with comparative high flow rate of precursor gas (20 SCCM in this case), it is seen that GNWs can be grown on the attenuator along with CNTs on Inconel substrate. But if a scratched Si surface is used with relatively lower precursor flow rate (5 SCCM in this case), NCD can be obtained on attenuator along with CNTs on the substrate. From OES, it is also shown that intensity of diatomic carbon during the deposition can be taken as a marker of control for CNT deposition. Through a schematic model it is shown that, one needs to make sure that substrates are placed inside the plasma sheath for co-deposition and feeding rate of carbon containing precursor should be lowered to avoid formation of unwanted carbon based structures. This entire work has been published in Carbon [45].

## References:

1. J.E. Butler, Y.A. Mankelevich, A. Cheesman, J. Ma, M.N.R. Ashfold, J.Phys: Condens. Matter 21 (2009) 364201.
2. F.J.G. Silva, A.J.S. Fernandes, F.M. Costa, V. Teixeira, A.P.M. Baptista, E. Pereira, Wear 255 (2003) 846.
3. K. Jagannadham, Solid-state Electron., 42 (1998) 2199.
4. A.K. Mallik, N. Dandapat, S. Chakraborty, A.K. Mandal, J. Ghosh, M. Unnikrishnan et al. Proces. Appl. Ceramic., 8 (2014) 69.

5. R. Velázquez, V.F. Neto, K. Uppireddi, B.R. Weiner, G. Morell, *Coatings*, 3 (2013) 243.
6. S. Iijima, *Nature* 354 (1991) 56.
7. P. Jarillo-Herrero, J.A. Van Dam, L.P. Kouwenhoven, *Nature* 439 (2006) 953.
8. S. Fan, M.G. Chapline, N.R. Franklin, T.W. Tombler, A.M. Cassell, H. Dai Fan, *Science* 283 (1999) 512.
9. K.B.K. Teo, E. Minoux, L. Hudanski, F. Peauger, J.P. Schnell, L. Gangloff et al., *Nature* 437 (2005) 968.
10. T.T. Baby, R.B. Rakhi, N. Ravi, S. Ramaprabhu, *J. Nanosci. Nanotech.* 12 (2012) 6718.
11. R.Kar, S.G. Sarkar, C.B. Basak, A. Patsha, S. Dhara, C. Ghosh et al. *Carbon* 94 (2015) 256.
12. T. Machino, W. Takeuchi, H. Kano, M. Hiramatsu, M. Hori, *Appl. Phys. Express* 2 (2009) 025001.
13. O. Tanaike, N. Kitada, H. Yoshimura, H. Hatori, K. Kojima, M. Tachibana, *Solid State Ionics* 180 (2009) 381.
14. T. Itoh, S. Shimabukuro, S. Kawamura, S. Nonomura, *Thin Solid Films* 501 (2006) 314.
15. Y. Wu, B. Yang, B. Zong, H. Sun. Z. Shen, Y. Feng, *J. Mater. Chem.* 14 (2004), 469.
16. F.G. Celii, D. White Jr., A.J. Purdes, *Thin Solid Films* 212 (1992) 140.
17. F.G. Celii, D. White Jr., A.J. Purdes, *J. Appl. Phys.* 70 (1991) 5636.
18. W. Chen, X. Lu, Q. Yang, C. Xiao, R. Sammynaiken, J. Maley et al. *Thin Solid Films* 515 (2006) 1970.

19. M. Ali, M. Ürgen, Solid State Sciences 14 (2012) 150.
20. Q. Liang, C.Y. Chin, J. Lai, C. Yan, Y. Meng, H. Mao et al. Appl. Phys. Lett. 94 (2009) 024103.
21. P. Joeris, G. Bendorf, S. Bohr, J. Appl. Phys. 71 (1992) 4638.
22. M.L. Terranova, S. Orlanducci, A. Fiori, E. Tamburri, V. Sessa, Chem. Mater. 17 (2005) 3214.
23. A.J.S. Fernandes, M. Pinto, M.A. Neto, F.J. Oliveira, R.F. Silva , F.M. Costa, Diamond & Related Materials 18 (2009) 160.
24. N. Shankar, N.G. Glumac, M. Yu, S.P. Vanka, Diamond Relat. Mater. 17 (2008) 79.
25. D. Takagi, Y. Kobayashi, Y. Homma, J. Am. Chem. Soc. 131 (2009) 6922.
26. Y.Q. Hou, D.M. Zhuang, G. Zhang, M.S. Wu, J.J. Liu, Appl. Surf. Sci. 185 (2002) 303.
27. C.R. Kumaran, M. Chandran, M.K. Surendra, S.S. Bhattacharya, M.S.R. Rao, J Mater Sci 50 (2015) 144.
28. Q. Yang, Y. Tang, S.L. Yang, Y.S. Li, A. Hirose, Carbon 46 (2008) 589 .
29. R. Kar, N.N. Patel, S.S. Chopade, S. Mukherjee, A.K. Das, D.S. Patil, J. Exp. Nanosci. 9 (2014) 575.
30. M. Vojs, M. Varga, O. Babchenko, T. Ižák, M. Mikolášek, M. Marton et al. App. Sur. Sci. 312 (2014) 226.
31. T. Chein, J. Wei, Y. Tzeng, Diamond Relat. Mater. 8 (1999) 1686.
32. P.W. May, W.J. Ludlow, M. Hannaway, P.J. Heard, J.A. Smith , K.N. Rosser, Diamond Relat. Mater. 17 (2008) 105.

33. Y.F. Zhang , F. Zhang , Q.J. Gao, X.F. Peng , Z.D. Lin, *Diam. Relat. Mater.* 10 (2001) 1523.
34. T. Lin, G. Y. Yu, A. T. S. Wee, Z. X. Shen, *App. Phys. Let.* 77 (2000) 2692.
35. V. Kaushik, H. Sharma, A. K. Shukla, V. D. Vankar, *AIP Conf. Proc.* 1451, (2012) 148.
36. F.Ding, K. Bolton, A. Rosèn, *J. Elec. Mat.* 35 (2006) 207.
37. O.J.L. Fox, J. Ma, P.W. May, M.N.R. Ashfold, Yu.A. Mankelevich, *Diam. Relat. Mater.* 18 (2009) 750.
38. S. Kurita, A. Yoshimura, H. Kawamoto, T. Uchida, K. Kojima, M. Tachibana et al. *J. App. Phys.* 97 (2005) 104320.
39. Z.H. Ni, H.M. Fan, Y.P. Feng, Z.X. Shen, B.J. Yang, Y.H. Wu, *J. Chem. Phys.* 124 (2006) 204703.
40. M.S. Dresselhaus, G. Dresselhaus, R. Saito, A. Jorio, *Phys. Rep.* 409 (2005) 47.
41. L.M Malard, M.A. Pimenta, G. Dresselhaus, M.S. Dresselhaus, *Phys. Rep.* 473 (2009) 51.
42. M.S. Dresselhaus, A. Jorio, M. Hofmann, G. Dresselhaus, R. Saito, *Nano Lett.* 10 (2010) 751.
43. L.G. Cancado, M.A. Pimenta, R. Saito, A. Jorio, L.O. Ladeira, A. Gruneis et al. *Phys. Rev. B* 66 (2002) 035415.
44. S.A. Linnik, A.V. Gaydaychuk, *Vacuum* 103 (2014) 28.
45. R.Kar, N.N. Patel, N.Chand, Shilpa R. K., R. O. Dusane, D.S. Patil, S.Sinha, *Carbon*, 106 (2016) 233.

## **Chapter 6**

### **Conclusions & Future Scope**

#### **6.1 Conclusion**

During the course of this work, we have employed PECVD technique to deposit different carbon nanostructures, characterized these samples, studied their field emission characteristics and investigated their growth mechanism in the plasma environment. We have used two different PECVD systems where operating pressure ranged from 50 to  $10^{-4}$  Torr. Over this wide spectrum we have been able to deposit three different carbon nanostructures namely, GNWs/CNWs, MWCNT and NCD. We started our work with very low pressure ECR-CVD for better control on the deposition. We used catalytic-PECVD method in this scheme, where 30 nm thick Ni thin film was used as the catalyst on Si surface. Our endeavor resulted in the deposition of CNWs in this system without application of external bias. We carried out investigations on this deposited nanomaterial and found that silicide formation could be avoided even when the substrate had no diffusion resistant barrier. Drawing on earlier research we also proposed a qualitative model describing the growth of CNWs based on the LSPR effect of Ni nanoparticles in the plasma environment.

After successful generation of CNWs on Si we aimed to achieve similar control on carbon nanomaterial growth also for a faster growth rate and thus chose MPECVD as the preferred method of deposition for our remaining activities. MPECVD is a technique where operating pressure remains  $\sim 50$  Torr resulting in faster deposition. Apart from changing the system for deposition we also investigated the possibility of deposition of other carbon nanostructures. thought We focused on the CNT this time which has been one of the most extensively studied among the



carbon nanostructures. We also focused our interest on the particular application of field emission from these CNTs for our research. Field emission application has long been under investigation and our investigations resulted in new data, particularly from the point of view of substrate preparation and microwave attenuation. Our aim was to show how simple changes made on the substrate could result in CNTs with enhanced field emission current density. Our experiments showed that with the proper substrate pre-conditioning (heat-treatment) and by using microwave attenuator on the top of the growing surface, it is possible to deposit CNTs having high FEF ( $\sim 6740$ ) at a low turn on electric field of ( $\sim 0.65$  V). Our results have shown that the presence of clearer grain boundaries due to heat-treatment of substrate helps in formation of transition metal nanoparticles more efficiently. Further, it was concluded that incorporation of the microwave attenuator on the growing surface promotes growth of CNTs at a faster rate with higher aspect ratio and favorable bamboo-like defects.

Having generated CNWs/ GNWs and CNTs separately by two different PECVD techniques, we ultimately tried to use a single PECVD technique to grow different carbon nanostructures. In fact, we went one step further and tried to explore the possibility of co-deposition of two different nanostructures in a single experiment. We again chose MPECVD as the preferred technique for its faster deposition rate. During our research we showed that it is possible to deposit GNW and CNT together in a single experiment. Moreover, we could also show that sp<sup>2</sup> and sp<sup>3</sup> hybridized carbon nanostructures (CNT and NCD in this case) can also be deposited in a single experiment by MPECVD method. During the experiments, we used Inconel as the substrate for CNT deposition and Si microwave attenuator for the deposition of GNW and NCD. During analysis of results, it was seen that choice and surface treatment of

the substrate are very important for a particular type of deposition and precursor flow rate is a major controlling factor for these experiments. When an unscratched Si surface was used as attenuator with comparative high flow rate of precursor gas GNWs could be grown on the attenuator along with CNTs on Inconel. But when a scratched Si surface was used with lower precursor flow rate NCD could be obtained along with CNTs. With the help of OES, we found that intensity of diatomic carbon can serve as a marker for controlled co-deposition experiments. Our observations were described with the help of a schematic model for the process of co-deposition.

## **6.2 Future Scope**

The present work described this thesis needs to be taken forward both in terms of experiments and theoretical simulation in future. A few key areas which can be explored in future include: (i) Effect of microwave attenuation on CNTs and other nanostructures can be studied further by replacing Si with other possible attenuators, such as  $\text{Al}_2\text{O}_3$ . This could be an important investigation to further increase our knowledge on the use of microwave attenuator for production of CNTs by MPECVD method, (ii) For field emission studies in the future, we need to study the emission stability of the emitters along with the emission uniformity and density. This is important as high value of emission current density is not the only criteria for a good field emitter, (iii) In addition to field emission such films of CNT, GNW could be tested for their performance for other applications, such as supercapacitors, (iv) Simulation of the process involving co-deposition mechanism would provide an understanding of mechanism occurring within the and try to see what actually happens inside the plasma sheath during the deposition and all microscopic parameters which affects its growth, (v)

Detailed simulation of the growth mechanism well validated against experimental data would enable controlled growth of nanostructure of choice.